

# **AN INVESTIGATION INTO ABDOMINAL AORTIC ANEURYSM (AAA) RUPTURE PREDICTION**

**ABD HALIM EMBONG**

**PhD**

**2014**



**Auckland, New Zealand**

# **AN INVESTIGATION INTO ABDOMINAL AORTIC ANEURYSM (AAA) RUPTURE PREDICTION**

**ABD HALIM EMBONG**

A Thesis Submitted to  
Auckland University of Technology in  
Fulfilment of Requirements for the Degree of  
**Doctor of Philosophy (PhD)**

**2014**

Faculty of Design & Creative Technologies  
School of Engineering  
Institute of Biomedical Technologies (IBTec)  
Auckland University of Technology  
Auckland, New Zealand

Primary Supervisor: Professor Ahmed Al-Jumaily

## DECLARATION

'I hereby declare that this submission is my own work and that, to the best of my knowledge and belief, it contains no material previously published or written by another person nor material which to a substantial extent has been accepted for the qualification of any other degree or diploma of a university or other institution of higher learning, except where due acknowledgment is made in the acknowledgements.'

Signature: 

Name: Abd Halim Embong

Date: 16 March 2015

I further authorise the Auckland University of Technology to reproduce this thesis by photocopying or by other means, in total or in part, at request of other institutions or individuals for the sole purpose of scholarly research.

Signature: 

Name: Abd Halim Embong

Date: 16 March 2015

## BORROWER PAGE

The Auckland University of Technology requires the signatures of all people using or photocopying this thesis. Accordingly, all borrowers are required to fill out this page.

Date                      Name                      Address                      Signature

## ACKNOWLEDGEMENT

The completion of this research has been a challenging but very pleasurable journey. I honour God's unceasing faithfulness and mercy, without which, I would not have been able to meet this challenge. As with all such endeavours, without the strength granted by God and the support of numerous people and institutions, this research would not have been possible.

First and foremost, I would like to express my appreciation to my supervisor, Professor Ahmed Al- Jumaily, Director of the Institute of Biomedical Technologies (IBTec). He is a very humble and dedicated person who offered a tremendous amount of support along this journey. Also, his willingness to help, and advice at all levels, both theoretical and analytical, are highly valued. His knowledge and insights have been hugely beneficial and helpful. I pray to God to grant him a continued long, healthy and successful life. I would like to express my thanks and gratitude to my secondary and tertiary supervisors, Dr Giri Mahadevan (Counties Manukau District Health Board (CMDHB) Vascular Surgeon) and Dr Andrew Lowe, respectively, for their continuous guidance, invaluable help, discussion and support, which ensured the completion of this research.

I also would like to acknowledge the Manukau Super Clinic vascular nurse specialist, Marion Gibson and members of the Vascular Nurse Team, Carol Duncan, Janet Franks and Bev McKenzie, for their great guidance and cooperation during data collection.

Many thanks also to the International Islamic University Malaysia (IIUM) and Ministry of Education Malaysia (MoE) for supporting this research and giving me the opportunity to pursue my PhD at Auckland University of Technology (AUT) in New Zealand. Their financial support through a scholarship has been a great help.

I gratefully acknowledge many colleagues and staff at AUT, particularly those in IBTec and the Postgraduate Office that have offered me remarkable assistance and support to ensure that my PhD process ran smoothly. I would like to especially thank my lovely colleagues, Lulu, Thomas, Pierson, Arun, Sherif and the pretty Jo who always ready to help. Thank you all.

To the most special people in my life, my wife Nurul Husna Shaberi and my two little ‘Kiwi’ heroes, Muhammad Amir Harith and Muhammad Amir Hafiy. To my wife: I was blessed by having you as my special companion who motivated and supported me through the countless phases of doing my PhD. To my two little heroes: thank you for your patience. Your laughter and smiles have given me strength to complete this journey. Also my sincere appreciation to all of my family in the ‘Waris Haji Embong Group’ in Terengganu and the Tok Kerawat family in Kelantan, Malaysia including all friends who always stood behind with their pray and moral support. Without their support and encouragement, this thesis would not have been possible. It is an absolute obligation for me to thank them because they always provided me with the confidence and belief in my aptitude to complete this thesis successfully.

Finally, I would also like to acknowledge ethical approval from the Auckland University Ethics Committee (AUTEK) and CMDHB for the human ethics approval number AUTEK 12/273 on 11 December 2012 and CMDHB 1404 on 23 November 2012.

## ABSTRACT

Cardiovascular Disease (CVD) is one of the leading causes of death and disability in the world. The mortality rate between 1993 -1997 in New Zealand was about 46% and 32% worldwide. CVDs such as Abdominal Aortic Aneurysm (AAA) is life threatening and poses a very high risk for aneurysm patients with particular aneurysm diameter.

AAA rupture is a patient-specific problem with evolving structures and on-going growth. Current ultrasound methods are used to probe for and diagnose instantaneous AAA by analysing arterial tissue deformation. However, tracking the progression of potential aneurysms, and predicting their risk of rupturing based on the diameter of the aneurysm is still an insufficient method. AAA image segmentation and analysis using the Patient-Specific Aneurysm Rupture Predictor (P-SARP) protocol is proposed to identify dependent elements that lead to a three-dimensional (3-D) aneurysm reconstructive model. Models of the patient-specific aneurysm images were designed along with biomechanical characterization and specific material properties to be incorporated. Fluid Structure Interaction (FSI) is used to mathematically establish the oscillations of patient-specific cyclic pressure loading in order to visualize the impact of potential pressure distributions on the deformed arterial wall over time. The correlation between the geometric elements and the models' potential for rupture are extensively investigated to produce a possible AAA rupture mechanism.

This research presents a new Computational Fluid Dynamics (CFD) of Patient-Specific Aneurysm Model (PSAM) which is based on the energy strain function combined with the dilated vessel wall stress-strain relationship to predict aneurysm rupture. This thesis focuses on investigating how computer simulation can be incorporated to predict AAA rupture. The personalized model is developed based on instantaneous arterial deformations obtained from ultrasound images using a 6-9 MHz doppler transducer. The PSAM relies on available

mechanical properties and parameters obtained from the personalised model. Using the strain energy function based on historical stress-strain relationship to extrapolate cyclic loading on the PSAM along with patient-specific pressure, multi variant factors are proposed and considered to predict the actual location of the weakening points to reach rupture. The material properties of the wall are calculated using biaxial tensile tests to observe the time dependency of the material response and formation of the aneurysm wall rupture.

The outcomes indicate that the proposed technique of the PSAM model has the ability correlate the wall deformation and tissue failure mode with predicting rupture. Thus, this method can positively be integrated with already established ultrasound techniques for improvements in the accuracy of future diagnoses of potential AAA ruptures.

# TABLE OF CONTENTS

DECLARATION.....	iii
BORROWER PAGE.....	iv
ACKNOWLEDGEMENT.....	v
ABSTRACT.....	vii
TABLE OF CONTENTS.....	ix
LIST OF FIGURES.....	xiii
LIST OF TABLES.....	xv
LIST OF UNIT, SYMBOLS AND ABBREVIATIONS.....	xvi
CHAPTER 1: BACKGROUND.....	1
1.1: Introduction.....	1
1.2: Human Circulatory System Structure.....	1
1.3: Arterial Tissue Structure.....	3
1.4: Aneurysm Disease in the Human Abdominal Aorta (AA).....	4
1.5: Disease diagnosis and treatment.....	5
1.6: Biomechanics of AA.....	7
1.7: Numerical Modelling using Computational Method.....	8
1.8: Closure.....	8
CHAPTER 2: LITERATURE REVIEW.....	9
2.1: Introduction.....	9
2.2: General AAA Risk.....	10
2.2.1: Aneurysm Factors Parameters.....	10
2.3: Clinical and Mechanical Characteristics.....	11
2.4: AAA Regenerated Model using US.....	12
2.5: Rupture Risk Detection and Prediction.....	13
2.6: Stress-Strain Relationship in Tissues Behaviour.....	17
2.7: Mathematical Model for Elongation.....	21
2.8: Artery Biomechanics: Rupture Theory.....	22
2.9: Computational Simulation and Modelling in Rupture Prediction.....	23
2.10: Computational Simulation and Modelling Fluid-Structure Interaction (FSI).....	24
2.11: Summary.....	25
2.12: Objectives.....	26
2.13: Closure.....	27
2.14: Research and Thesis Outline.....	28
CHAPTER 3: MODEL FORMULATION.....	31
3.1 Introduction.....	31
3.2 Tissue Failure Overview.....	31
3.2.1: Strain Deformation.....	34
3.2.2: Equivalent Stress.....	34
3.2.3: Strain Energy.....	36

3.2.4 Stress Cycles .....	37
3.2.5 Total Life Curve .....	37
3.3 Computer Modelling.....	38
3.3.1 Fluid Flow Equation .....	38
3.3.2 Wall Equation .....	41
3.3.3 Fluid Structure Interaction (FSI).....	42
3.3.4 Two-Way FSI .....	42
3.4 Material Assumption and Solution Method .....	43
3.4.1 Wall Assumptions.....	43
3.4.2 Blood Flow Assumptions.....	44
3.4.3 FSI Coupling Solver .....	45
3.5: Tissue Failure Characteristic in Modelling.....	45
3.6: Closure.....	48
CHAPTER 4: AAA PATIENT DATA COLLECTION .....	50
4.1: Introduction .....	50
4.2: AAA Patient Data Collection .....	51
4.2.1: Patient Database .....	52
4.2.2: Ethics Approval .....	53
4.2.3: Consent .....	53
4.2.4: Data Storage .....	53
4.3: P-SARP Protocol using US .....	53
4.3.1 P-SARP Protocol Procedure .....	54
4.4: Ultrasound Accuracy and Visual Limitation .....	58
4.5: Closure.....	60
CHAPTER 5: ANEURYSM SIMULATION AND ANALYSIS.....	61
5.1: Introduction .....	61
5.2 US Structural Design and Geometrical Analysis.....	61
5.2.1 Factors by Segment and Thickness.....	63
5.3 Modelling and Simulation .....	65
5.3.1 Patient Specific Aneurysm Model (PSAM).....	65
5.3.2: Geometry Design.....	66
5.3.3: Mesh Generation.....	69
5.3.4: Boundary Conditions .....	71
5.3.5: Material Properties of the Model.....	73
5.3.6: Parameters Specification .....	74
5.4 Simulation Results .....	75
5.4.1 High deformation region.....	76
5.4.2 Maximum Stress Region.....	80
5.4.3 Ultimate Strain Energy Region.....	83
5.5 Closure.....	85
CHAPTER 6: ANEURYSM WALL DEFORMATION AND RUPTURE PREDICTION .....	86
6.1 Introduction .....	86

6.2 Geometric Aspects of Failure .....	86
6.3 Physical Aspect of Failure .....	90
6.4 Biaxial State of Loading .....	92
6.4.1 Experimental Setup.....	93
6.4.2 Raw Data Analysis .....	94
6.4.3 Prediction Factors from True Stress Strain Curve .....	98
6.5 Tissue Fatigue Cyclic testing.....	101
6.5.1 Experimental Setup.....	101
6.5.2 Data Analysis.....	102
6.5.3 Prediction Factor – Calculated Stress-Cycle Curve (S-N curve).....	103
6.6: Blood Vessel Fatigue to Failure .....	106
6.7: Other Related Prediction Factors.....	106
6.7.1: Cyclic Loading .....	107
6.8: Closure.....	108
CHAPTER 7: ANALYSIS AND DISCUSSION .....	109
7.1 Introduction .....	109
7.2: Model Geometrical Analysis .....	109
7.2.1: High Risk Location and Affected Factors .....	111
7.3: Physical Parameter Analysis.....	115
7.3.1: Strain Energy .....	115
7.3.2: Maximum Stress .....	116
7.4: Comparison Study and Empirical Evidence .....	117
7.5: Ultimate Failure Tissue Analysis.....	120
7.5.1 Failure Tissue Formula .....	121
7.6: Fatigue Tissue Analysis.....	121
7.6.1: Fatigue Formula.....	122
7.6.2: Stress Life Cycle (S-N curve) Analysis.....	122
7.7: Aneurysm Progress Validation .....	125
7.7.1: Annual Validation Methods.....	126
7.8: Summary.....	131
7.9: Conclusion.....	132
7.10: Future Work.....	133
7.10.1: Integrated Aneurysm Assessment Method for Screening, Processing and Prediction Improvement .....	133
7.10.2: Instantaneous AAA modelling reconstruction.....	135
REFERENCES .....	136
APPENDIX A: HUMAN ETHICS APPROVAL.....	143
APPENDIX B: SPECIMEN TRUE STRESS AND TRUE STRAIN .....	145
A.1 Maximum True Stress in specimen by Sugita [124].....	145
A.2 Strain of the specimen.....	146
APPENDIX C: ANEURYSM PSAM RESULTS .....	147
B.1 Patient-Specific Von Mises Stress .....	147

B.2 Patient-Specific Strain Energy .....	148
B.3 Patient-Specific Deformation.....	150
APPENDIX D: ANEURYSM GEOMETRY BASED ON 3 YEARS PROGRESS .....	152
APPENDIX E: GOODMAN STRESS RANGE RECONSTRUCTION.....	154

## LIST OF FIGURES

Figure 1. 1: Human Circulatory System with Oxygenated Blood (Red) and Deoxygenated Blood (Blue) [2] .....	2
Figure 1. 2: Arterial Tissue Structure Composition [5] .....	4
Figure 1. 3: Normal Aneurysm Location in Humans [10] .....	5
Figure 1. 4: The deformation of the artery and stent for (A) The Nir Design by Boston Scientific and (B) The S7 Design by Medtronic Ave (One quarter of the Artery and Stenosis is Removed for viewing)[12].....	7
Figure 2. 1: (A) Collagen-Elastin Composition Curve in Arterial Wall) adapted from Fung [29]; and (B) The Three Stages of AAA Degeneration Composition related to Rupture from Kleinstreuer et al. [1] .....	11
Figure 2. 2: Histology of Normal Aorta (Left) and Aneurismal Aorta (Right). Adapted from [32].....	12
Figure 2.3: Stress-Strain Curve from Stress-Strain Relationship in Engineering .....	18
Figure 2. 4: Uniaxial Testing on Excised Human AAA after Surgery For Validation [81].....	21
Figure 2. 5: Research Layout.....	30
Figure 3. 1: A) Strain Energy is the area under Stress-Strain Curve And; B) Energy Loss is the area under the Stress-Strain Loop [68].....	33
Figure 3. 2: Cartesian Co-Ordinates for the 3 Dimensional Stress shape deformation in FEM .....	36
Figure 3. 4: Modelling Result from Aneurysm Model with three observed parameters; Strain Energy (1), Strain Deformation (2) and Stresses (3).....	47
Figure 4. 1: Measuring with US Doppler with the proper Insonification Angle [148].....	55
Figure 4. 2: Aneurysm Assessment Using P-SARP .....	55
Figure 4. 3: Cross-Sectional Aorta From US for measurement .....	56
Figure 4. 4: Abdominal Ultrasound Images Segmentation (AUis) Template.....	57
Figure 4. 5: (A) Measurement of the diameter in the US Image (B) Measurement of the thickness with 45 Degrees C) Image regeneration .....	58
Figure 4. 6: Thickness Measurement from Ultrasound Imaging .....	59
Figure 4. 7: Expansion Measurement between Systolic and Diastolic Pressure.....	60
Figure 5. 1: A) Measurement Points from Aneurysm Location in Patient, B) Model Location of the Segment A1-A5 based on Cross Sectional Points in accordance to P-SARP Protocol. Image originally adapted from Aortic Dissection [151] .....	62
Figure 5. 2: Aneurysm Deformation at each segment in (A) Vertical and (B) Horizontal .....	64
Figure 5. 3: Computational Method Stages .....	65
Figure 5. 4: Geometry snapshot capture to CFD Modelling using ANSYS; A) Ultrasound Blood Vessel Morphology, B) Wall Thickness creation and C) AAA Blood Vessel regeneration .....	66
Figure 5. 5: Image Segmentation and Parametrical Modelling for the Idealised Model before PSAM from Real Aneurysm images .....	67
Figure 5. 6: Simplified Model with Boundary Conditions for each segment .....	68
Figure 5. 7: Aneurysm Geometry reconstruction based On P-SARP Protocol.....	69
Figure 5. 8: Mesh Generation for (A) Simplified PSAM and (B) Boundary Condition Setup.....	70

Figure 5.9: (A) Model Designated Axes (B) Boundary Condition with: (A) Both ends of the Artery are kept in a fixed position. (B) The Inner Surface of the fluid is set as FSI and (C) Imported fluid pressure to the wall. ....	72
Figure 5. 10: Input and Output Modelling Setup .....	72
Figure 5. 11: Imported Pressure from PSAM .....	73
Figure 5. 12: Setup Parameters in Computational Modelling.....	75
Figure 5. 13: Multi Variation Output Parameters Resulting from PSAM Simulation.....	76
Figure 5. 14: PSAM Model Deformation Region and Thickness Cross Section.....	77
Figure 5. 15: Aneurysm Deformation at affected region at Point A in Suspected Segment.....	78
Figure 5. 16: Aneurysm Deformation at Different Point and Segments.....	79
Figure 5. 17: Maximum Stress Region Location (A) and High Strain Energy (B) at Segment (Sg) 4 and 5 .....	81
Figure 5. 18: Maximum Stress for PSAM .....	82
Figure 5. 19: High Strain Energy at Segments (Sg) 4 and 5.....	83
Figure 5. 20: Various Strain Energy point on Aneurysm PSAM.....	834
Figure 6. 1: Tissue Failure Prediction Analysis.....	91
Figure 6.2: Experimental Setup: Schematic Illustration for Pressure Imposed Test Device Setup Image with permission from Sugita [123]. .....	94
Figure 6. 3: Pressurized Specimen during Inflation Testing (A) Flat Surface at no load state (B) Pressure loading supplied until Maximum Diameter (C) Pressure loading supplied after combined geometry [123] .....	96
Figure 6. 4: All Specimens True Stress and True Strain Curve .....	98
Figure 6. 5: A) Cyclic Test Setup and B) Profile Table.....	102
Figure 6. 6: S-N Curve based cyclic loading of specimen [122], (A) Number of cycles and (B) Log (N) cycle.....	104
Figure 6. 7: Sugita UTS And Gilpin's Cyclic Loading Stresses Vs. Endurance Limit.....	105
Figure 6. 8: Curve of Total Energy to Rupture .....	106
Figure 6. 9: Reconstructed Pressure Wave for Cycle Loading Modelling.....	108
Figure 6. 10: Pulsatile Time Flow for Pressure Waveform measured in Aorta within 20 Sec [158].....	108
Figure 7. 1: Parameters comparison location for A) Max Diameter, B) Maximum Stress and C) Maximum Strain Energy .....	110
Figure 7. 2: Excised Specimen taken from Patient Aneurysm Rupture at Multiple Region. A High-Speed Digital Image taken from Sugita [123] with permission.....	111
Figure 7. 3: Aneurysm Formation Atlas .....	113
Figure 7. 4: Stress Parameter Correlation Graph.....	119
Figure 7. 5: Strain Energy Parameter Correlation Graph.....	120
Figure 7. 6: Goodman Relation for PSAM-Failure Group Specimen.....	124
Figure 7. 7: Number Of Cycle for PSAM-Failure Group Specimen .....	124
Figure 7. 8: Goodman Relation based on Aneurysm Progressing Years .....	127
Figure 7. 9: Number Of Cycle Based On Aneurysm Progressing Years .....	128
Figure 7. 10: Goodman Stress Range .....	130

## LIST OF TABLES

Table 2. 1: Severity Parameter Factors Table from Kleinstreuer and Zhonghua [23] .....	19
Table 2. 2: Summary of Stress-Strain definitions used to determine the Elastic Modulus Aneurysm for the Thoracic Aorta [69] .....	19
Table 3. 1: The Material Parameter and Boundary Condition of Aneurysm Vessel Wall and Blood [136, 138, 139].....	44
Table 4. 1: Demographic of the Observed AAA Patient .....	52
Table 5. 1: Measuring Mesh Elements (Mesh Metrics).....	71
Table 5. 2: Stress, Strain Energy and Deformation Simulation Results .....	75
Table 5. 3: PSAM High Deformation .....	79
Table 6. 1: Thickness Per Segment Level Measurement (cm).....	88
Table 6. 2: Regression Summary based on Thickness Variation in each Segments .....	89
Table 6. 3: Summary of Origin, Sex Age, Position and Dimensions of Aneurysm Specimens.....	92
Table 6. 4: Patient Specific Diameter Range Classification .....	100
Table 6. 5: Specimens Strain Energy Per Unit Time .....	100
Table 7. 1: High Risk Location Related Factors .....	112
Table 7. 2: Segmented Diameter Deformation basedon A) Vertical Axis; and B) Horizontal Axis.....	114
Table 7. 3: Patient Specific Diameter Range Classification .....	116
Table 7. 4: Mean Stress and Alternating Stress Results based on Aneurysm Model.....	117
Table 7. 5: Modelling-Experimental Parameter Analysis Diameter Classification .....	118
Table 7. 6: Annual Aneurysm Progress Databa Modelling .....	11826
Table 7. 7: Endurance Stress from Annual Aneurysm Progress .....	11829

## LIST OF UNIT, SYMBOLS AND ABBREVIATIONS

<b>Symbols</b>	<b>Description</b>
E	Young Modulus
$E_{ZZ}$	Axial Strain
$E_{\theta\theta}$	Circumferential Strain
$E_{zz}$	Axial Strain
G	Initial Shear Modulus
K	Initial Bulk Modulus
P	Pressure
S-N Curve	Stress- Cycle Curve
t	Thickness
T	Time
$U_T$	Strain Energy per Unit Time
$U_f$	Energy required to failure
X, Y, Z	Coordinates
W	Strain Energy Function
$\sigma_e$	Endurance Stress Limit
$\sigma_{VM}$	Von Mises Stress
$\rho_w$	Wall Density
$\rho_f$	Fluid Density
$\nu$	Poisson's Ratio
$\mu F$	Dynamics Viscosity
$\epsilon_e$	Engineering Strain
$\sigma_e$	Engineering Stress
$\epsilon_t$	True Strain
$\sigma_t$	True Stress
$\tau_{ij}$	Total Cauchy Stress
$S_{ij}$	Second Piola Kirchhoff Tensor Stress
$\bar{I}$	Solid Unit Tensor

### Abbreviations

AA	Abdominal Aorta
AAA	Abdominal Aorta Aneurysm
ALE	Arbitrary Lagrangian-Eulerian
ADAM	Aneurysm Detection and Management

AUis	Aneurysm Ultrasound Image Segmentation template
AUTEC	Auckland University of Technology Ethics Committee
CFD	Computational Fluid Dynamics
CMDHB	Counties Manukau District Health Board
CT Scan	Computed Tomography Scan
CSA	Cross Sectional Area
FEM	Finite Element Method
FSI	Fluid-structure interaction
IBTec	Institute of Biomedical and Technologies
ILT	Intraluminal Thrombus
P-SARP	Patient-Specific Abdominal Rupture Predictor
PWV	Pulse Wave Velocity
MRI	Magnetic Resonance Imaging
UKSAT	United Kingdom Small Aneurysm Trial
US	Ultrasound
SP	Severity Parameter
3-D	Three-Dimensional
2-D	Two-Dimensional

#### **Units**

mmHg	Millimetre of mercury, unit for pressure
J	Joule
kPa	Kilo Pascal
Pa	Pascal
s	Second
ml	Millilitre

# CHAPTER 1: BACKGROUND

## 1.1: Introduction

The aim of this thesis is to investigate the correlation between Abdominal Aorta Aneurysm (AAA) blood vessel biomechanics and how computational modelling can play a role in predicting ruptures in aneurysms. This chapter discusses background information of AAA which is known as one of the most fatal of cardiovascular diseases. It starts with the general human circulatory system (Section 1.2) where the function of the aorta is studied. Subsequently, an introduction of physiological arterial tissue is given in (Section 1.3). Then, an overview of the disease in the human abdominal aorta is given in Section 1.4, followed with its diagnosis and treatment through visual assessments in Section 1.5. Section 1.6 explains blood vessel biomechanics and important components followed with computational modelling requirements in Section 1.7.

## 1.2: Human Circulatory System Structure

The circulatory system consists of three major elements which are the heart, blood and blood vessels. The function of the heart is to pump the blood to ensure that the cardio-transport system runs continuously. The blood flows through the heart through the blood vessels such as arteries, capillaries and veins as illustrated in Figure 1.1. The human aorta is an integral part of the circulatory system, used to transport the blood throughout the body, carrying the nutrients, oxygen and hormones to the cells. An average of five liters of blood flows through a varied and complex network of blood vessels which are distributed to all the organs and parts of human body providing nutrients and oxygen. The blood is distributed in a pulsatile flow and propagates a cycle loading as it travels along the arterial system. These important characteristics can be largely utilized to understand the difference in physiology between the

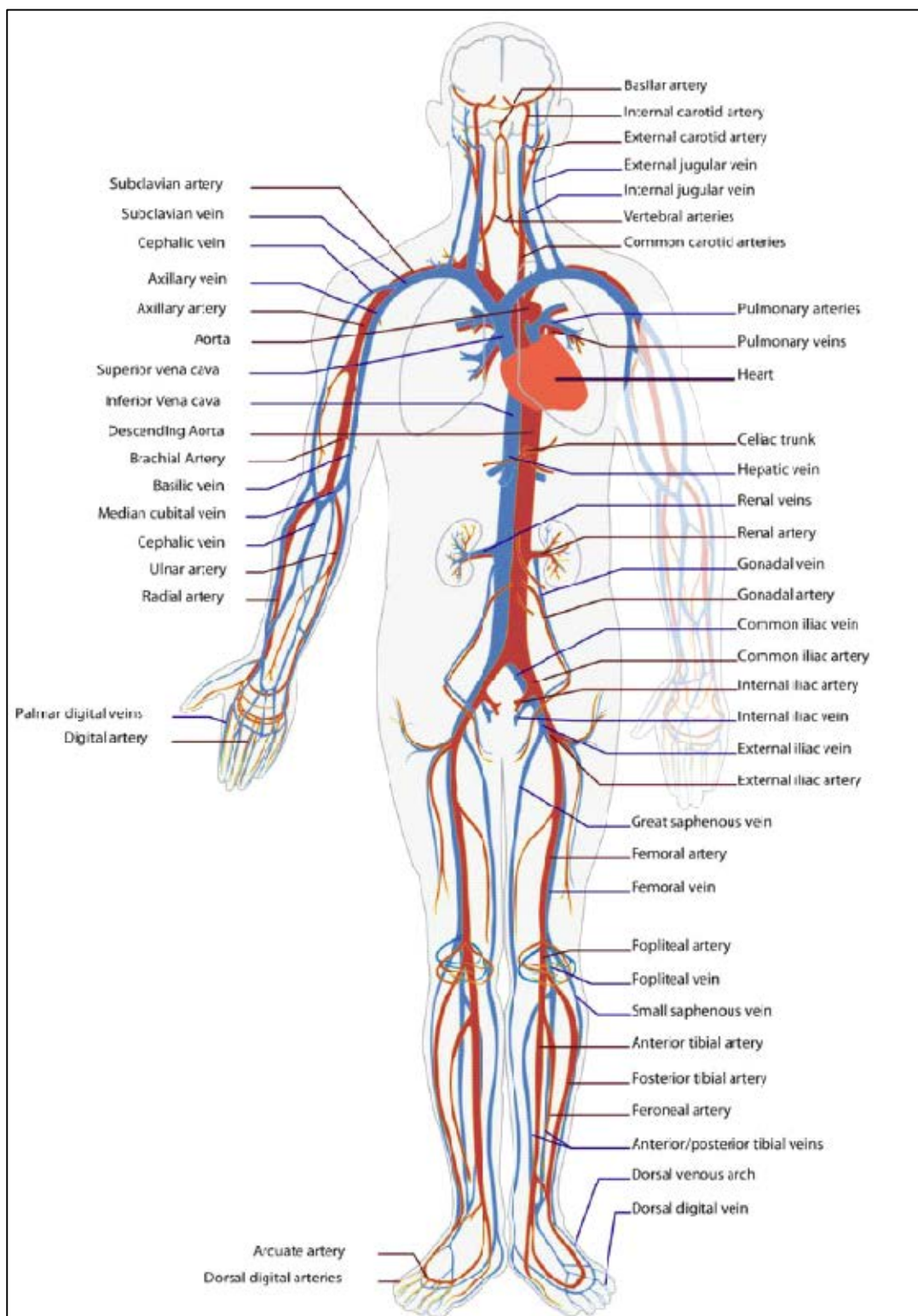


Figure 1. 1: Human circulatory system with oxygenated blood (red) and deoxygenated blood (blue) [2]

healthy and unhealthy circulatory system. The circulatory system is greatly vital but still malfunctions in many different ways due to disease [3]. The most important to understand is the mechanisms that are biomechanically and biologically affected because of the disease [3, 4]. Thus, investigating these mechanisms is an important element of this study.

### 1.3: Arterial Tissue Structure

The construction of the arterial tissue structure in Figure 1.2 contains three main layers known as the intima (inner), media (middle) and the adventitia (outer). The intima layer is constructed from a monolayer of endothelial cells on a base membrane to serve several purposes. It has a squamous structure with continuous cover which is responsible for the anti-thrombogenic behavior of the vessel wall. Also, it controls the transport of water, solutes, macromolecules and cells across the wall. The media is the thickest part, composed of smooth muscle cells and connective tissues known as collagen and elastin [5-7]. They consist of cells and matrix fiber which are circumferentially oriented during blood pulsatile flow. The media constitutes of the smooth muscle cells that allow for the control of the arterial diameter [5-7]. The adventitia forms the outer layer of the blood vessel which mainly constituted of connective tissue and axially-oriented collagen fibres [5-7]. It also protects and mechanically supports the intima and media from external disruption.

Different arteries have different ratios of arterial wall structural components [8]. For example, hypertension may lead to hypertrophy of the medial layer, elastin degradation and also collagen formation based on the different cases. Arterial stiffening increases transiently as blood pressure rise [5]

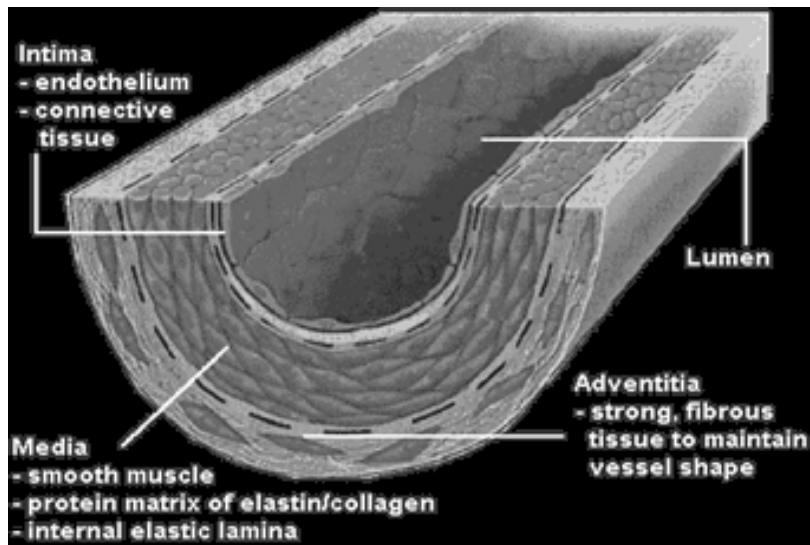


Figure 1. 2: Arterial Tissue Structure Composition [5]

#### 1.4: Aneurysm Disease in the Human Abdominal Aorta (AA)

Cardiovascular diseases such as AAA are a major cause of death and disability. The worldwide mortality rate is between 32-95% and in New Zealand, the rate is 46% [6, 7]. AAA occurs when there is an enlargement of the abdominal aorta (see Figure 1.3) and it usually affects the aorta from the renal arteries to the bifurcation region. The abdominal aorta becomes dilated due to the weakened vessel wall and eventually inflates like a balloon. It usually does not cause any symptoms to patients until they rupture, and the sudden onset of severe back and abdominal pain is a characteristic of a ruptured abdominal aortic aneurysm. The risk of rupture is directly related to aneurysm size and continues to be associated with high morbidity and mortality [8]. It can be considered as a fatal surgical emergency without surgical repair. Rupture of aneurysm can occur at any size, however it is more common once the vessel dilates to over 2.5 times the original vessel diameter or if the annual diameter increase is greater than the expected per year. Rupture is unpredictable and can occur during a radiology examination especially for the patient with a leakage in the aneurysm which is hemodynamically in an unstable condition [9]. Current practice is to electively repair an AAA surgically once the aneurysm diameter size reaches 5.5 cm. The repair can be performed either as an open surgery or endoluminal repair,

however, both these procedures are invasive and expensive treatments with their own associated morbidity and mortality.

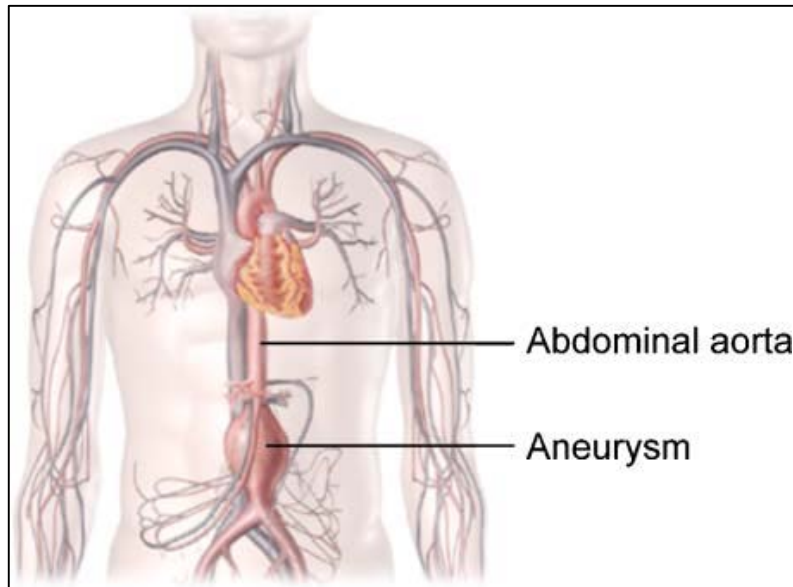


Figure 1.3: Normal Aneurysm Location in Humans [10]

#### 1.5: Disease diagnosis and treatment

AAA normally diagnosed or screened through medical modalities which have the ability to noninvasively detect the presence of aneurysm. Conventionally, the most used non-invasive devices are Ultrasound (US), Magnetic Resonance Imaging (MRI) and Computed Tomography (CT) scan. These tools used to help vascular nurses to screen the internal part of the body including bones, tissue and blood through imaging techniques for mechanical characterization. An operation is usually advised when the threat of the aneurysm bursting (which is usually fatal) is more than the risk of an operation. For diameters up to 50 mm, the growth rate is between 1-4 mm per year and increases when the size is more than 50 mm.

In general, the diseases are detected using physical examination done by vascular nurses and surgeons for potential patients before undergoing further assessment. These medical

assessments and examinations are usually conducted with X-Ray machines, US, CT scan and MRI. Most of them are costly devices for examination and not advisable as a close monitoring technique except for US. The latter is considered as a relatively cheaper method and is used in most pre-screening stages.

US devices are the most common imaging modalities which have the possibility of accurately discerning the morphology of the vessel wall and flexibility. Hence, this technique is used clinically to detect the presence of aneurysms. In order to get an accurate measurement, an US probe has to be positioned at a certain insonification angle (non-perpendicular) with respect to the blood velocity vector. Inconsistency in insonification angle might result in velocity errors of the same order [11]. US examination of the abdomen is a very good way of finding an aneurysm as well. It is a painless procedure involving a lubricated probe pressing gently on the abdominal skin over the aneurysm. The scan will identify the existence of an aneurysm on top of the exact site. (Further detail of the method will be described in Chapter 4). Some patients have the aneurysm diagnosed incidentally when they are examined for alternative problems or reasons e.g: prostate, kidney trouble or gallstones.

Most aneurysms are treated by surgical operation in which the aneurysm is replaced with an artificial artery made of robust polyester, which is unlikely to be replaced (as shown in Figure 1.4). To treat this operatively, the abdominal aorta is clamped at both ends of the aneurysm sac to temporarily stop the blood flow. The artificial blood vessel graft is sewn in position, and the aneurysm is sutured and sealed around the affected area. After the aorta is intact, blood will flow through the graft instead of the aneurysm. Circulation is restored and the incision is closed. The operative result is checked using an angiogram to ensure complete repair. This operation is very expensive as well as very risky.

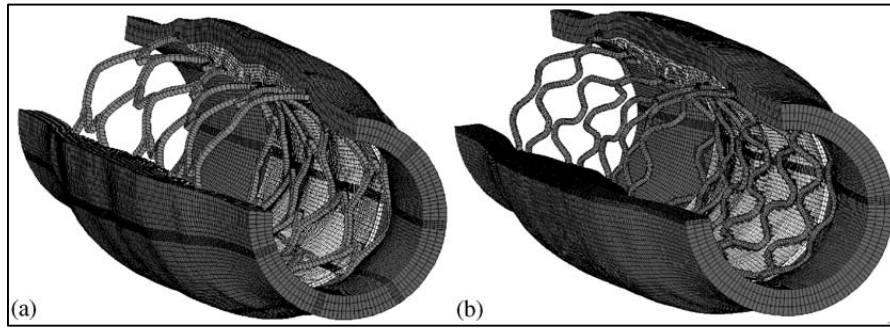


Figure 1. 4: The deformation of the artery and stent for (a) the NIR design by Boston Scientific and (b) the S7 design by Medtronic AVE (one quarter of the artery and stenosis is removed for viewing)[12]

#### 1.6: Biomechanics of AA

Experimental investigations of blood flow biomechanics in the vascular system have made a significant contribution to the understanding of vascular diseases and long-term consequences of surgical repair. An efficient biomechanical formulation approximates all types of soft tissues according to the accurate range of the tissues deformation [13]. This aims to understand the general model of the soft tissue behaviour based on parameters involved in their material response. Thus, using applicable geometries from the complex structure, this constitutive model is feasible to be reconstructed in a Three-Dimensional (3D) Finite Element Method (FEA) [13]. The performance and physical mechanisms of the numerical model are in accordance with the mechanical response of tissue physiology, i.e. when soft tissues are subjected to blood load pressure, the change in geometry is considered. In clinical procedures, the tissue may endure irreversible deformation and plastic deformation could be used to represent arteries [14, 15].

### 1.7: Numerical Modelling using Computational Method

Computational modelling offers an attractive alternative to blood vessel study with the expansion of CFD to investigate the blood dynamics in arteries by adding more physical aspects that are related to blood. It also has the potential to predict the clinical outcomes based on a variety of factors including the arterial wall composition, surface anatomy and hemodynamic forces [16]. This investigation is based on solving fluid dynamics equations such as the conservation of energy and continuity equations which are used to develop and optimize devices and system design at minimal cost. Hence, it is worth encouraging more biomedical related researchers to examine the circulatory system through numerical modelling systems. This method offers accurate stress simulation results that show the effects on the vessel wall from the dynamic blood flow. As a result, the output from CFD models can be used for further understanding the risk of disease according to hemodynamic stress relations [17, 18].

### 1.8: Closure

This chapter discusses the basic fundamentals related to AA disease. The introduction of the disease and its possible threat were briefly summarized as an introduction to the research that will be described later. This chapter also gives an explanation the reliable tools for aneurysm assessment and the vital characteristics that are feasible from the assessment. To understand the effect of these diseases, it is necessary to comprehend the biomechanics of the vessel wall through computational modelling that has an ability to describe the hemodynamics of the disease. The next chapter will review the existing literature related to aneurysms and possible parameters that can contribute towards rupture.

## CHAPTER 2: LITERATURE REVIEW

### 2.1: Introduction

Many factors such as high blood pressure, diabetes, family history and smoking lead to aneurysms. However, the clearest evidence that the occurrence of abnormal arterial dilation is not totally dependent on those contributors because it still remains under investigation. Since AAA occurrences differ from patient to patient, researchers formulated different approaches to investigate the feasible contributors. This study may lead to the conclusion that aneurysms could lead to rupture and that there are possible ways to predict and avoid it.

This chapter reviews the possible aneurysm risks and factors parameters that have been studied by previous researchers in Section 2.2. This is followed by an analysis of the mechanical and physiological characteristics of aneurysm observations in Section 2.3. This chapter also considers existing aneurysm rupture detection and prediction methods in Section 2.4 before examining assessment methods in Section 2.5. Aneurysm tissue analysis, mathematical models and rupture theory are discussed in Sections 2.6-2.8, respectively. Computational modelling and the Fluid Structural Interaction (FSI) approach are reviewed from an engineering point of view in Section 2.9 and 2.10, respectively. A summary of the literature and the objectives are presented in Section 2.11 and 2.12, respectively. Section 2.13 presents the outline of this thesis with a Closure in Section 2.14.

## 2.2: General AAA Risk

AAA rupture remains one of the most significant causes of death in developed countries [19]. In AAA, there is an enlargement of the abdominal aorta from renal arteries to the bifurcation region. Clinically, the risk of rupture is directly related to aneurysm size and continues to be associated with high morbidity and mortality [20, 21]. Further, it has been reported that patient-specific biomedical factors may significantly affect the rupture risk and must be considered if a decision regarding surgery is to be made [21]. A number of researchers have used different numerical techniques such as the Finite Element Analysis Rupture Index (FEARI) [20], Rupture Potential Index (RPI) [21, 22], severity parameter (SP) [1, 23] and other geometric factors to predict the risk of rupture. However, these methods remain to be validated for practical purposes. [1, 20, 22]

An aneurysm diameter of 5.5 cm is clinically considered as the critical point marker for a patient to be fully monitored or to undergo elective repair surgery [8, 24]. Conducting surgery in advance on patients (who may not be at risk of rupture) is expensive and may expose them to unnecessary risks. Hence, there is a need for a relatively accurate prediction method which considers a patient's specific biomedical factors with minimum or no invasiveness.

### 2.2.1: Aneurysm Factors Parameters

Most aneurysm investigators have tried to find the AAA rupture mechanism in various ways, including studying the changes of mechanical properties in the arterial wall for risk prediction. Lanne et al. [25] and Sonesson et al. [26] found that the aortic stiffness of the aneurysm wall exponentially increases with age. Martufi et al. [27, 28] and Walters et al. [29] found that deviation in the physical structure such as wall thickness and progression of geometry with size

were very important parameters in rupture analysis. However, parameters such as enhanced wall thickness and geometry are not adequate to be observed as parameters without further clinical validation, especially *in vivo*.

### 2.3: Clinical and Mechanical Characteristics

Clinically, the integrity of the arterial wall relies on the major elements of the wall structure itself which includes elastin (as a dominant element), collagen and smooth-muscle cells. Based on this insight, Kleinstreuer and Li [1] concluded that the collagen-to-elastin ratio is the key element in determining the wall structure of the aorta. This was proven by an experiment by Fung [30] on the stress-strain curve for AAA material composition (see Figure 2.1). Composition changes lead to the alteration of wall mechanics, as an increased collagen-to-elastin ratio corresponds to a higher wall stiffness and lower tensile strength. The increment of proteolyt enzymes influences the collagen of the aneurysm wall deformation as measured by biomechanical parameters and criteria. This was proven by observing the amount of enzymes and the local inflammatory response of the aneurysm wall during collagen degradation experiments. [31]

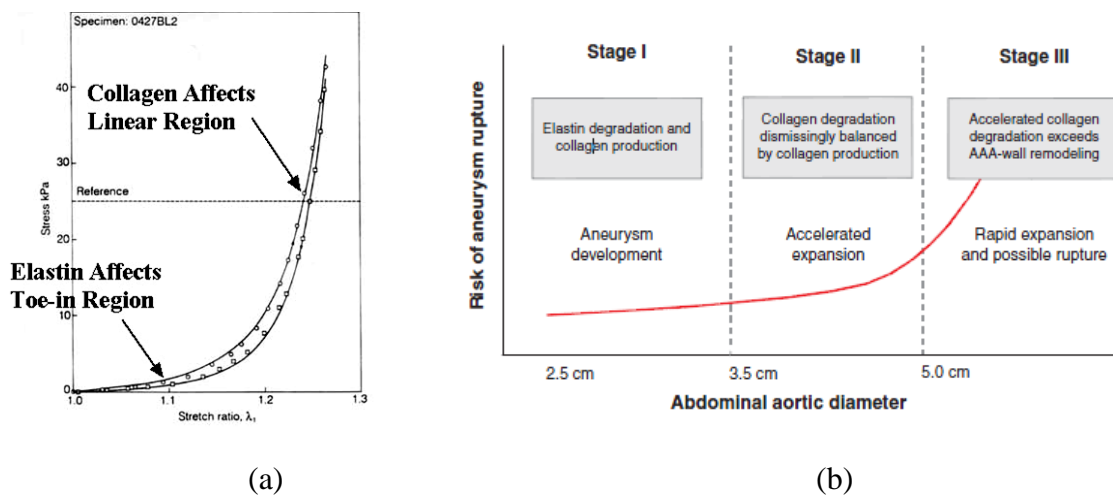
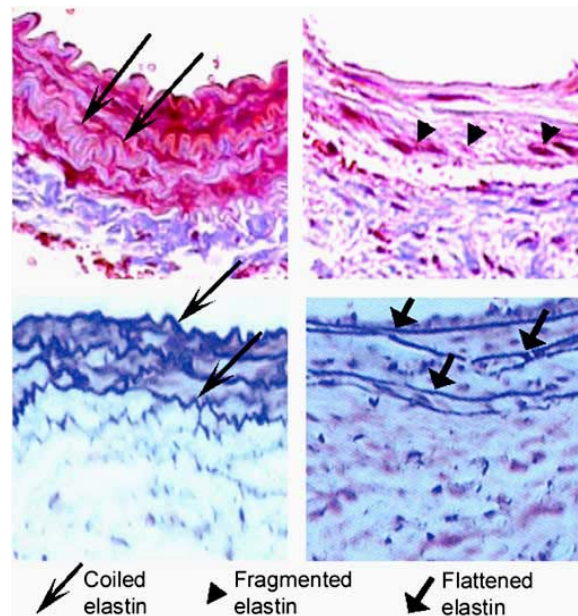


Figure 2. 1: (a) Collagen-Elastin composition curve in arterial wall) Adapted from Fung [29]; and (b) the three stages of AAA degeneration composition related to rupture from Kleinstreuer et al. [1]

Another clinical observation on this structural deformation is the disturbance of proteinase enzymes (notably Matrix Metalloproteinase (MMP) - 2 and -9) which contributes to the degradation of elastin and collagen [8]. Both enzymes function to invade inflammatory cells and stimulate its production on smooth muscles and fibroblasts [32]. Figure 2.2 shows the microscopic images of mice aorta specimens, which illustrate elastin degradation during AAA development. This study by Rentschler [32] used the *Doxy* drug to investigate how mechanical stiffness can be tested. This clinical observation explains the stages of AAA formation in the tissue in terms of structural composition after considering the changes of the collagen and elastin ratio in the wall.



**Figure 2. 2:** Histology of normal aorta (left) and aneurismal aorta (right). Adapted from [32]

#### 2.4: AAA Regenerated Model using US

The ultrasound modality is one of the simplest and most non-invasive tools for internal body assessment including blood vessel wall deformation. It estimates the vessel wall motion, geometry, diameter as well as thickness using proper designated Doppler analysis. A parameter related to arterial wall elasticity can be obtained by measuring the change in diameter of the artery [33]. By using a mathematical relationship to calculate the approximate changes in

arterial wall thickness, a prediction of the material elasticity in response to diameter deformation can be determined. The difference in cylinder diameters based on arterial diameter enlargement from the literature can be tested with a simple model of the disease. This method leads to an instant calculation based on the extraction of image input parameters which are defined either by looking through the image or display output from medical imaging tools. This method also includes the AAA formation, mechanical properties of the wall and internal blood pressure with appropriate velocity instantaneously.

## 2.5: Rupture Risk Detection and Prediction

The risk of rupture of an AAA relies more on the geometry or diameter of the aneurysm rather than other characteristics. In the case of AAAs, there is a number of factors which indirectly impact the aneurysm deformation in an arterial aneurysm. This includes annual growth-rate diameter expansion [34, 35], the presence of an intraluminal thrombus (ILT) inside arteries [36, 37] and blood wave speed [38]. Amongst these biomechanical factors, the threshold of the maximum AAA diameter and its growth rate are commonly regarded as major contributors towards rupture, from a clinical perspective [39]. However, recent studies have shown that additional parameters might also have an impact on the rupture. The rupture prediction aids the surgeon in recommending whether or not the patient should have an immediate surgical repair. The decision is based on the available parameters obtained from the patient during the treatment.

The multiple parameters available, according to the published literature [23], have been reviewed to identify the best prediction method. Clinically, a high expansion rate, which increases from 0.5 cm per year and over, is considered as a high risk of rupture [40]. Vorp et al. [41] indicated that instead of the additional expansion of diameter of AAAs, there is also

significant influence derived from mechanical stress due to the different asymmetry view point. Raghavan et al. [42] used ANSYS software to simulate an AAA 3-D model and found that an AAA with the diameter of 5.5 cm is insufficient as a single rupture predictor. By using individual computations of each aneurysm in their simulation, they found that the peak wall stress occurred anywhere from 45% of their failure strength and this is considered as a reason to suggest that AAA volume might be the best indicator instead of the diameter. Hua et al. [43] also found a similar result with the simple geometry model and characteristics; that there are insufficient variables to rely on when predicting AAA-wall stresses.

An alternative technique by Kleinstreuer and Li [1] considered a multi-parameter element and is shown in Table 2.1. By considering a multiphase factor when defining better predictions, the method has to start with the most important parameters in order to rank the highest contributor. In AAA wall aneurysm, a number of parameters are suspected to make a higher contribution, thus, prioritizing the most affected is necessary. Kleinstreuer and Li [1] chose 1) diameter, 2) annual growth rate expansion of the wall and 3) mechanical stress as their most significant parameters to generate the biomechanical weighted factor in descending order. Gasser, Biasseti, Bluestein, Tong, Vande Geest and Wang [36, 44-49] perceived from their study that the ILT also affects the biomechanical factors and it must be considered as a parameter for patient-specific rupture predictor analysis.

Myers and Faggioli [50, 51] described the importance of a small diameter of the abdominal aorta (between 1.9 and 2.6 cm) which has the potential to rupture based on the gradual increase of maximum diameter observed. Meanwhile, Kleinstreuer and Li [1] discovered that by classifying the category of maximum to minimum diameter, the rupture risk chances decreased accordingly. Therefore, it is not entirely necessary to respect this estimated threshold value for

interference as clinical investigation holds 5.5 cm as a critical value for elective repair surgery [1]. It is clinically proven that a smaller aneurysm diameter has less potential to rupture compared to a larger one [51-53]; however, we still have to take possibility into account while investigating the rupture wall in an aneurysm because the risk of rupture is more important than the size of deformation.

The expansion rate of wall deformation is another key indicator for rupture [52-54]. This parameter is observed by continuous monitoring since AAA was diagnosed in specific patients with abnormal diameter [55]. The expansion rate rapidly increases when the diameter is more than 5.5 cm, which means the aneurysm wall is highly inclined to rupture, thus elective repair should be immediately commenced. This is in line with the study of Wolf et al. [56], which suggests that if the expansion rate reaches more than 0.5 cm/year, elective repair should be considered, even if the maximum diameter at that time was below 5 cm. However, this expansion rate correlates with the diameter at the end because of the geometry factors based on the prior study by Kleinstreuer and Zhonghua [23]. Moreover, this research alternatively proposed the use of the principle of true stress-strain engineering to determine the ultimate strength of material during aneurysm development.

Table 2. 1: Severity Parameter Factors Table from Kleinstreuer and Li [11]

BF <sub>i</sub>	Definition	Reported ranges of biomechanical factor (BF <sub>i</sub> )				Weighted factor w <sub>i</sub>
		Low risk	Middle risk	High risk	Danger zone	
<i>i</i> = 1: Diameter ratio	$\frac{d_{AAA,max}}{d_{AA}}$	1.5 ~ 1.9	2.0 ~ 2.4	2.5 ~ 3.2	≥ 3.3	0.20
<i>i</i> = 2: Expansion rate (per year)	$\frac{(d_{AAA,max} - d_{AAA,max}^{previous})}{d_{AAA,max}^{previous}}$	0.01 ~ 0.04	0.05 ~ 0.09	0.10 ~ 0.17	≥ 0.18	0.25
<i>i</i> = 3: Stress ratio	$\frac{\sigma_{AAA,max}}{\sigma_{AA}}$	1.5 ~ 2.0	2.1 ~ 3.0	3.1 ~ 4.3	≥ 4.4	0.15
<i>i</i> = 4: Diastolic pressure ratio	$\frac{P_{dia}}{90\text{mmHg}}$	0.83 ~ 0.9	0.91 ~ 1.0	1.1 ~ 1.16	≥ 1.17	0.12
<i>i</i> = 5: Asymmetry index	$\frac{d_{AAA,max} - l_a}{l_a}$	1 ~ 0.9	0.7 ~ 0.8	0.5 ~ 0.6	≤ 0.4	0.07
<i>i</i> = 6: ILT-AAA ratio	$\frac{A_{ILT}}{A_{AAA}}$	0.1 ~ 0.24	0.25 ~ 0.44	0.45 ~ 0.61	≥ 0.62	0.07
<i>i</i> = 7: Stiffness decrease (per year)	$\frac{E_p - E_p^{previous}}{E_p^{previous}}$	0.01 ~ 0.03	0.04 ~ 0.06	0.07 ~ 0.09	≥ 0.1	0.07
<i>i</i> = 8: Saccular index	$\frac{d_{AAA,max}}{L_{AAA}}$	≥ 0.71	0.66 ~ 0.70	0.61 ~ 0.65	≤ 0.6	0.07
Assigned BF <sub>i</sub> threshold value		0.1	0.3	0.7	1.0	

Another important parameter of the arterial deformation analysis is mechanical stress, which is determined by the peak wall stress in AAA rupture investigations. General stresses normally measured as arterial wall stress are considered in most AAA rupture analyses, which include longitudinal, circumferential and Von Mises stresses [1, 57-64]. Most results from the previous studies are based on numerical assumptions in computational analysis since the stress measurements are not available *in vivo*. However, the mechanical stress of the wall has been proven to be a major contributor to the wall rupture through computational simulation [64, 65]. Furthermore, with the complexity of rupture mechanisms and geometry, it is difficult to determine wall stress for a specific patient without any computational devices to compute the stress. Raghavan [42, 66] found the results through ANSYS package (ANYS Inc.) simulation by considering the wall stress to determine the rupture predictor criterion. Similarly, Fillinger et al. [24, 58] in their study also suggested that the peak wall stress seems to be superior to maximum diameter in rupture prediction. Moreover, the study from Thubrikar [40, 62] found that the different regions of an AAA had different yield stresses, yield strains and other mechanical properties.

## 2.6: Stress-Strain Relationship in Tissues Behaviour

Stress and strain are important moduli in assessing the potential failure in machine parts [22, 67, 68]. The term strain is also used to define the intensity and direction of the deformation at any given point with respect to a specified plane within a solid body. A relation between both stress and strain is crucial in recognizing the difference between engineering and tissue biomechanics in terms of its first principles. According to the existing data on the mechanical properties from the literature, stress and strain definitions were used to determine the elasticity of the aneurysm wall under diverse testing approaches. Fung [30] stated that since the artery behaves as a membrane, the stresses of concern and the strain principle are dependent on its

circumferential and longitudinal elongation and stretching. This is because of the fact that most of the blood vessels are asymmetrically deformed due to haemodynamic factors. Referring to that, to understand the tissue behaviour, there are different interpretations in determining the real tissue mechanical properties.

Two types of stress and strain curves that need to be considered when determining material behaviour are detailed by [69]. The ‘engineering’ stress and strain (Equation 2-1 and 2-2) are determined from the measured load and deflection using the original specimen cross-sectional area  $A_0$  and length  $L_0$  as

$$\sigma_e = P/A_0 \quad (2-1)$$

$$\epsilon_e = \delta/L_0 \quad (2-2)$$

When the stress  $\sigma_e$  is plotted against the strain  $\epsilon_e$  an engineering stress-strain curve such as that shown in Figure 2.3 is obtained.

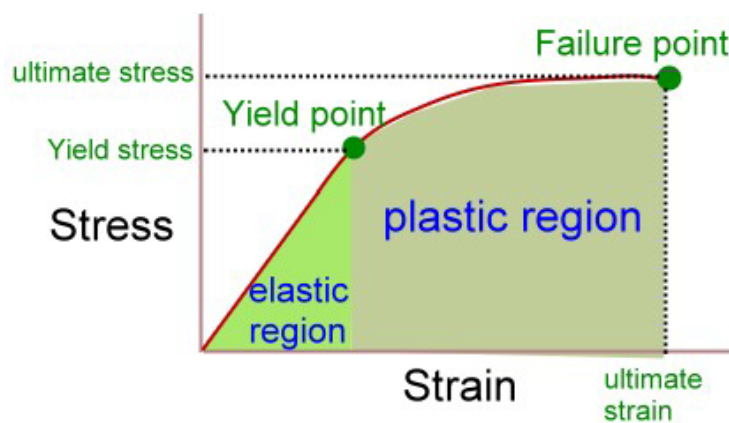


Figure 2.3: Stress-strain curve from stress-strain relationship in engineering

Since the specimen dimensions experience substantial change from their original values, the engineering stress-strain curve must be determined with caution beyond the elastic limit. Due to this consideration for real tissues, using the true stress  $\sigma_t = P/A$  rather than the engineering stress  $\sigma_e = P/A_0$  can give a more direct measure of the material's response in the plastic flow range. A measure of strain often used in conjunction with the true stress takes the increment of strain to be the incremental increase in displacement  $dL$  divided by the current length  $L$ . Table 2.2 summarizes how previous researchers have defined the material properties based on tissue testing (uniaxial or biaxial).

Table 2. 2: Summary of Stress-Strain Definitions used to Determine the Elastic Modulus Aneurysm for the Thoracic Aorta [70]

Reference	Stress	Strain
<sup>4</sup> Iliopoulos et al.	True	Engineering
<sup>11</sup> Vorp et al.	True	Engineering
<sup>12</sup> He and Roach	True	Engineering
<sup>13</sup> Thubrikar et al.	True	Engineering
<sup>14</sup> Raghavan et al.	True	Engineering
<sup>15</sup> Choudhury et al.	Engineering	Engineering
<sup>16</sup> Emmanuel and Dimitrios	Engineering	Engineering
<sup>17</sup> Sokolis	Engineering	Engineering
<sup>1</sup> Khanafer et al.	True	True
<sup>2</sup> Duprey et al.	True	True
<sup>19</sup> Iliopoulos et al.	True	Almansi—Hamel
<sup>20</sup> Sokolis et al.	2nd Piola—Kirchhoff	Green—St. Venant
<sup>21</sup> Okamoto et al.	True	Green—St. Venant

O'Rourke [71] and Fung [72] agreed that the problem of characterizing arterial mechanical stress is due to the complexity of the arterial system with regards to each and every point. The elastic properties of the arterial wall are nonlinear and the physical and chemical wall properties may vary at different points [61]. The lengths and angulations of the geometry change instead of having an obvious circumferential deformation during the development of AAA [32, 73,

74]. However, in order to measure the diameter, the presence of an ILT inside the aneurysm has to be ignored due to its insignificant impact in reducing the wall stress [62]. The presence of an ILT is likely to be perceived as resilience (elastic region in Figure 2.3) in the stress-strain relation, which is capable of absorbing energy even though it represents the area under the stress-strain curve up to the yield point. Consequently, other research findings [36, 44-49] have highlighted the importance of the ILT being part of the risk rupture assessment; it is also vital to consider its limitation in material deformation at the yield point. At this point, the mechanical properties of a material cannot be elastically absorbed by the load due to its elastic limit boundary before it changes to the plastic region [75, 76].

The theory of engineering material endurance for the force-elongation relationship [76] in tissue regions is used for reference purposes. This region is used for uniaxial and biaxial testing on the excised aortic tissues experiment conducted by most researchers to investigate the time taken for the tissue to break or rupture [32, 46, 47, 66, 77-79]. Kim and Baek [80] in their study found that circumferential stress has more correlation with the stress-strain relationship compared to other characteristics. By observing the strain deformation and the circumferential stresses during pressurization in the porcine aorta, they found that the aortic wall thickness is changed gradually along with the circumference stress. Vorp et al. [63, 81] stated that, in addition to diameter, the influence of mechanical wall stress in AAAs is very important because previous researchers were using different approaches to correlate the stress-strain relationship in order to better understand the wall tissue mechanical properties.

The graphs by Di Martino [82] in Figure 2.4, which show the change in ultimate tensile strength (UTS) of material with the diameter and thickness, illustrate a significant comparison technique in defining the correlation between both parameters. This is because the failure criteria predict the ultimate strength based on different combinations of the main

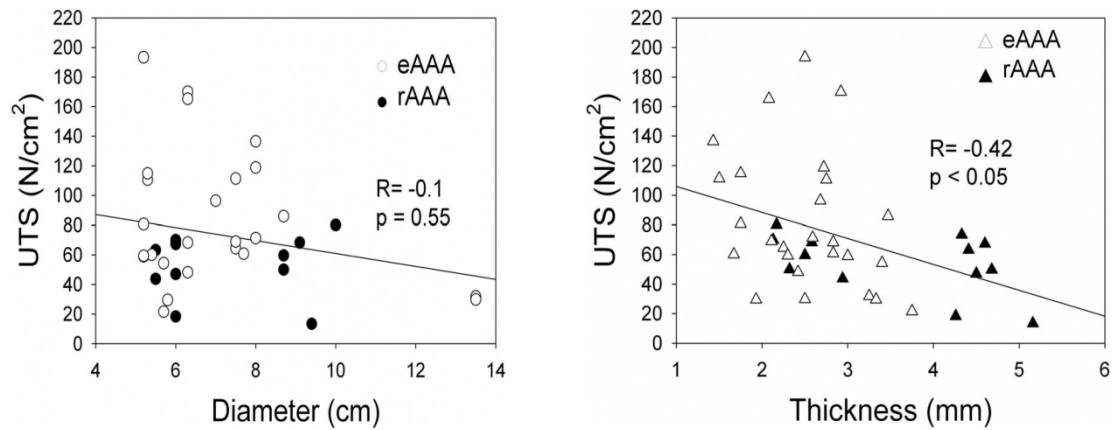


Figure 2. 4: Uniaxial testing on excised human AAA after surgery for validation [82]

failure modes, which are longitudinal, circumferential and shear [83]. The maximum stress theory of fracture assumes that fracture occurs when at least one of the stresses in the principal directions reaches a critical strength which eventually leads to a rupture [68].

## 2.7: Mathematical Model for Elongation

Modelling the deformation of the tissue vessel behaviour by mathematical methods refers to the spontaneous movement in various axes of the wall. It investigates not only how the aneurysm is constructed from the stiffness factor of the wall, but also relates to the stress endurance after it attains the yield point [76]. Fung [30] described that stress-strain relationship testing in two mathematical expressions, polynomials and exponential functions, where both methods were introduced by Chuong [84] and Ramesh [85], respectively since in 1972. Okamoto [86], however, proposed that by using strain energy functions as a function of the circumferential ( $E_{\theta\theta}$ ) and axial ( $E_{zz}$ ) strain, if the shear is not involved, the ratio of the mechanical stress for deformed and undeformed specimens can be determined. With this deformation, estimating the toughness of tissue material properties and the pathophysiology in terms of time is recognised to be crucial [87].

The intention of the present research is to consider the entire history of deformation especially from the time the plastic (or nearly plastic) region was created [76]. It seems to increase the complexity of understanding by involving the stress and the time rate of strain. However, the equation would be analogous to the equation for flow of a viscous fluid, and the strain at any given time would be determined through step-by-step integration over the entire strain history.

## 2.8: Artery Biomechanics: Rupture Theory

Failure or rupture can occur when the endurance of the vessel wall is compromised by continuous exposure or if the wall stiffness becomes weak. Thus, it is desirable to accurately determine the mathematical relationship between the pressure and endurance in determining the maximum strength limit with varying wall ratios [75, 76, 88, 89]. By conducting experiments on specimens or similar materials to determine the relationship between biomechanical stress and strain and rupture, it is expected that an understanding of the fundamental mechanism of wall rupture will be achieved. The numerical experiments have also described the behaviour of more realistic models in which the geometry and composition of the wall material are obtained based on physical impact [36, 61, 90-93]. Wang [94] simulated the viscoelastic behaviour by using load control data to identify the failure criterion on collagen fibre. The maximum stress failure criterion is independently based on tension failure in the material's maximum direction of elasticity [95] and endurance of plasticity of the material by referring to metal fatigue and fracture engineering theories [75].

In this research, the fatigue failure under repeated loading pressure within the frequency domain [96-98] was observed until it noticeably establishes a general criteria for the failure, which can be used as a prediction marker. By taking into consideration the history of the deformation and weakest point, a potential rupture mechanism based on time estimation was identified.

## 2.9: Computational Simulation and Modelling in Rupture Prediction

To understand the stress and strain principle, it is necessary to study the mechanical properties of the materials. In biomechanical studies of the tissue material of the vessel wall, the main factors that contribute to the rupture have been broadly investigated, yet the key contributors have not been found. In determining a numbers of factors, Kleinstreuer and Li [23] pointed out the idea of combining all the parameters that may make possible contributions to the wall vessel dilation and rupture by introducing their method called the Severity Parameter (SP).

This method requires computer analysis and needs to be validated with CFD modelling. This approach will also help researchers to do further study on the disease *in vivo* since it is capable of producing consistent and efficient results. Several studies [36, 61, 92, 99, 100] suggest that the stress in the diseases (dilated wall arteries) is much higher at inflection points and bifurcation region in aneurysm compared to non-aneurysm by using 3D simulation software including flow dynamics, meshing techniques and solid mechanics. Another study by Tan, Helderma, Venkatasubramaniam and Vande Geest [61, 65, 101, 102] found that rupture prediction showed that peak wall stress in an aneurysm had a higher sensitivity and specificity than the maximum diameter. Previous studies [1, 29, 44, 99, 103] demonstrated that computational capabilities were used with the aim of providing a better understanding of the fundamental fluid and solid physics in the aortic artery and its branches. These studies encourage other researchers to enhance and explore in detail how solids and fluids interact with one another, thus simulating a model for arterial diseases.

## 2.10: Computational Simulation and Modelling Fluid-Structure Interaction (FSI)

Recently, many researchers have favoured a fluid-structure interaction approach to model the aneurysm in CFD modelling, in order to investigate the interaction between fluid and solid accurately [73, 104, 105]. This approach includes the analysis of significant increases in computational time comparison of elements especially the wall stress accuracy, which corresponds to blood flow in arteries. Fraser [106], Di Martino [107], Shahcheraghi [108] and Doyle [20] in their analysis have used the features of CFD modelling called fluid-structural interaction as the wall structure boundary to identify the different components in the model. Their findings may allow the possible identification of the region potentially at risk of rupture.

The most important aspect of combining the two elements in the simulation model is the boundary element between solid and fluid [109, 110]. This is because blood vessels are flexible; therefore the interaction between blood flow and arterial wall deformation may involve a wide range of fluid-mechanical phenomena. The flow will affect movement of the walls which in turn will influence the flow field [111, 112]. In order to adapt analytical experiments into a numerical experiment, it is necessary to observe the behaviour of AAA wall tissue under mechanical stresses for FSI modelling. For this reason, simultaneous fluid-structural interaction should be considered when studying the hemodynamics and biomechanics [113-115] of blood vessels. At the moment, most of the FSI research work focuses on the simple blood vessel. For example Zhao et al. [116] investigated the effect of blood vessel elasticity on wave propagation and local flow pattern based on fluid-solid interactions in arteries and indicated that the wall characteristics can be included as a tool to predict the hemodynamics of blood flow in a clinical context. Other studies by Tang et al. [117, 118] simulated cyclic arterial compression using an unsteady 3D model with FSI and they obtained reasonable agreement with experimental results.

Employing a FSI in modelling, Finol [71], Samarth [94] and Scotti [95] performed fluid and structural analysis of an aneurysm model and had proven that FSI simulation allowed for computation of the flow and pressure field in the aneurysm which simultaneously move with the wall stresses. This proves that the computational simulations with clinical diagnostic data are correlated. Therefore, this simulation model by utilizing FSI will provide accurate results of the solid and fluid boundary region. Many researchers also use a standard range of wall thicknesses ranging between 1.5 to 2 mm to run a simulation without considering that the result is highly dependent on this value [93, 119, 120]. This modelling assumption input will lead to uncertainties with respect to the real AAA geometry.

### 2.11: Summary

From existing research, there are some gaps that need to be covered in developing a rupture prediction technique. The existing prediction methods can still be enhanced especially pertaining to precise model design with actual geometry from the specific patient. Even though a number of approaches to predict rupture have been proposed [21, 23, 62], they have never been evaluated *in vivo*. In addition, the models being used are based on a uniform thickness assumption of the arterial wall which is not an accurate representation of tissue structure. Using commercial analysing software such as ANSYS, ABAQUS, ADINA, and FIDAP to analyse the medical images is unreliable for prediction if without experimental validation. Moreover, the parameters obtained for a specific patient cannot simply determine other patients' conditions since the studies [60, 98] show that there are numerous differences between the parameters for different patients. This research focuses on investigating possibilities of rupture prediction techniques based on tissue biomechanical properties and blood flow characteristics. It will consider reviewing the risk of aneurysm rupture through the estimation of time period based on the current condition of the patient directly from an US system. It is anticipated that

this work will determine the *in vivo* distribution of stresses and the material strength of the abdominal aorta wall directly from the proposed correlation of design parameters. It also enables us to determine and estimate the influence of various parameters on wall stress. To be quantified, a diagnostic setting will be useful in predicting the AAA rupture, we propose the strain energy with time estimation over progressing period from the aneurysm patient.

In this research, the accuracy of stress distributions in specific regions of the model will be comprehensively investigated to estimate the rupture region. Since this simulation is valid as close attention is paid to the wall stress distribution in any aneurysm that subsequently ruptures, the effect of other relevant factors on wall stress, such as the rate of change of blood pressure [121, 122] and strain deformation [118] could also be explored as part of a dynamic stress analysis. This estimation will be used as confirmation in this research when proceeding to numerical studies.

## 2.12: Objectives

Using data developed by a relatively cheap modality method, namely US, the main objective of this work is to investigate and understand the geometrical deformation and strength characteristics of AAA. Specific attention focuses on understanding how these characteristics are correlated with AAA rupture and its estimation. Thus, the specific objectives of the work can be summarized as follow:

1. Obtain US data for patients with AAA in order to investigate the possibilities of developing a Patient-Specific Aneurysm Rupture Predictor (P-SARP).
2. Incorporate this data into geometrical and simulation studies.
3. Use numerical simulation to develop AAA shapes and determine locations of critical variables such as maximum stress, strain and energy.

4. Thereafter, determine critical rupture parameters which can be used to predict a possible failure mode.
5. Since there is no well defined failure mode for AAA rupture, alter available material failure theories and investigate how they can be used to predict AAA rupture.
6. Use experimental data to justify and validate the hypotheses proposed in 5 above.

### 2.13: Closure

This research intends to develop an insight into patient-specific and instantaneous predictor methods that can guide clinicians to assess aneurysm rupture risk more accurately. The main features of the proposed method are the fact it is based on instantaneous assessments of ultrasound readings which are normally obtained for AAA patients. The proposed method takes into consideration patient-specific biomechanical parameters such arterial elasticity, size and conditions, which are extracted from patient US image data. CFD techniques will be incorporated to investigate the FSI between the blood flow and the arterial walls and determine critical stresses and strains to formulate necessary algorithms. In determining their findings, most researchers have to validate their results from sample population treatment record history or human autopsy investigations or animal specimen tensile testing. These validations, however, are insufficient to support clinicians to implement those theories. Since it is difficult to accurately estimate rupture occurrence from the hemodynamics of human tissues, this research aims to implement a technique that assesses patient-specific data *in vivo* and propose an approach that will be used from the same patient record for validation. In this research, the proposed technique will be novel as it will be based on available parameters, which are easily identified and can be obtained from the ultrasound images taken from different directions.

## 2.14: Research and Thesis Outline

This study will focus on a more accurate identification of AAA patients who are at high risk of rupture and limits low risk patients from undergoing invasive procedures by targeting treatment. In contrast to previous research, the approach offers significant benefits in terms of complementary, safe and reliable results that are also economical. The proposed research layout is presented in Figure 2.5 for systematic research flow. Four major elements that will cover the fundamentals are discussed in consecutive chapters and are outlined as follows:

1. Analyse the most-weighted parameters that *non-invasively* contribute to rupture prediction study [23] to liaise with US limits parameters.
2. Tissue failure experiments are used to further understand the failure mode of the tissue based on real tissue specimens, to define the interrelation between the failures.
3. Numerical study discusses the *in-vivo* US data collection technique that can be segregated between a normal pre-screening aneurysm patient and the proposed P-SARP method.
4. Validation techniques to evaluate the aneurysm progress over a period of time for each patient subject.

In Chapter 3, there will be an overview of the theory towards the tissue rupture. Chapter 4 discusses the medical imaging data collection method as a fundamental method of the simulation process to define parameters from US for further analysis. It also explains criterion for the parameters to be measured during data collection. (From the vascular outpatient department at Manukau Super Clinic, Manukau)

Chapter 5 determines the accuracy of using stress distributions in specific regions of the model. Here, the rupture postulation is based on wall stress distribution in any aneurysms that subsequently rupture. The effect of other relevant factors on wall stress, such as rate of change

of blood pressure [121, 122] and strain deformation [118] could also be explored as part of a dynamic stress analysis. This estimation will be used as priority in predicting the wall rupture.

In Chapter 6, the wall rupture prediction from US imaging is discussed along with proposed failure theory from Chapter 3. Chapter 7 analysed and discussed the rupture theories in Chapter three when comparing with high risk parameters towards rupture prediction discussed in Chapter 6. This is followed by conclusion to summarize the research findings and offer future recommendation.

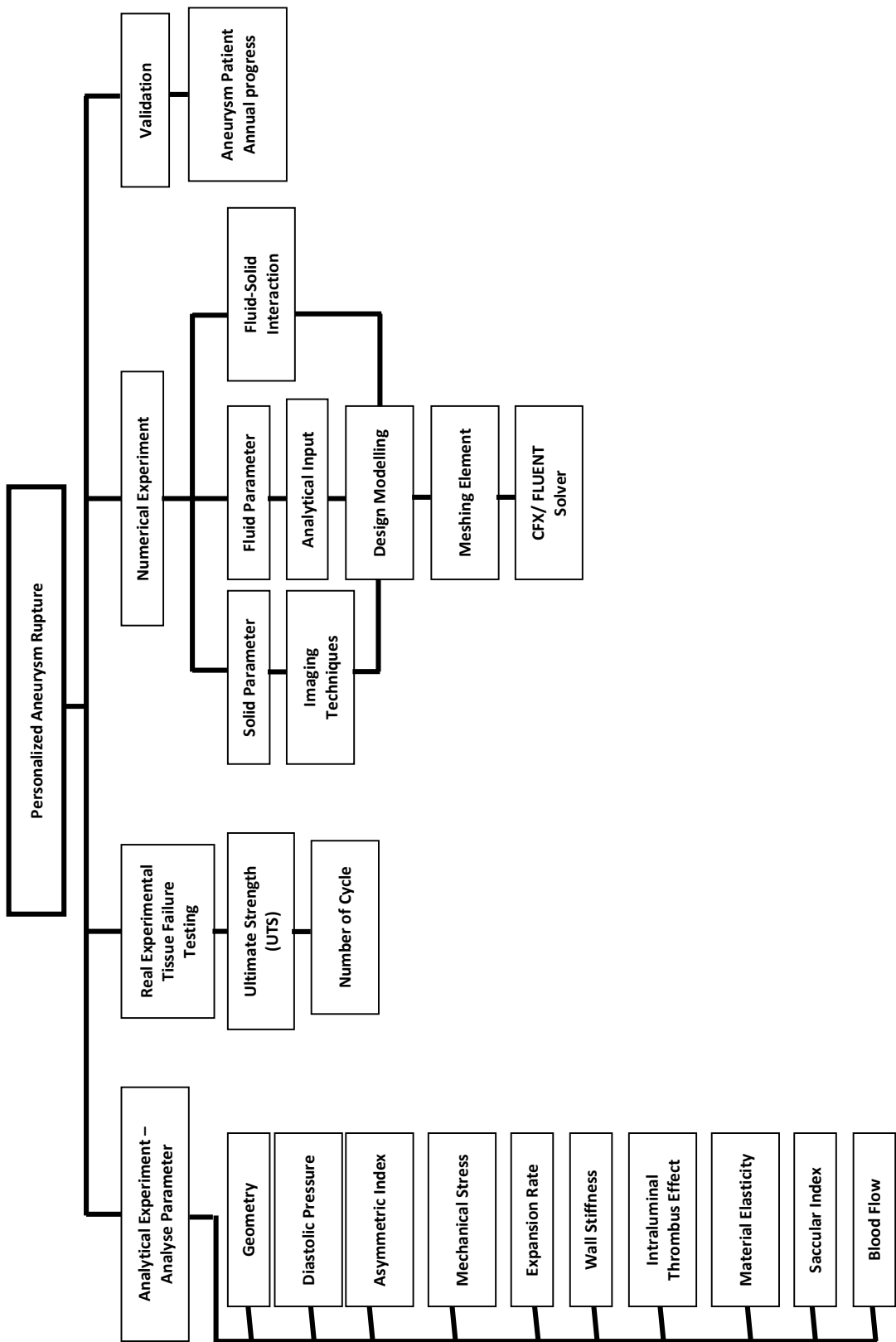


Figure 2. 5: Research layout

## CHAPTER 3: MODEL FORMULATION

### 3.1 Introduction

This research focuses on investigating the AAA rupture prediction by using computer simulation for data collected from US measurements. This is a two-fold chapter. It presents the background theories for failure prediction followed by the basic theories used in the simulation program ANSYS. First, this chapter presents an overview of possible failure modes which could be implemented to predict AAA rupture. To use any of these modes, determining a thorough map of stress, strain and energy distributions are essential before any prediction is made. These variables will be determined using computer simulation.

Second, in principal, ANSYS will be used to determine the stress, strain and energy distributions around an AAA section and then use an appropriate hypothesis to predict rupture. Thus, failure modes and the background theories for the ANSYS simulation software are presented in this chapter.

### 3.2 Tissue Failure Overview

AAA tissue is a complex multilayer structure with hyperelastic-viscoelastic-like characteristics. Developing a simple straight forward algorithm to predict rupture is not an easy task. However, looking at standard materials and how they fail helps one to understand the mechanism which contributes to tissue failure. Thus, two scenarios are considered in this work and are introduced as follows.

Since the tissue is exposed to pulsating loads due to the heart beat and blood flow, fatigue failure may be considered as an option. There is limited reference to this in the open literature.

In fact, the only work in this area is that by Gilpin [123]. If we consider fatigue failure as an option, then it may be possible to determine an endurance limit and number of cycles which helps to estimate the total time required until rupture.

If accumulated damage is taken into consideration, then the total energy required to introduce failure maybe estimated over a period of time. From this an estimator could be made for the total time required to accumulate this energy and determine the time required for rupture.

The second approach is based on some biaxial state of shear test. Since there is limited data available on this, collaboration with a group in Japan was initiated which allowed access to AAA human tissues. From the data one can estimate the total energy required for rupture. Using computer simulation we can obtain the total energy generated from each cycle. Combining these values will help to develop a prediction indicator.

The relation between load cycles as a mean of the areas and the energy dissipation (hysteresis loop) rely on the stress-strain relationship of the material, which is used to determine the fatigue of the tissue before its failure. The rupture strength of this strain exhibits plastic behaviour and reaches its maximum value when the strain energy ( $W$ ) per cycle decreases. This state represents strain deformation leading to zero ( $\Delta\varepsilon \rightarrow 0$ ) where the corresponding changes of rupture strength energy ( $\Delta U_f$ ) changes towards zero. The significance of the strain energy approach is its ability to obtain data from human subjects. From another perspective, when the strain reaches static value (maximum deformed) the number of loading cycles may be calculated. Using Stress-Cycle (S-N) curve, the accumulated energy to failure which will help in estimating the number of cycles to ultimate rupture stress is investigated.

The major elements to be postulated based on the two scenarios are further discussed in Chapter 6 and are as follow:

1. Strain energy per unit time ( $U_T$ )- where the rupture is based on energy determined from stress-strain testing of tissues specimens (Figure 3.1) as described by Sugita [124].
2. Tissue endurance limit ( $\sigma_e$ ) based cyclic-loading of the pressure – where the rupture is estimated by the number of cycles from the S-N curve prediction using the Goodman fatigue relation[123].

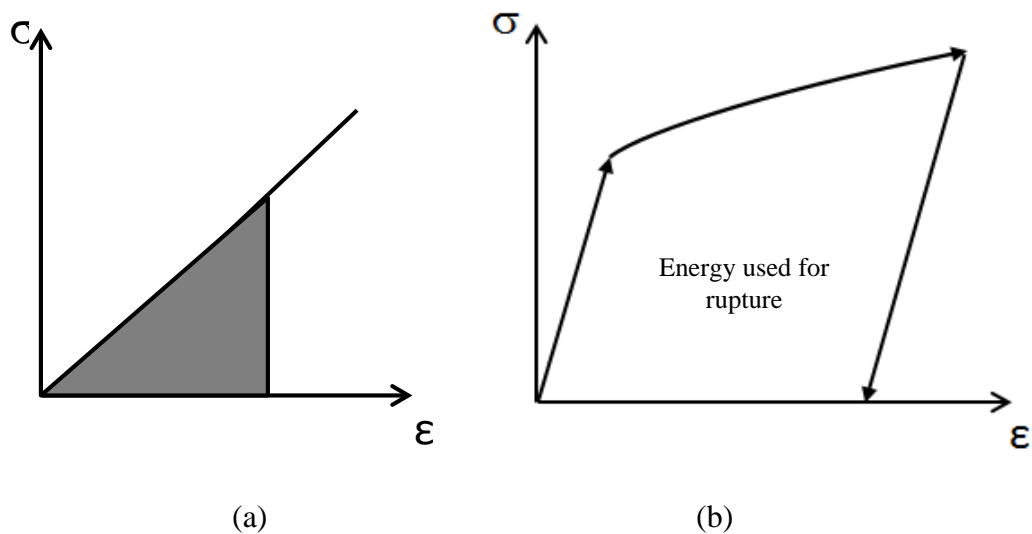


Figure 3. 1: a) Strain Energy is the area under stress-strain curve and; b) Energy Loss is the area under the stress-strain loop [69]

To develop an understanding of failure, one has to decide what failure variables or parameters to use. In the following section, a summary is presented to briefly discuss the main variables used in this investigation. Although these parameters have been used for standard materials, they may help us in identifying proper failure prediction methods for tissues.

### 3.2.1: Strain Deformation

As mentioned earlier, the mechanical characteristics of arteries deform at every pulse cycle repeatedly. It is also possible to define the behaviour of blood flow and the compliance of the arterial wall. The straining effect due to this strain deformation occurs because of the dilated vessel wall from the aneurysm aorta and can be governed by the following strain equation.

$$\varepsilon_{ij} = \frac{1}{2} \left( \frac{\partial U_i}{\partial x_j} + \frac{\partial U_j}{\partial x_i} \right) \quad (3-1)$$

Where  $U = U_1, U_2$  and  $U_3$  represents the displacement vector of computational grid-points of the arterial wall in three directions.  $i$  represents the strain direction and  $j$  represents the area.

The strain deformation is considered when investigating aneurysm models due to its dependability on the flow equation, the pressure-diameter response and the equation of equilibrium. This situation could lead to possible correlations between strain deformation effects with the development of cardiovascular disease and thus establishing a new relationship.

### 3.2.2: Equivalent Stress

Among the events that occur during testing, ‘the maximum-distortion-energy-theory (also called Von Mises stress theory ( $\sigma_{VM}$ )) is the one with the finest agreement with experimental evidence where the energy obtained will cause a change in deformation [68]. This Von Mises equivalent stress theory is based on the failure due to distortion of that portion which is capable of predicting the elastic failure when reaching the maximum limit. Concerning to the physiological theory of the blood tissue which is more to wall-shear related [10, 118, 125-128] (shearing caused by distortion), we apply the Von Mises Stress theory given by:

$$\sigma_{VM} = \sqrt{\frac{(\sigma_1 - \sigma_2)^2 + (\sigma_2 - \sigma_3)^2 + (\sigma_3 - \sigma_1)^2}{2}} \quad (3-2)$$

Where  $\sigma_1$ ,  $\sigma_2$  and  $\sigma_3$  are the principal stresses obtained from the equation which is originally equated from the energy of cylindrical surfaces and this is completely in line with the original physical cylindrical form of the blood tissue before aneurysm. Therefore, the maximum-distortion-energy theory predicts elastic failure when the von Mises stress reaches the maximum strength or beyond; and distortion with various deformation patterns on the physical wall. This effect correlates with the history of the stress-strain relationship of the tissue specimen. The stress-strain behaviour is curving up to the point of failure (depending on the applied testing method) until abrupt failure occurred. This combines principal stress from the 3-D components  $\sigma_1$ ,  $\sigma_2$  and  $\sigma_3$  represented in the x, y and z direction, respectively in the 3-D modelling (Figure 3.2).

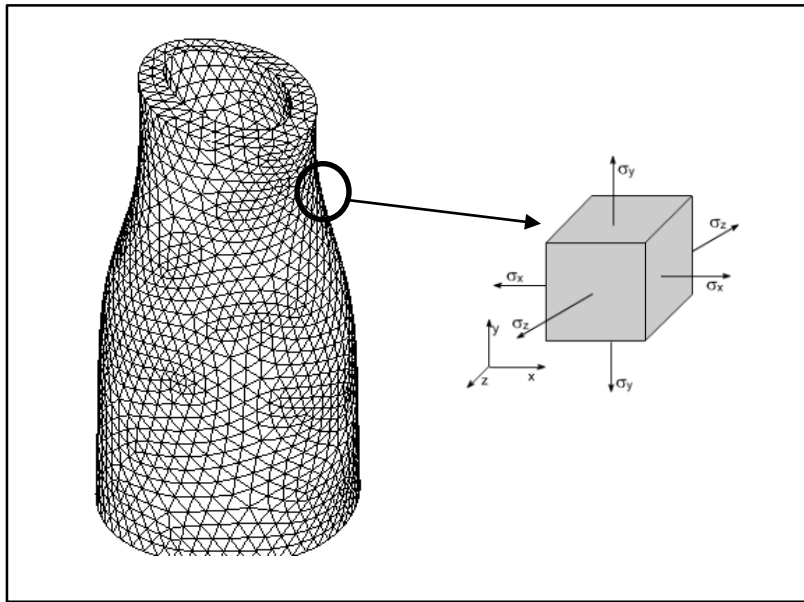


Figure 3. 2: Cartesian co-ordinates for the 3 dimensional stress shape deformation in FEM

### 3.2.3: Strain Energy

In this approach, the constant strain data are measured according to the formulated rupture model design. The strain energy is used to characterize the failure factors along with consistent strain values. On constant loading (pulsatile), the specimen deformation is continuously pressurized as generated from the heartbeat. Whenever, it reaches the constant strain, the time is measured. This factor is due to tissue hardening or fatigue (as will be discussed in the next section) after reaching the tissue yield strength. Using this approach, it would be possible to measure the amount of energy required from the stress-strain data beyond the elastic region.

This energy required for failure ( $U_f$ ) can be represented by;

$$U_f = \int_0^{\varepsilon_s} \sigma d \varepsilon \quad (3-3)$$

Where  $\varepsilon$  is strain and  $\sigma$  is stress from the stress-strain data curve and  $\varepsilon_s$  is rupture strain.

### 3.2.4 Stress Cycles

Before looking into more detail at the nominal stress using pulsatile waveforms, one must consider that modeling an aneurysm model with pulsatile waveforms is more complex than normal sinusoidal waveforms. This cycle known as distorted peak with certain observations made by approximated sinusoidal waveform (considering maximum amplitude and time period) [68]. The overall observation of the stress cycle is made to ensure that the fatigue behavior is directly affected by the shape and systolic pressure waveform. The magnitude of the mean stress in cycling plays an important role on the fatigue analysis where it relates to an arterial pressure to flow or volume change. The detail of this stress cycle will be further discussed in Chapter 6.

### 3.2.5 Total Life Curve

The total life curve is one of the methods used to understand the relationship between the fluctuating load and number of cycle to failure. It is widely used in applications where the applied stress is nominally in the elastic range of the material and the number of cycle to failure is large. It has also been recognized in metal subjected to a repeated load, which will fail at stress levels lower than that required to cause the fracture from the application of the load. From this point, the nominal stress method is best suited to areas that undergo a high-cycle fatigue process. In this failure theory analysis, we use the nominal stress approach at the required fatigue process that produces a high number of cycles based on strain deformation of the aneurysm model.

In this research, the changes of the angular displacement during size deformation are geometrically observed based on time. Every single point is measured according to the stress-strain curve model during loading pressure where multiple curves are plotted for a single

aneurysm case. In mechanical tissue testing, when a maximum elasticity is attained, stress fatigue will be considered based on estimation time, tracked from the intended stress and strain. All information will be incorporated into numerical implementation using computational modelling capabilities to rebuild the model in different stages to represent a single solution.

### 3.3 Computer Modelling

As previously discussed, ANSYS will be used in the current research to simulate AA rupture and determine the necessary variables (as discussed in the previous section). This section presents the background theories for the ANSYS simulation software. A collective set of streamlining theory captures the most applicable physics describing the biomechanical solids and fluids in an aneurysm computational model to get better predictions. The modelling setup has to be as accurate as possible to ensure the results are successfully solved and the assumptions are made according to real solid and fluid parameters.

#### 3.3.1 Fluid Flow Equation

The solution applies flow equations that govern the aorta solid and fluid domain by considering three-dimensional incompressible fluid flow. Using the free surface and non-linear interaction assumption and Figure 3.3, the model is solved numerically by (i) mass continuity (Equation 3-4) and (ii) the equation of momentum (Equation 3-6) [129],

- i) The mass continuity equation in differential form is:

$$\frac{\partial \rho}{\partial t} + \nabla \cdot (\rho \vec{v}) = 0 \quad (3-4)$$

where  $\rho$  represents the density of the blood,  $\frac{\partial \rho}{\partial t}$  represents incompressibility and unsteady blood flow and  $\nabla$  is the divergence of the flow velocity vector field  $\vec{v}$ . The blood is assumed to be

incompressible with constant density and complies with the mass continuity equation and as a result, the velocity field is diverged at any location due to its non-dilation rate [130].

For symmetrical modelling in polar coordinates (see Figure 3.3), the mass continuity equation may be written as

$$\frac{\partial \rho}{\partial t} + \frac{\partial}{\partial x}(\rho \overline{v_x}) + \frac{\partial}{\partial r}(\rho \overline{v_r}) + \frac{\rho \overline{v_r}}{r} = 0 \quad (3-5)$$

Where  $x$  = the axial coordinator equivalent,  $r$  = the radial coordinate,  $\overline{v_x}$  and  $\overline{v_r}$  are the axial and radial velocity vector, respectively. Both  $\frac{\partial}{\partial x}(\rho \overline{v_x})$  and  $\frac{\partial}{\partial r}(\rho \overline{v_r})$  represent the velocity vector on the  $x$ - axis and  $r$ -axis in Figure 3.3. This figure illustrates the blood flow direction as imposed on the artery wall.

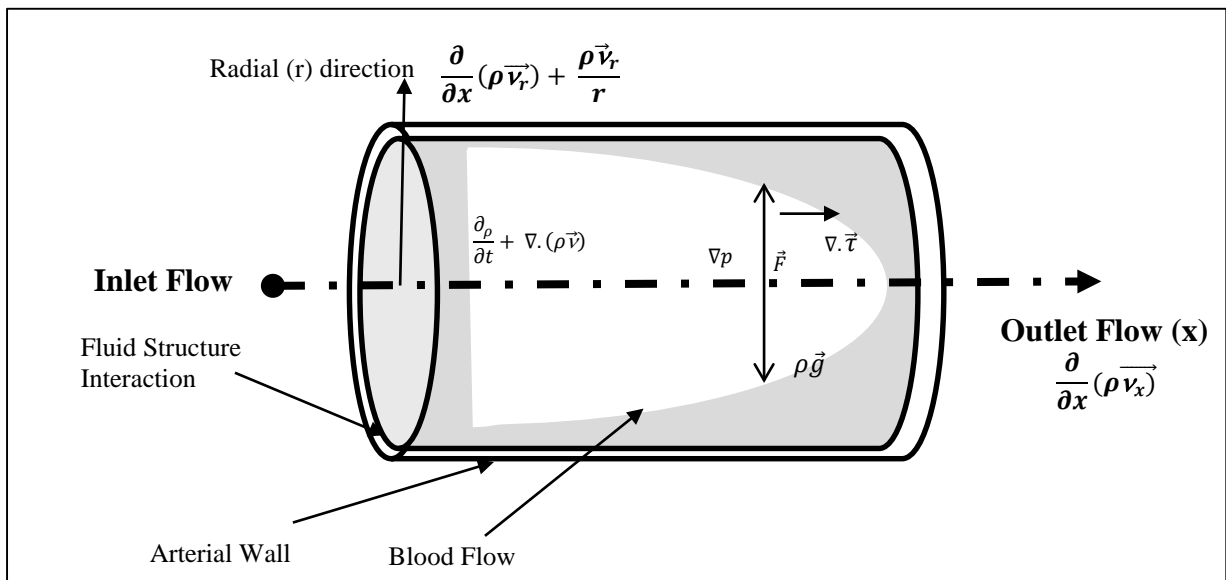


Figure 3. 3: The initial cylinder input and output for blood and arterial wall

ii) The conservation of momentum equation is applied to Figure 3.3

$$\frac{\partial}{\partial t}(\rho \vec{v}) + \nabla \cdot (\rho \vec{v} \vec{v}) = -\nabla p + \nabla \cdot \vec{\tau} + \rho \vec{g} + \vec{F} \quad (3-6)$$

Where  $p$  is the static pressure and the term  $\nabla p$  represents the divergence of the pressure,  $\vec{\tau}$  is the stress tensor and the terms  $\rho \vec{g}$  and  $\vec{F}$  represent the gravitational body force and external body force, respectively [130]. The divergence of the stress tensor represented in terms of  $\nabla \cdot \vec{\tau}$  in Figure 3.3 is written as:

$$\vec{\tau} = \mu \left[ (\nabla \vec{v} + \nabla \vec{v}^T) - \frac{2}{3} \nabla \cdot \vec{v} I \right] \quad (3-7)$$

Where  $\mu$  is the molecular viscoelasticity,  $\left[ (\nabla \vec{v} + \nabla \vec{v}^T) - \frac{2}{3} \nabla \cdot \vec{v} I \right]$  is the effect of the volume increment and  $I$  is unit tensor.

The viscosity equation ( $\tau_{ij}$ ) is used to govern fluid force investigations based on an incompressible and Newtonian fluid which is proportional to the rate of the deformation tensor  $\left( \frac{\partial u_j}{\partial x_i} + \frac{\partial u_i}{\partial x_j} \right)$  and is written as:

$$\tau_{ij} = \mu \left( \frac{\partial u_j}{\partial x_i} + \frac{\partial u_i}{\partial x_j} \right) \quad (3-8)$$

Where  $\mu$  represents the independent viscosity from the rate of the deformation, and  $i$  and  $j$  are tensor vectors.

### 3.3.2 Wall Equation

For geometrical modelling the tissue mass continuity equation is written as

$$\rho_w \frac{\partial^2 \varepsilon_{ij}}{\partial t^2} = \frac{\partial \sigma_{ij}}{\partial x_j} + \rho_w F_i \quad (3-9)$$

For  $i= 1, 2, 3$

Where  $\varepsilon_{ij}$  and  $\sigma_{ij}$  are the components of the strain and the stress tensor in a solid, respectively,  $\rho_w$  is the arterial density and  $F_i$  are the components of the body force acting on the solid. In this equation, the stress tensor  $\sigma_{ij}$  is governed from the conservative energy from the blood flow when deforming the blood wall. The stored energy is called the strain energy density function  $W$  and written as;

$$S_{ij} = \frac{\partial W}{\partial \varepsilon_{ij}} \quad (3-10)$$

$i, j = 1, 2, 3$

where  $S_{ij}$  and  $\varepsilon_{ij}$  represent the second Piola-Kirchhoff stress tensor and the Green-Lagrange strain tensor, respectively. The infinitesimal deformation conditions and the stresses are similar, thus the second Piola-Kirchhoff stress tensor is related to the Cauchy stress and total stress tensor as follows [129];

$$\tau_{ij} = p' \bar{l}' + \sigma_{ij} \quad (3-11)$$

Where  $\tau_{ij}$  and  $\bar{l}'$  represent the total stress and unit tensors for solid, respectively. However,  $p'$  represents the hydrostatic pressure.

### 3.3.3 Fluid Structure Interaction (FSI)

A coupling of biomechanics between solid and fluid is translated into the FSI technique which is feasible in merging a constitutive model with stress distribution and blood flow analysis [131, 132]. This technique is deliberately applied in the model to simulate a transient hemodynamics of the solid and fluid coupled in aneurysm that requires optimal solution. This couple interaction feasibly provides a complete solution of vessel wall and fluid region to understand the wall deformation and its progress in mechanical properties.

### 3.3.4 Two-Way FSI

The two-way effect between blood flow and solid wall interactions are simultaneously investigated using the two-way FSI method. In ANSYS, the solid and fluid equations were solved separately before generating the FSI interface on the model [129]. The solid is solved via solid element (mechanical) method and the fluid is solved via the Command Field Exercise (CFX) method. Then the results are exported to the mechanical method to generate the two-way FSI solution. Using FSI, the results are obtained according to the imposed fluid pressure with velocity across the FSI designated surface in the model. The CFX solves the pair of algebraic multi-grid equations to give vigorous results according to a complex flow field as expressed below:

$$\frac{d}{dt} \int_{(t)} \rho d = \int_v \frac{\partial \rho}{\partial t} dv + \int_s \rho W_j dn_j \quad (3-12)$$

Where  $v$  is volume integration,  $s$  is surface integration,  $dn_j$  is the differential Cartesian components of the surface vector and  $W_j$  is the velocity of the control volume boundary.

### 3.4 Material Assumption and Solution Method

In structuring the aneurysm model, it is important to know the physical geometries, necessary assumptions and the selection criterion in order to develop the particular realistic vessel shape to convey the blood flow.

#### 3.4.1 Wall Assumptions

A numerical analysis allows the pressure in the wall to react when the initial configuration of the artery model is setup. The wall properties of the blood vessels are curve fitted based on our experimental data from real specimens testing [124]. An estimated tissue tangential modulus and Poisson ratio of the model were used after considering stress strain data observed from testing. Mechanically, the modulus at the location of the disease stretches to a higher value compared to a normal artery [23]. Thus, the blood vessel wall stress and strain from the simulation results will be investigated for further analysis. Using material parameters (constants) in designing material properties is one of the approaches in the transitional trend between compression and shear deformation in ANSYS which is applicable to our reconstructed aneurysm model. This model constant can approximate the stress versus strain curve for elastomeric material including a rubber-like tissue specimen. This consideration is taken because the reconstructed aneurysm model exists in an elastic potential function  $W_{fr}$  (strain energy of failure) in Equation 3.3 which is a scalar function of one of the strains or deformation tensor. The constant model may be assumed according to the hyperelastic material model equation for the strain energy function as below:

$$w = \alpha(I_B - 3) + \beta(I_B - 3)^2 \quad (3-13)$$

Where  $W$  is the strain-energy density,  $B$  is the left Cauchy-Green tensor and  $I_B$  is the first invariant of  $B$ .

### 3.4.2 Blood Flow Assumptions

The basic formation of blood is known as red blood flow, white and platelets which are suspended in plasma. The viscosity that was obtained from this formation leads to physiologically changes where it allows the blood layers to slide over one another in smooth layer paths through laminar flow. In an unhealthy blood vessel, however, there is more interference between the layers due to different characteristics after blood flow is no longer laminar. An assumption of turbulent flow showed better agreement with clinical data with respect to the velocity profile in diseased arteries [133-135]. The transition from laminar to turbulence of the flows in arterial disease, is relied on low Reynolds number (Re) [136, 137]. Blood material properties, as well as the vessel wall property, values are taken from previous studies done by Yahya, Nichols and Canic et al. [137-139]. The summary of the blood and vessel wall parameters are detailed in Table 3.1.

Table 3. 1: The material parameter and boundary condition of aneurysm vessel wall and blood [137, 139, 140]

	<b>Characteristic</b>	<b>Material Properties</b>
<b>Tissue Wall</b>	Material Model	Hyperelastic Neo-Hookean
	Initial Shear Modulus, $G$ (Mpa)	0.075
	Initial Bulk Modulus, $K$ (Mpa)	1.5
	Young's Modulus, $E$ (Mpa)	0.25
	Wall Density, $\rho_w$ (Kg/m <sup>3</sup> )	960
	Poisson's Ratio, $\nu$	0.33
<b>Blood</b>	Fluid Density, $\rho_F$ (kg/m <sup>3</sup> )	1050
	Dynamics Viscosity, $\mu_F$ (kg/ms)	$3.5 \times 10^{-3}$

### 3.4.3 FSI Coupling Solver

Arbitrary Lagrangian-Eulerian (ALE) formulation is engaged in ANSYS to simulate the model using the FSI method. Using a high deformation capability to allow aspect ratio of the order of 10,000:1), it provides an enormously vigorous model and helps to increase the mesh morphing algorithm to handle the moving fluid domain. In the Lagrangian formulation where it is typically used for solid, a fixed volume is observed as particles move through it. Meanwhile, the Eulerian formulation is typically used for the fluid to formulate the domain comprising boundaries.

Through ALE, a hybrid formulation method has been incorporated [141], where in, the Eulerian formulation is used at fixed boundaries, the Lagrangian formulation is used at moving boundaries and the ALE formulation is used at fluid-structure interface. In governing the equation of ALE formulation, the actual fluid velocity with respect to a fixed mesh is replaced by a relative velocity which relates the actual fluid velocity to the mesh velocity [142]. In blood flow estimation, a certain velocity distribution, e.g., a Poiseuille or Womersley profile is assumed, and the flow is calculated based on the maximum or centerline velocity [143].

### 3.5: Tissue Failure Characteristic in Modelling

Tissue modelling yields useful information that will lead to further understanding of the relative reason of wall rupture. However, more comprehensive and reliable information can be obtained if the computational and numerical model parameters such as stress, strain and energy are well understood.

Since the final outputs generated from the computational modelling, as presented in Figure 3.4 are obtained from the equation solved by the software package ANSYS 15, here we discuss how the abovementioned parameter theory is generated. This information will be elaborated on in Chapter 5 and 6 to correlate with wall rupture prediction. In this modelling the basic relationship between pressure and blood flow is dependent on the material property selection of vessel wall and blood flow properties of the fluid. The FSI function bridges both solid and fluid to solve the stress distribution, straining effects of the wall as well as strain energy required from the fluid to deform the vessel wall. The continuation load from the fluid creates an input to recalculate the solid domain again and this process is repeated iteratively until balance and convergence is achieved.

Since the goal is to develop the aneurysm model using the FSI method, the results from the model are analysed and validated for rupture prediction. Referring to the three main elements of the data analysis study which consists of the geometrical analysis, numerical analysis and the combination of these two with the validation process, we hypothesize that the rupture of the aneurysm tissue can be calculated based on the strain energy function based on the heart rate. Data analysis involves three steps that from our hypothetical view to calculate the energy rate for rupture estimation for aneurysm model. The steps below need to be done in sequence for calculating the specimen strain energy and later to calculate estimation factors and time periods for ruptures.

- (i) Determining the strain energy to rupture (from the pressure imposed testing), is based on cyclic loading for each specimen – where the specimen rupture energy is calculated based on the time of the rupture. The total time

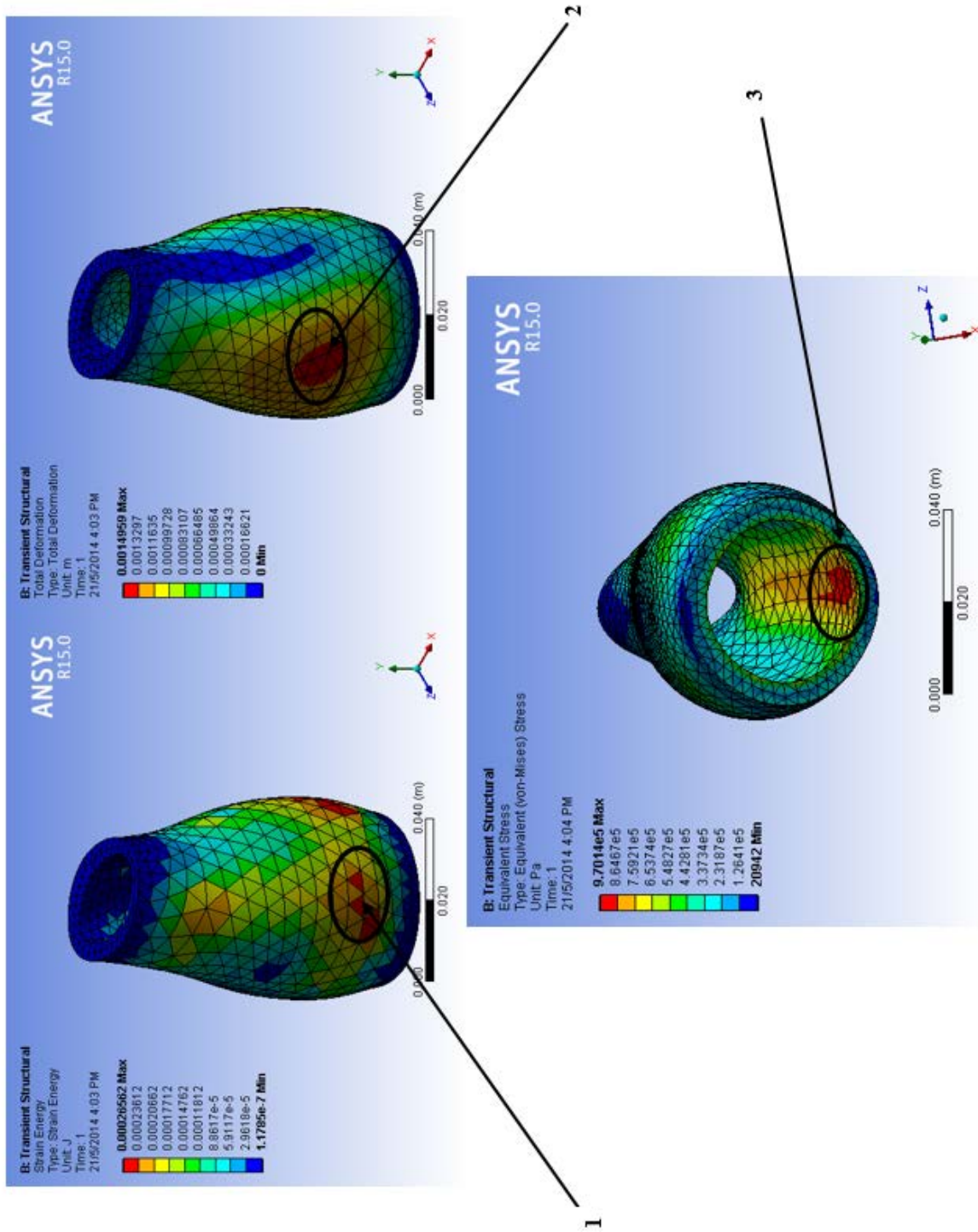


Figure 3. 4: Modelling Result from Aneurysm model with three observed parameters; strain energy (1), strain deformation (2) and stresses (3)

of the tissue to rupture is observed and is calculated based on total strain energy (Equation 3-4)

- (i) Determining the section of maximum strain energy per heart rate – A generated result from CFD aneurysm modelling simulation using a PSAM model is presented in Chapter 3. Based on the results, the maximum strain energy points were observed.
- (ii) From these two steps we can get an approximate heart rate linked to rupture by dividing the energy from step (ii) by the energy rate from step (i). These critical points of hypothesis will be further discussed in Chapter 7.

To express the result, the stress and strain of the measured tissue values were calculated in the sense of its behaviour, applicability and accuracy of the output requirement and includes the use of the data to compute the estimated energy consumption based on tissue deformation in the specimen testing that rely on the heart beat estimation.

### 3.6: Closure

Although rupture is determined by comparing the wall hoop and longitudinal stresses and strength, the exact wall strength measurement is impossible *in vivo*. As a result, considering only wall stress at a certain point may not necessarily provide a good estimation of the risk of rupture and it is important to acknowledge the strength at that specific time period. In this CFD modelling, our attention is directed more on FSI simulations of AAA rupture to identify if the rupture location coincides with the maximum stress of the aneurismal wall. This methodology

is expected to help clinicians in reaching a conclusion to determine the risk of AAA rupture and to better recognize the immediate need for surgical intervention.

The CFD/FE models of patient –specific aneurysms were used to simulate a strain energy progress on arterial wall aneurysm. Thirteen patients with three to four consecutive years of aneurysm progress history are developed to analyse the early periods of aneurysm enlargement. The variation of the thickness and diameter were investigated and observed as part of the indicator elements. The findings of the simulated models will be correlated and discussed further in Chapter 7 to elaborate on how the correlation between aneurysm wall progress and maximum wall strength is established based on ruptured specimen testing. This correlation will be used as non-invasive AAA assessment particularly on rupture diagnostic study. Furthermore, calculating the maximum wall strength of the tissue is the main principle of determination assisted by the contribution of the material characterization during the development of 3D modelling of aneurysms. This includes different geometry, pressure and wall thicknesses. By defining appropriate geometry, the mechanical properties can be used to generate the model from stress distribution and strain deformation in predicting the dilated affected aorta [24, 46, 73, 144, 145].

The following chapter will discuss the geometry of real aneurysm patients and all of their measurements used to reconstruct the aneurysm model.

## CHAPTER 4: AAA PATIENT DATA COLLECTION

### 4.1: Introduction

Medical imaging modalities have gained importance as assessment techniques for cardiovascular disease. There are several techniques and methodologies that have been developed to characterize patient-specific aneurysm geometry *in vivo*. According to clinical practice [146, 147], a diagnosed patient with preliminarily aneurysms needs to be observed throughout US or CT scans to assess the size and location for planning. However, in many instances, clinical examinations have shown inaccurate aneurysm size and location while assessing AAA due to unreal time observation or multi direction deformation.

In the situation where a patient has AAA problems, clinicians are not always decisive between the risks of not doing anything versus the risk of intervention or operation. Currently, for aneurysm repair there are two methods: Open repair, which has approximately 3% mortality [19] and Endoluminal repair which has 1% [50]. By assessing the risk of the aneurysm rupture from observation, it may justify whether any operation on the patient is necessary or not. The annual rate of rupture for AAA is difficult to quantify. Trials in 1980s and 1990s investigated the relevance of aneurysm risks. The UK Small Aneurysm Trial (UKSAT) and the Aneurysm Detection and Management (ADAM) screening program/trials [39] were the most reliable investigations to become biomarkers of aneurysm assessment. According to their findings, for the diameter 55 – 60 mm of AAA, the risk of rupture per year is about 6-11%. This indicator initially helps clinicians to identify the patient with high risk to rupture, that need to be offered immediate treatment and those that may wait longer who are at low risk. The benefit will apply to both patients i.e. only having operation if necessary and hence reducing unnecessary risks.

This research focuses on using US AAA data for understanding AA characteristics, prediction and analysis. This chapter presents the processes undertaken by this research to obtain data according to the geometry using segmented US AAA data. The proposed technique using P-SARP protocol is presented in Section 4.2 and analysed in Section 4.3. The 3-D PSAM models are reconstructed using available parameters from US image in this section before the structural analysis which is made in Section 4.3 and 4.4. All required information such as instantaneous dimension, thickness, pulse wave velocity and estimated central blood pressure are measured and classified accordingly. This new measurement method helps in proposing an alternative study using existing ultrasound screening assessment instead of other radiation-exposed imaging techniques for determining an earlier risk of rupture for any patient who had an aneurysm diameter more than 4.0 cm. Using US images along with new measurements and analysis techniques, stratifies patients into a high or low risk of rupture.

#### 4.2: AAA Patient Data Collection

Thirteen consenting outpatients (as illustrated by Patient Demographic in Table 4.1) undergoing US AAA for regular visits at the Manukau Super Clinic, New Zealand provided their aneurysm geometry and deformation progress along with information on other variables for later use. Following the proposed standard procedure of P-SARP protocol where the images were segmented in 2 cm slices from renal arteries to bifurcation, through to outer skin using US (See P-SARP procedure in next Section 4.3). Anonymous patient data is expected to provide the exact deformation of various parts of the aorta as a function of time, which is to be collected. This includes using the visual recorder available in US machine or images captured from the US scan. A General Electric (GE) US machine was used, with the software version release 3.1.2, equipped with curvy probe linear (C1-5) and 9L (Linear) which allow to screen until deep tissues. The data was obtained through their normal clinical assessment in

accordance with the proposed protocol on an aneurysm patient by a vascular nurse under the supervision of a vascular surgeon.

Patients were assessed voluntarily according to ethical approval obtained by Manukau Super Clinic and their consent. These findings may help to reduce the risks and costs associated with an early elective surgical repair by predicting patients that are stable as well as indicating which patients are at higher risk of rupture and need to be operated earlier.

Table 4. 1: Demographic of the observed AAA patient

<b>Patients Summary</b>						
	<b>Ages</b>	<b>Sex</b>	<b>Height</b>	<b>Weight</b>	<b>Max Diameter</b>	<b>BMI</b>
<b>Patient1</b>	79	F	159.5	61.8	4.52	24.29
<b>Patient2</b>	77	M	170	72.5	5.74	25.09
<b>Patient3</b>	61	M	163	59.7	4.56	22.47
<b>Patient4</b>	85	M	182	83.7	4.96	25.27
<b>Patient5</b>	82	F	166	77.7	4.6	28.20
<b>Patient6</b>	74	M	176	81	5.57	26.15
<b>Patient7</b>	75	M	167	71.4	4.23	25.60
<b>Patient8</b>	66	M	182	74	5.87	22.34
<b>Patient9</b>	75	F	162	64.5	4.06	24.58
<b>Patient10</b>	92	M	163	57	5.24	21.45
<b>Patient11</b>	72	M	184	80	5.02	23.63
<b>Patient12</b>	77	M	180	77	5.17	23.77
<b>Patient13</b>	82	F	148	51	8.33	23.28
<b>Mean Value</b>	77	Mean Value	167	72.5	5.02	24.29

#### 4.2.1: Patient Database

Patients with known aneurysms measuring over 4.0 cm were invited to participate in this study. Priority was given to patients with aneurysms over 4.0 cm in diameter. However, if more patients participate, the criteria put in place for the blood pressure record, diagnosis date and ethnicity will limit the numbers. Based on the list of the patients provided from CMDHB, the primary researcher invited potential participant through an information sheet at the end of their clinic appointment. The participants were asked to sign a consent to participate.

#### 4.2.2: Ethics Approval

Following human ethics approved by the Auckland University of Technology Ethics Committee (AUTEK) number 12/273 and CMDHB number 1404, 13 patients were recruited for data collection (see Appendix A). Subjects were selected based on proposed criterion by CMDHB and the specification agreed by the researcher through the P-SARP protocol. Patient data was taken after the assessment protocols provided were consented for the study. See Appendix E.

#### 4.2.3: Consent

Patients were given a random number which was recorded in the database to ensure the confidentiality of the collected data. All the data was recorded on the consent form, which can only be accessed by the researchers and project supervisor for administrative purposes. Only anonymous data was available to the individual researchers.

#### 4.2.4: Data Storage

The anonymous data collected from this project can be accessed with other existing clinical patient records that relate to aneurysm at IBTec. The database is securely stored within IBTec, where access to it was controlled uniquely by the Director of IBTec and related researchers. In the hospital, the data was stored using the Agfa RIS System, which is capable of recording patient's aneurysm data for the next 10 years.

#### 4.3: P-SARP Protocol using US

The entire aneurysm measurement process follows a standard protocol as is normally followed in a clinical diagnostics laboratory. The only difference is that there was more time taken as we needed to observe the images in more detail in every segmented ultrasound. The recorded data is archived and securely stored till 1 January 2023 in agreement with hospital. The new recorded data is used for therapeutic treatment in the future. This protocol is based mainly on

specific data collected from the same patient at an instance in time. This approach is expected to assist clinicians in reaching informed decisions to determine the risk of AAA rupture and to better recognize the immediate need for surgical intervention. Since there is an increasing issue in developing countries with an aging population with multiple comorbidities and AAA, the model is initiated to propose better patient selection for AAA repair, which consumes a large amount of health resources per patient. Since this research expects to lead to new strategies to investigate and predict the risk of abdominal aortic aneurysm rupture at an early-stage, it has the potential to contribute to the field of aneurysm prognosis. It also provides a useful tool to clinicians to predict/rank the risk of aneurysm.

#### 4.3.1 P-SARP Protocol Procedure

The following protocol is used to determine the AAA dimensions and shapes:

- 1- A scale sticker is attached to the patient's stomach as guidance (Figure 4.1). The measurement at four important points (A to C and B to G) including the diameter from the vertical and horizontal axes are made to ensure image accuracy. An insonification angle at the maximum value is considered (60 degrees) for better image quality when applying the Doppler on the outer skin. The level of the sensitivity of the thickness factors is investigated to make best use of the images.



Figure 4. 1: Measuring with US Doppler with the proper insonification angle [148]

2- The aneurysm diameter and thickness is recorded from patient charts as assessed from the US device. The protocol is illustrated in Figure 4.2, where the spinal cord of the patient is located at point E during assessment. No bias to AAA patient selection will be made with respect to age or sex.

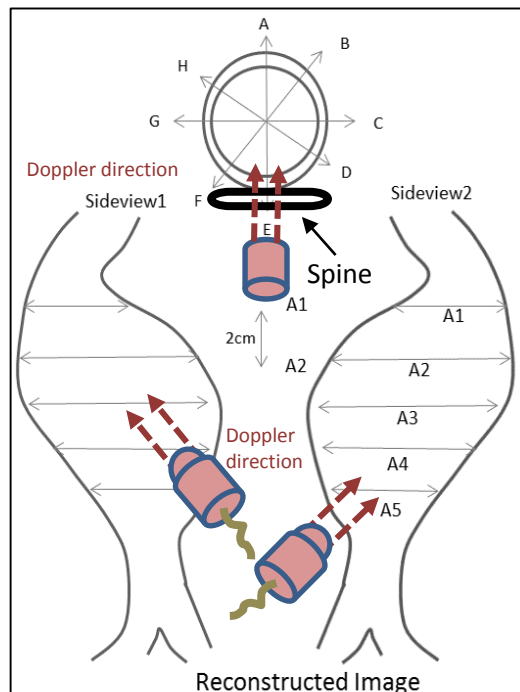


Figure 4. 2: Aneurysm assessment using P-SARP

- 3- Patient blood pressure is also measured using the Pulsecor Cardioscope II [149] that has been used at IBTec to measure the estimated arterial and central pressure from the patient as part of input modelling for subsequent numerical simulation.
- 4- The healthy (normal) data is taken from aorta above the renal artery since the most of the aneurysm cases start below the renal artery.
- 5- The slice thickness of the wall and the lumen of AAA is determined by the node thickness (A to E and C to G) in accordance with a 45° cross sectional area (CSA) pattern as well as the lumen boundary. See figure 4.3. All the segmentations are built up to separate the lumen and the wall along with the investigated artery area (from renal arteries to iliac bifurcation).

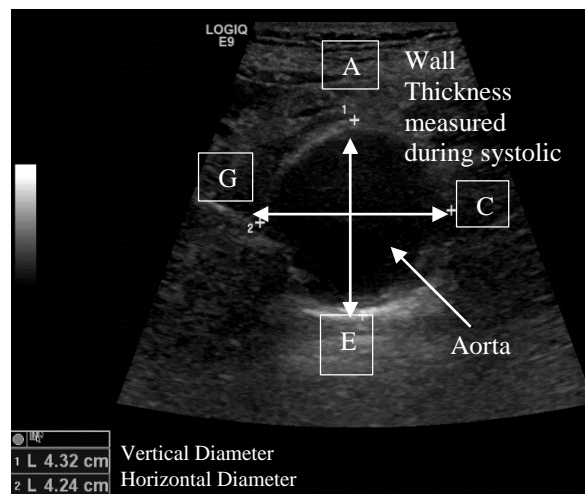


Figure 4. 3: Cross-sectional aorta from US for measurement

- 6- The patient-specific geometry details are recorded in the Abdominal Ultrasound images segmentation (AUis) template as in Figure 4.4. This assessment template is completed by the vascular nurse specialist team to ensure that the measured image and aneurysm formation are appropriately observed in standard format.

**Aneurysm Ultrasound image segmentation (AUis) Form**

Patient Code:  
Date/Time:

View 1 →      ← View 2

View1      View2

Estimation Aneurysm vertical snapshot images

Sg1

Sg2

Sg3

Sg4

Sg5

Sg6

Sg7

Sg8

Sg9

Circumferential snapshot (All measurements in cm)

Measured by:

Figure 4. 4: Abdominal Ultrasound images segmentation (AUis) template

- 7- The patient-specific snapshot image of pulse wave velocity (PWV) is also required from the biggest sac of the AAA to investigate the blood flow of the affected aneurysm sac. This PWV is used to regenerate a mathematical equation using the Fourier series function for the PSAM output model.

8- A reconstructed aneurysm model based on the US images are illustrated in Figure 4.5 by the following P-SARP protocol steps:

- a. Map the boundary of the aorta to distinguish between the lumen, aorta wall and thrombus (ILT) as shown in Figure 4.5a.
- b. Mark the points (A to E for vertical and C to G for horizontal) that are justified by the vascular nurse in the AUIs template according to the 2 cm range between segments as illustrated in Figure 4.5b.
- c. All the images are then migrated into three dimensional modelling to create geometry of the model between the points using the spline line feature.
- d. Stack each segment in two different side views as illustrated from the AUIs template (task is done by the vascular nurse). See details in Figure 4.5c and the modelling reconstruction detail in Section 3.3.

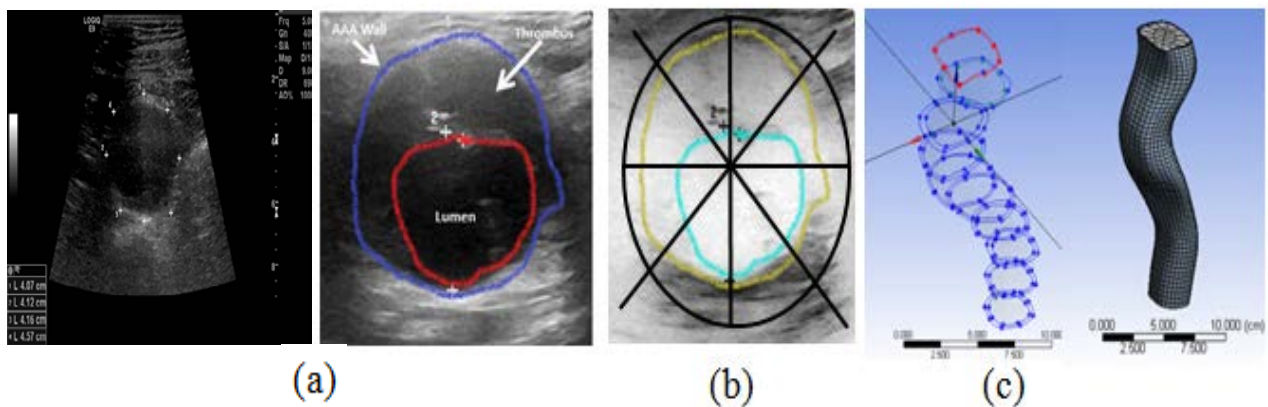


Figure 4. 5: (a) Measurement of the diameter in the US image (b) Measurement of the thickness with 45 degrees c) Image regeneration

#### 4.4: Ultrasound Accuracy and Visual Limitation

The ultrasound assessment is a standard screening process for aneurysm patients to get through regular clinic visits. The basic scanning procedure as explained in the P-SARP protocol within

ultrasound frames is cautiously supported by a suitable Doppler to produce the best images (see Figure 4.6). Well trained vascular nurses from Manukau Super Clinic, New Zealand were given the responsibility to assess the same patient using the proposed protocol under the supervision of a vascular surgeon.

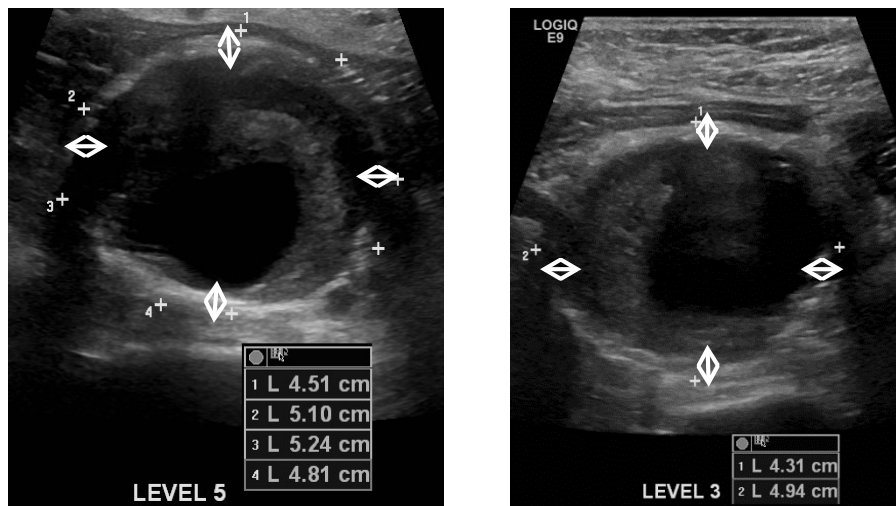


Figure 4. 6: Thickness measurement from Ultrasound imaging

The visuals based measurement might also have some minor inaccuracy when looking at systolic and diastolic pressure (small differences shown in figure 4.7). However, nurses' expertise in determining an accurate image helps to minimize a low quality image and unclear measurement.

Many researchers have used the signal of the US probe to obtain a quality image as a source of quasistatic mechanical excitation [11, 119, 147, 150]. In order to gain that quality, the outer skin of the assessed area needs to be gently pushed by the probe against the surface. An avoidance issue that could not be overcome was the presence of bowel gas from the patient. This gas existence restricts the nurses' view during assessment and aneurysm assessment could be postponed for hours or day.

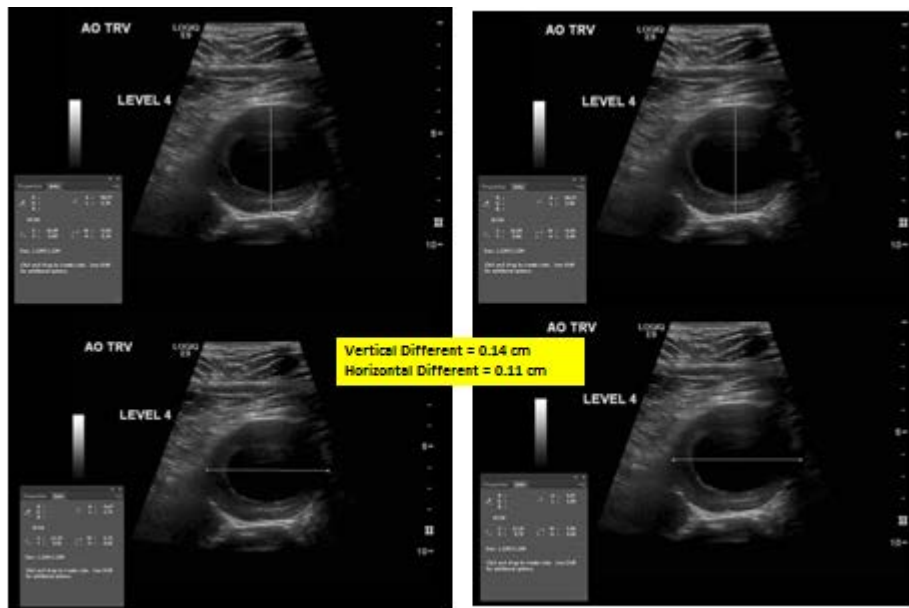


Figure 4. 7: Expansion measurement between systolic and diastolic pressure

#### 4.5: Closure

This chapter outlines the method used in collecting US data and how the data was analysed to obtain AA size (diameter, thickness and shape). This data was then processed to be used in the simulation process as explained in next chapter.

## CHAPTER 5: ANEURYSM SIMULATION AND ANALYSIS

### 5.1: Introduction

To start the numerical simulation process, accurate geometry and physical properties were obtained and were used as inputs to the simulation process. Chapter 4 presented the US data collected from the patients. This chapter presented the procedure and methods that were used to convert the data in Chapter 4 to values used in the simulation process. These values were then inserted in the ANSYS software to produce a realistic simulation of AAA. The final simulation models were analyzed and critical stress, strain and energy parameters were determined in magnitude and location.

### 5.2 US Structural Design and Geometrical Analysis

The images observed from US using the P-SARP protocol give two main structural parameters of the real aorta: the diameter and the thickness. In order to extract reliable geometries of aneurysm, the segments of interest from the image selection must take into consideration the influences on hemodynamic variables. The original aorta cross sectional shape in the human body is considered, as shown in Figure 5.1a. This point allocation process helps us in determining the physical factors of aorta deformation direction which will be discussed later in Chapter 7. For the diameter, vertical and horizontal orientations are observed from the image per segment which consists of four measured point (A-E for vertical) and (B – G for horizontal). These points were also used for instantaneous thickness measurement of the wall. Using the P-SARP protocol in which the scan was performed during normal breathing (systolic condition), all of these points were observed to ensure that the images follow the same standard to reduce motion artefacts. Figure 5.1b shows the location of the designated segment (A1 to A5) according to the P-SARP protocol discussed in Section 4.3.

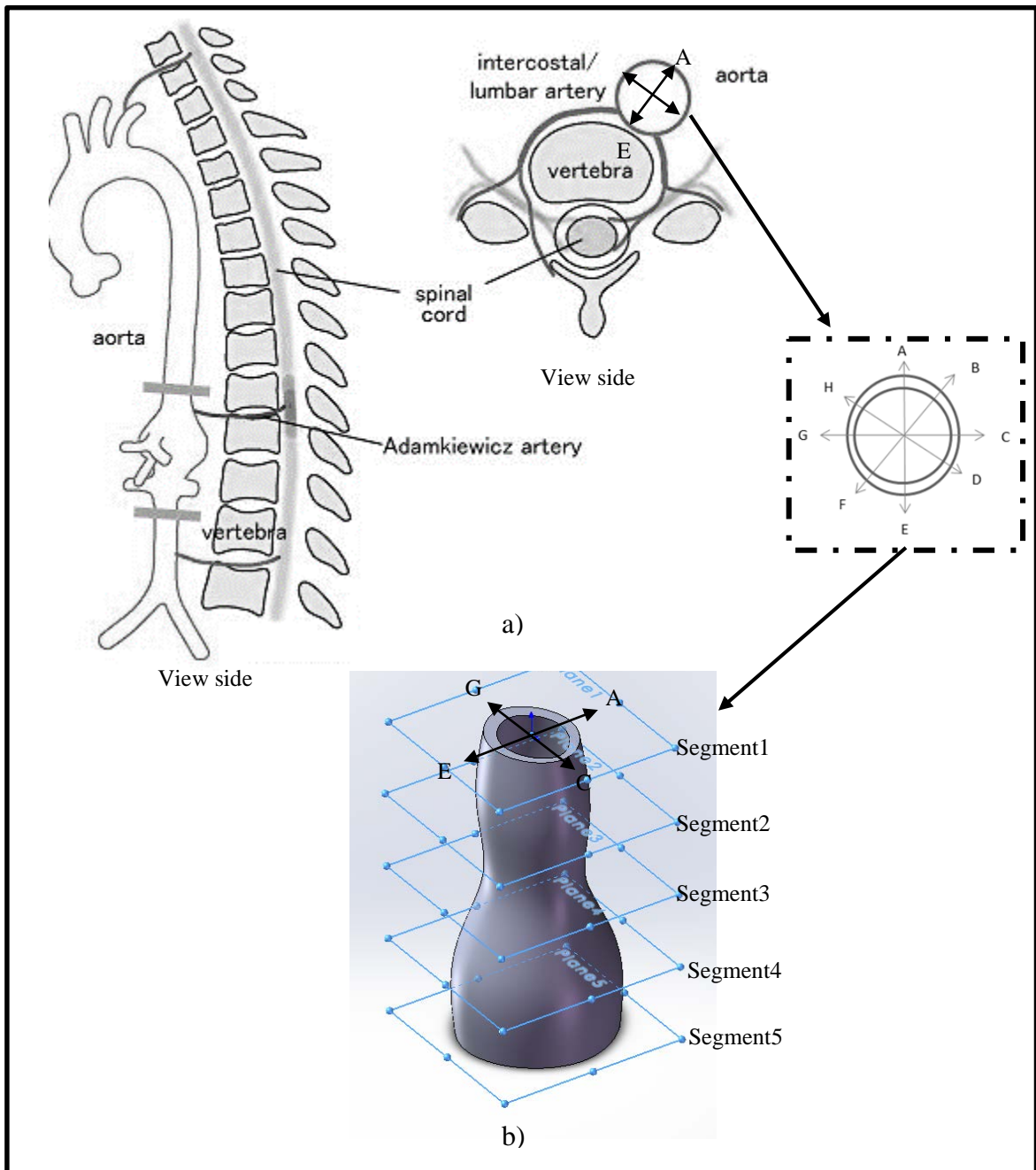


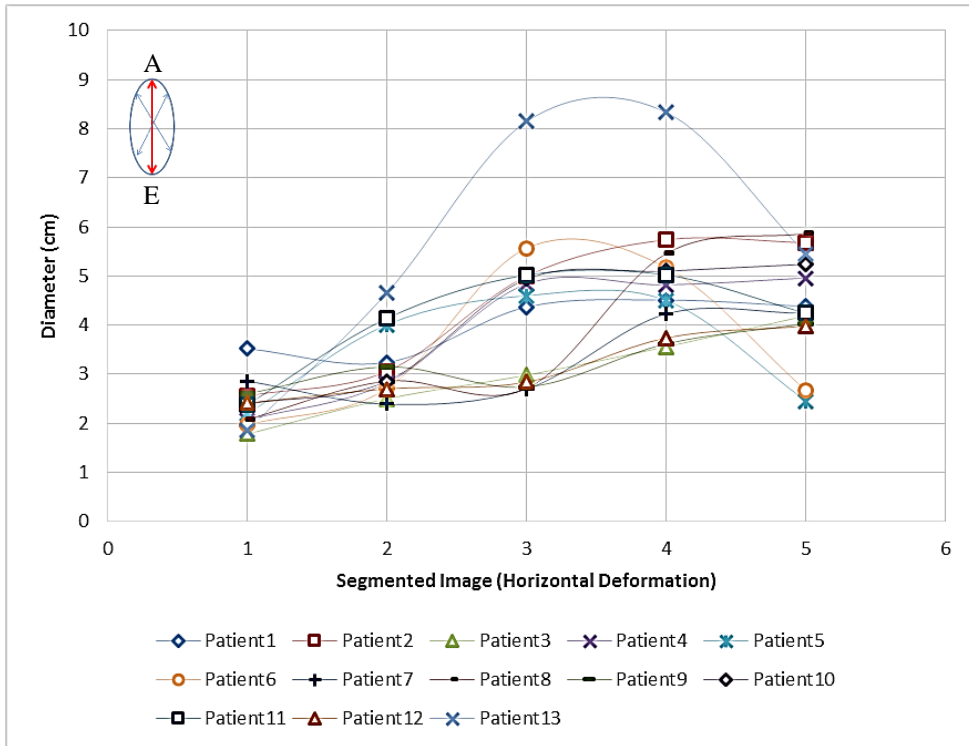
Figure 5. 1: a) Measurement points from aneurysm location in patient, b) Model location of the segment A1-A5 based on cross sectional points in accordance to P-SARP protocol. Image originally adapted from aortic dissection [151]

The segmented images were taken from two dimensional (2D) US image dimensions of 960 x 720 mm at a resolution of 1024 x 1024 and presented in Figure 5.2. This figure shows the measurement obtained from different segments and deformation axes with corresponding

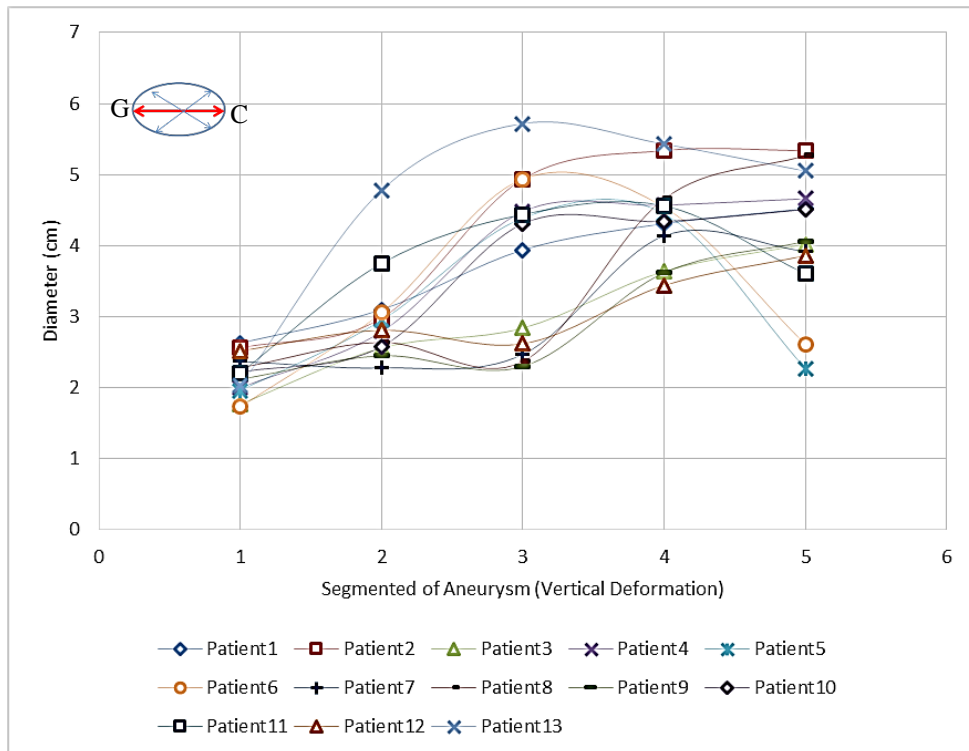
diameter. The thickness measurements were taken from the US images using Adobe Photoshop V 14.1.2 x64 (Adobe Systems Inc.) according to designated points from P-SARP protocol before further analysis.

### 5.2.1 Factors by Segment and Thickness

In this analysis, we look at the variation in thickness and diameter in order to determine the most suitable dimension and shape for the simulation process. The analysis is done on the most affected segmented areas during geometry measurement. The geometrical analysis from the vertical and horizontal segmentation on patient aneurysm images shows that segment 4 and 5 have consistent increments in diameter. Half of the segments' diameters increased at section 3 with an average value of aneurysm diameter (Figure 5.2). This value changes is used as the benchmark in Chapter 7. The thickness variation as measured from US provides the possible value that could be affected when simulated on the PSAM. These values were compared with the modelling results to identify the specific regions from different PSAM and is discussed in Section 5.4



(a)



(b)

Figure 5. 2: Aneurysm Deformation at each segment in (a) vertical and horizontal (b)

### 5.3 Modelling and Simulation

Simulation results from the aneurysm geometry using specific parameters provides a multi-mechanism parameter to be further investigated. The arterial wall is defined from measured geometry using the P-SARP protocol in Section 4.3 for a standardized measurement. Aneurysm models need to implement accurately the mechanical characteristics of the wall. Also the hemodynamics of the blood flow inside the vessel wall during pulsation flow needs to be understood. This leads us to observe the effective factors that may contribute towards aneurysm rupture possibilities. This information can be translated into a correlation with wall biomechanics factors and CFD modelling studies later in the chapter. The computational method consists of three main elements that make the model more accurately simulated as a realistic model. Each element is to be wisely characterized according to the preferred mechanism for analysing the computational procedure as shown in Figure 5.3.

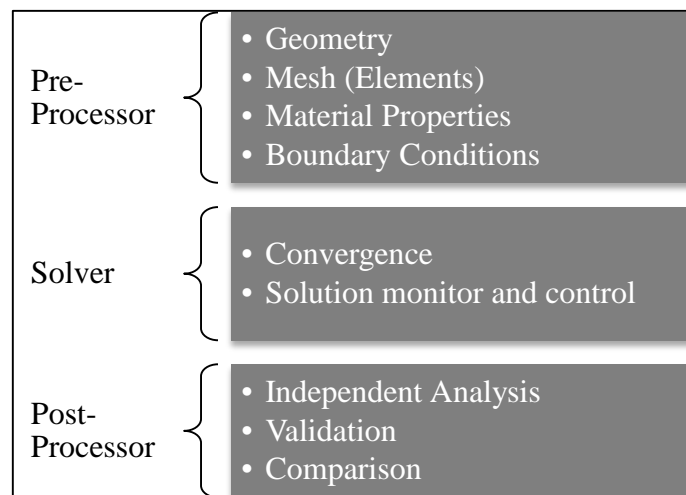


Figure 5. 3: Computational Method Stages

#### 5.3.1 Patient Specific Aneurysm Model (PSAM)

An image processing technique using US is shown in Figure 5.4. The snapshot geometry at each segment level is designed to include the diameter in the vertical and horizontal axis,

thickness at a specific location (referring to 45 degrees method under the P-SARP protocol in Section 4.2). The real design of arterial wall and blood flow estimation from the original image is time consuming and a challenging process in computational modelling due to several dynamic responses. However, by understanding the wall deformation due to the blood forces, the stress effect distribution in the vessel wall can be predicted. The coupling between solid and fluid is estimated according to real patient data from clinical assessment and aneurysm tissue specimen test findings.

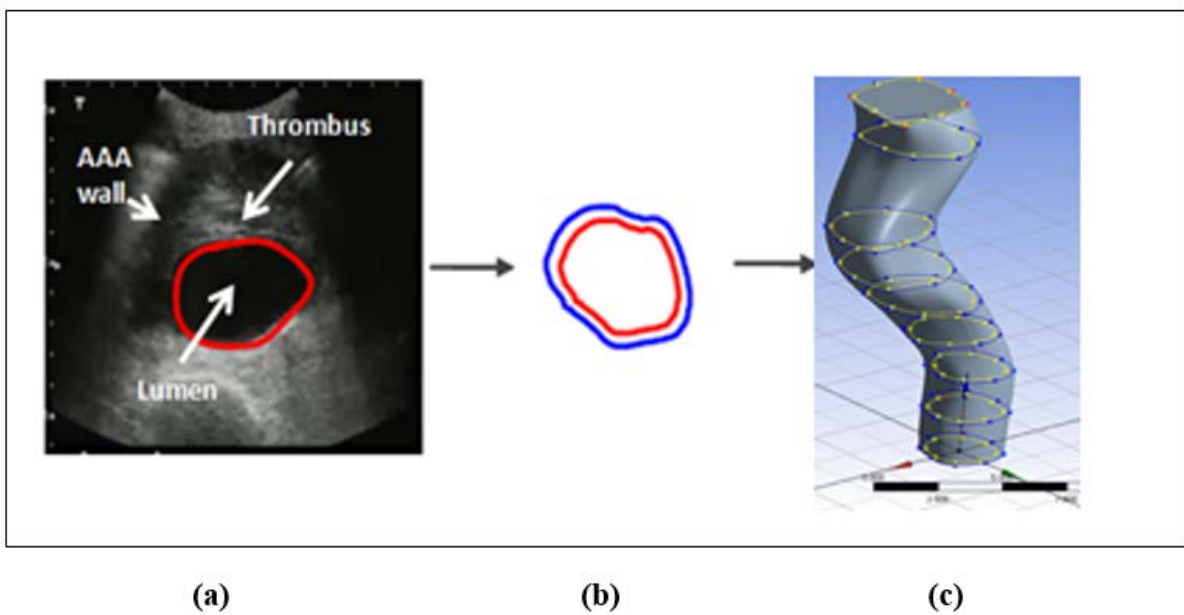


Figure 5. 4: Geometry snapshot capture to CFD Modelling using ANSYS; a) Ultrasound blood vessel morphology, b) Wall thickness creation and c) AAA blood vessel regeneration

### 5.3.2: Geometry Design

The model for each patient is designed separately due to different sizes of thickness in AAA as the thickness changes during the development of AAA. The detail of the design is summarized as follows:

1. Dividing each cross sectional area of a segment (to be modelled) by 2cm apart along with specific thickness in an attempt to improve the accuracy of the model [62].

2. After the construction, the model is meshed and the boundary conditions are placed in the modelling process. Since the behaviour of the individual region and element nodes are easy to distort after meshing processes, it is necessary to have the best quality of mesh in order to obtain a satisfying result. In order to measure mesh element quality, skewness of the mesh metrics measurement is used to measure the relative distortion of elements by comparing the element with its ideal shape.
3. This modelling process investigation starts with the transient mechanical analysis using a reconstructed idealised model as shown in Figure 5.5.
4. A simplified model as shown in Figure 5.6 is initially used to determine the dynamic response before proceeding to the complex models obtained from US images. This aneurysm model (PSAM) is reconstructed and is elaborated at the next section.

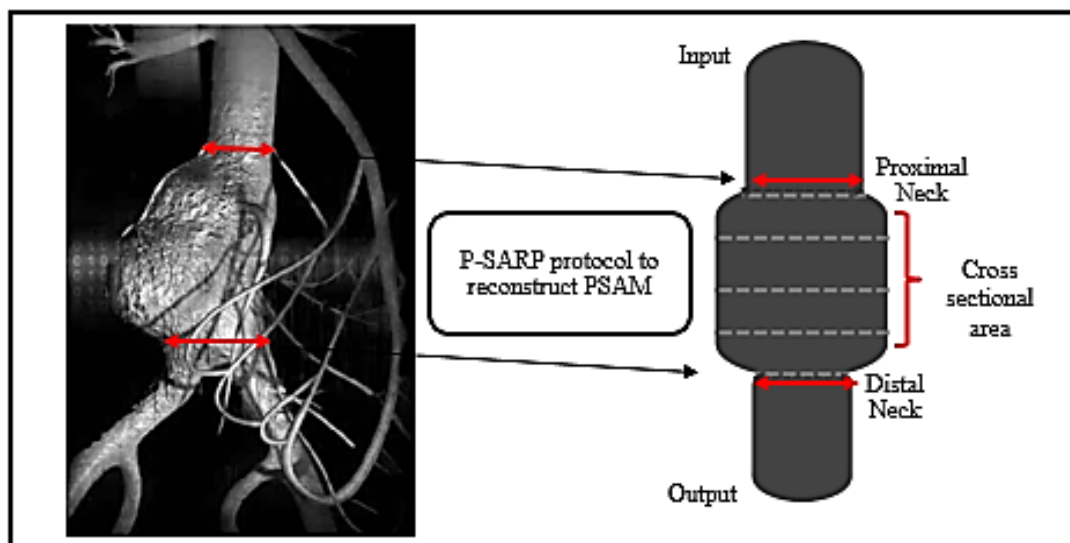


Figure 5. 5: Image segmentation and parametrical modelling for the Idealised Model before PSAM from real aneurysm images

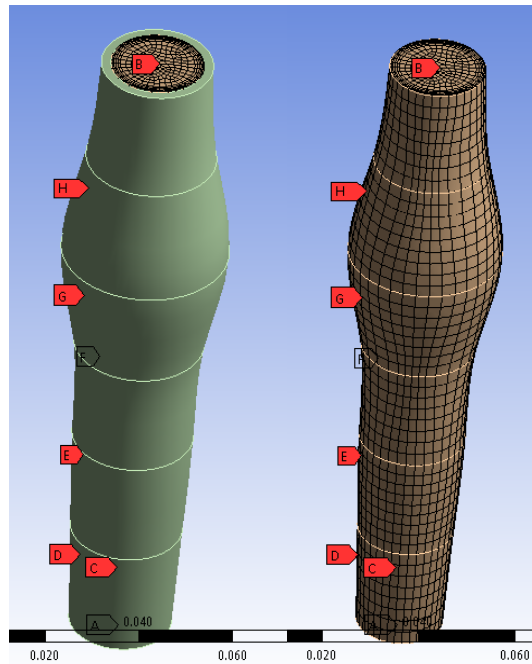


Figure 5. 6: Simplified model with boundary conditions for each segment

In order to keep the originality of a real patient geometry model, we simplify the model without changing any geometry information (Figure 5.7). Simplified models were generated based on US available parameters from patient specific geometry with 5-6 segmentations and four designated points (A to E and C to G). Details are discussed in Chapter 4 (P-SARP protocol). The results of these simplified models have influenced the investigation of the mechanism of cardiovascular disease development. Using the accurate data provided (described in Chapter 4), the PSAM development has resulted in a realistic model based on anatomical data from screening ultrasound assessment.



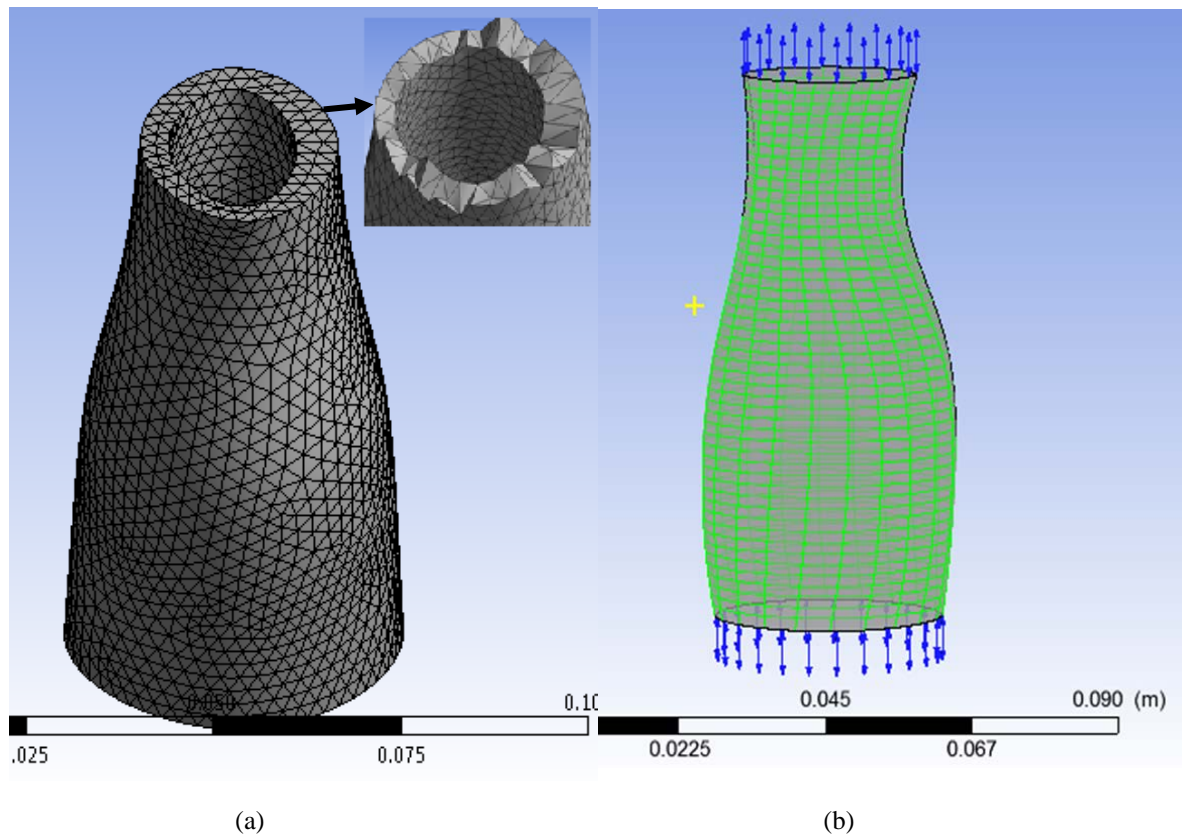


Figure 5. 8: Mesh generation for (a) simplified PSAM model and (b) boundary condition setup

The acceptable mesh as stated in Table 5.1 below has proven a good statistical measure for moving the mesh node. The convergences are assessed to remain in a satisfactory range [99, 103, 117, 132, 141]. For the number of converged iterations, the maximum value is performed based on the level of residual reduction or absolute residual level until an appropriate level of convergence is achieved. The solid wall and fluid blood needs to be meshed with different types of techniques to ensure it is suitable with the degree of complexity and the various options available in meshing methods in ANSYS which includes the sweep, tetrahedron and multizone features [152].

Table 5. 1: Measuring Mesh Elements (Mesh Metrics)

Mesh Metrics	0-0.25	0.25-0.5	0.5-0.8	0.8-0.95	0.95-0.98	0.98-1.00
Acceptance Level	Excellent	Very Good	Good	Acceptable	Bad	Unacceptable

#### 5.3.4: Boundary Conditions

In this research, an aneurysm model is numerically simulated using ANSYS 15.0<sup>®</sup> based on partial differential equations as described earlier in Chapter 4, particularly the equations in different domains (Equations 3-4 to 3-12). The boundary condition is set separately according to different domains.

- *For the solid domain* (Figure 5.9a), the body is assumed to be a flexible solid with radial displacement possibilities after both ends are fixed (zero displacement). The FSI face is set between the solid and the fluid domain. (See details of both properties in Table 3.1)
- *For the fluid domain* (Figure 5.9b), the fluid is assumed as an incompressible, Newtonian fluid of dynamic viscosity  $3.5 \times 10^{-3}$  and a density  $1050 \text{ kg/m}^3$ . The inlet and outlet of the fluid domains were fixed.

The input and output setup for this aneurysm model relies on actual patient blood pressure waveforms which were invasively measured in patients undergoing aneurysm assessment at the Vascular Surgery Department in the Manukau Super Clinic under ethics approval number 1404. The equation is governed by using a Fourier transform formulation based on a consistent waveform cycle from imaging data and this equation is used as the input and output as shown in Figure 5.10. The imported pressure from the input as shown in Figure 5.11 illustrates the high pressure response on the wall after a given pressure at the inlet. The output corresponds to blood pressure waves generated at a specific location from US imaging.

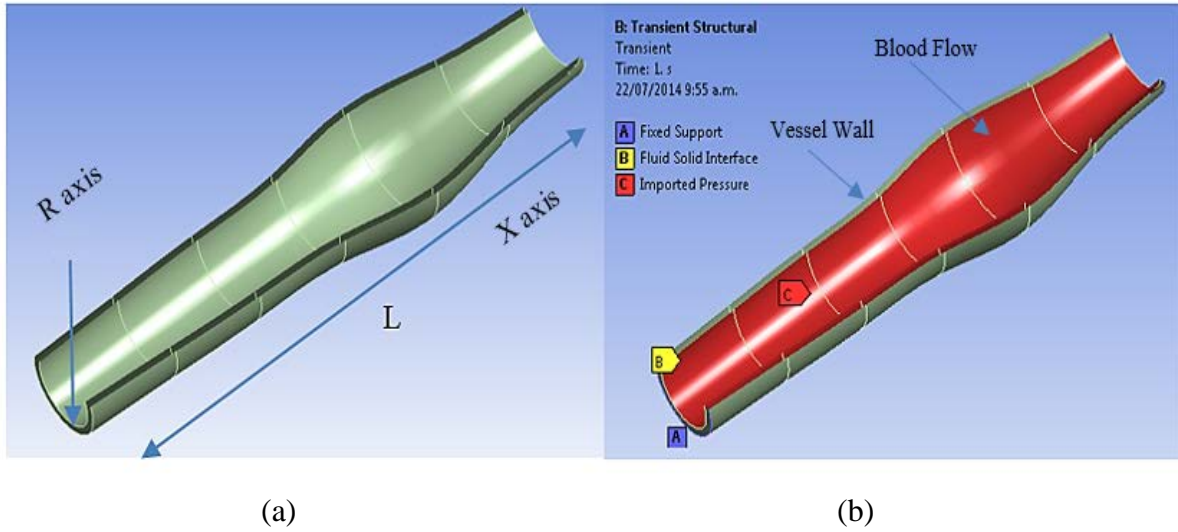


Figure 5.9: (a) Model designated axes (b) Boundary condition with: (A) Both ends of the artery are kept in a fixed position. (B) The inner surface of the fluid is set as FSI and (C) imported fluid pressure to the wall.

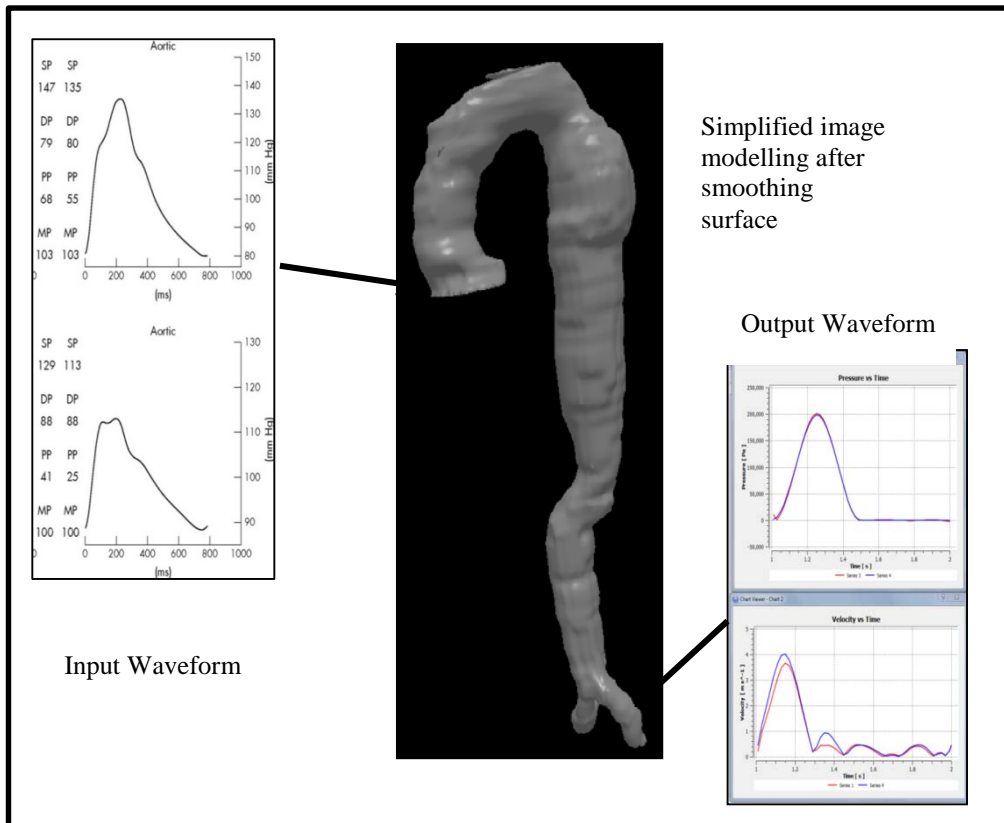


Figure 5. 10: Input and Output Modelling Setup

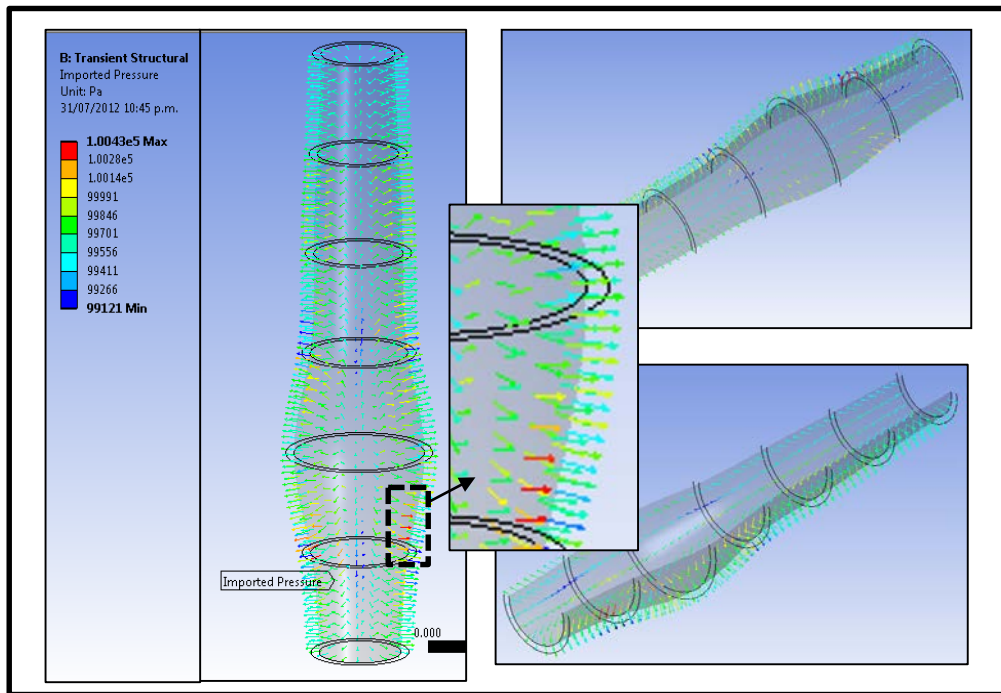


Figure 5. 11: Imported Pressure from PSAM model

### 5.3.5: Material Properties of the Model

The accuracy of the mathematical model relies (most importantly) on the hemodynamic effects during arterial deformation. This investigation has to consider hemodynamic factors. For example, the hemodynamics of biological tissues consider nonlinear, elastic properties and rely on historical data of stress-strain relationships that are expressed by exponential functions [132]. The stress strain history is determined by the quantity of pulsatile forces or pressure that causes deformation on the solid wall. In this research we assume that the tissue material properties are viscoelastic and hyperelastic according to stress-strain data obtained. In this research the arterial wall is assumed as a single layer throughout the whole reconstructed model as a Neo-Hookean elastic non-linear arterial material which is dependent on the stress-strain behaviour of macroscopic material deformation. The assumptions used in our modelling process consider realistic material properties with the Cauchy elastic wall ( $W$ ) expressed by:

$$w = \frac{G}{2}(\bar{I} - 3) \frac{k}{2} (J - 1)^2 \quad (5-1)$$

Where  $G$  and  $k$  are the shear and bulk modulus of the arterial wall, respectively,  $J$  represents the ratio of the deformed elastic volume over the undeformed volume and  $\bar{I}$  is the first invariant of the left Cauchy-Green deformation tensor [129]. Real specimen data from multiple testing methods were used to generate curve fitting in defining tissue behaviour for the aneurysm model. This curve fitting method is used to explore the mechanisms associated with the tissue stress-strain relation according to the blood pressure waveform. This will be explained furthermore in detail in Chapter 6 for analysing tissue specimen behaviour.

#### 5.3.6: Parameters Specification

Parameter specification for FSI settings are summarized as shown in Figure 5.12 and are used in the computation of the PSAM to generate model results. The results obtained from this model are to be investigated to determine the tissue failure mode discussed in Section 3.2. Three main elements; strain deformation, equivalent stress and strain energy are computed and are illustrated in Figure 5.13. The table 5.2 represents the maximum values of stress, strain energy and also deformation generated from the PSAM model.

These findings will be further discussed in Chapter 7 where the details as compared with other important elements which need to be considered as tissue wall failure contributor.

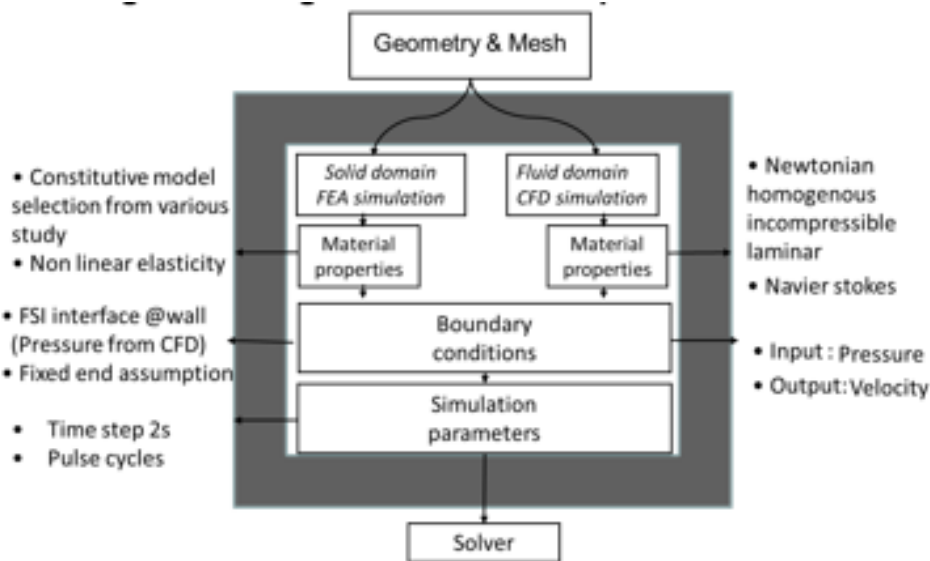


Figure 5. 12: Setup parameters in computational modelling

Table 5. 2: Stress, Strain Energy and Deformation Simulation Results

Model	Maximum Stress (MPa)	Minimum Stress (MPa)	Strain Energy (J)	Deformation (M)
<b>Patient 1</b>	0.097	0.002	0.00027	0.0015
<b>Patient 2</b>	0.097	0.008	0.00043	0.0018
<b>Patient 3</b>	0.077	0.041	0.00077	0.0074
<b>Patient 4</b>	0.11	0.007	0.00049	0.0023
<b>Patient 5</b>	0.094	0.0039	0.00041	0.0018
<b>Patient 6</b>	0.09	0.0013	0.00065	0.0098
<b>Patient 7</b>	0.116	0.0015	0.001	0.0017
<b>Patient 8</b>	0.075	0.002	0.00042	0.0012
<b>Patient 9</b>	0.084	0.0062	0.0018	0.0018
<b>Patient 10</b>	0.1	0.0076	0.0013	0.0017
<b>Patient 11</b>	0.77	0.0062	0.00083	0.0012

#### 5.4 Simulation Results

A simulation analysis was conducted at different stages to evaluate the difference between various couplings under a variety of parameters. The structural members subjected to strain deformation, stresses and energy from reconstructed geometry were analysed as shown in Figure 5.13. In order to determine a large variation of deflection, the formation of the geometry was varied based on primary element modelling such as material properties and model shape. Specific locations of the thickness and the diameter are also analysed according to marked points and segmented boundaries as specified in the reconstructed model. This simulation result

was executed for different patients to compare the possible variation of real aneurysm geometrical analysis and actual location from the patient's aorta. The selected parameters will be further analysed and compared in order to identify rupture characteristics in Chapter 6.

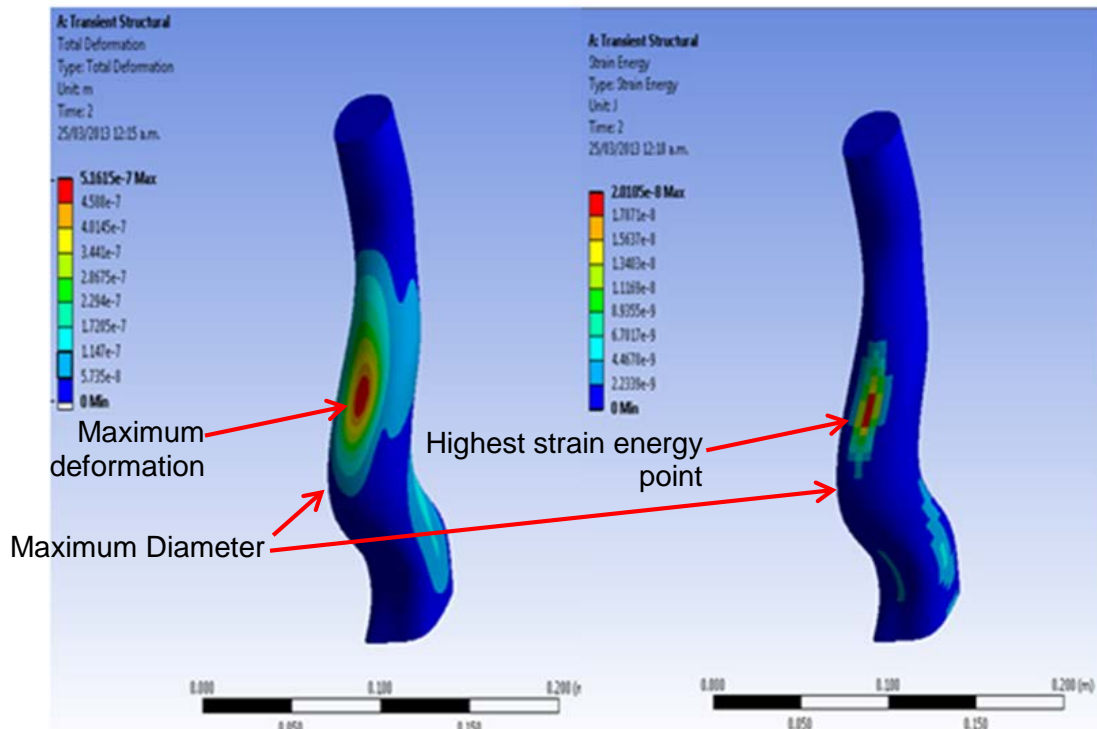


Figure 5. 13: Multi variation output parameters resulting from PSAM simulation

#### 5.4.1 High deformation region

Deformation in ANSYS is estimated from iterative displacement calculations. Based on that, the stress and strain were calculated as the normalized force applied by the inner surface to deform a cross section (segment) by using a membrane stress formulation [10]. In this observation, the section with the highest wall deformation due to the flow-structure interaction in an aneurysm is investigated. From these findings, the results provide better indication the affected area within aneurysm sacs. Its ability to see the exact location during the maximum

diameter in one pulse could clearly clarify that the defect region does not always occur at maximum areas.

By comparing the results with geometrical analysis from Section 5.2, it showed that the high deformation value location varies between segments (Sg) A3 to A5 in our modelling as illustrated in Figure 5.14. The thickness points also were parametrically observed to identify the deformation progress based on thickness. The rest of the PSAMs were observed according to point from the thickness and model segmentation as shown in Figures 5.15 and 5.16.

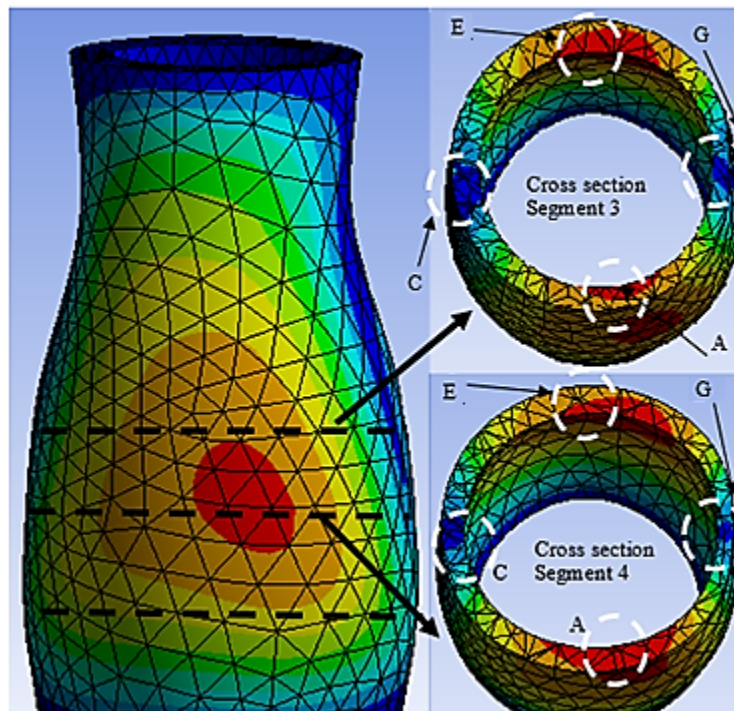


Figure 5. 14: PSAM Model deformation region and thickness cross section

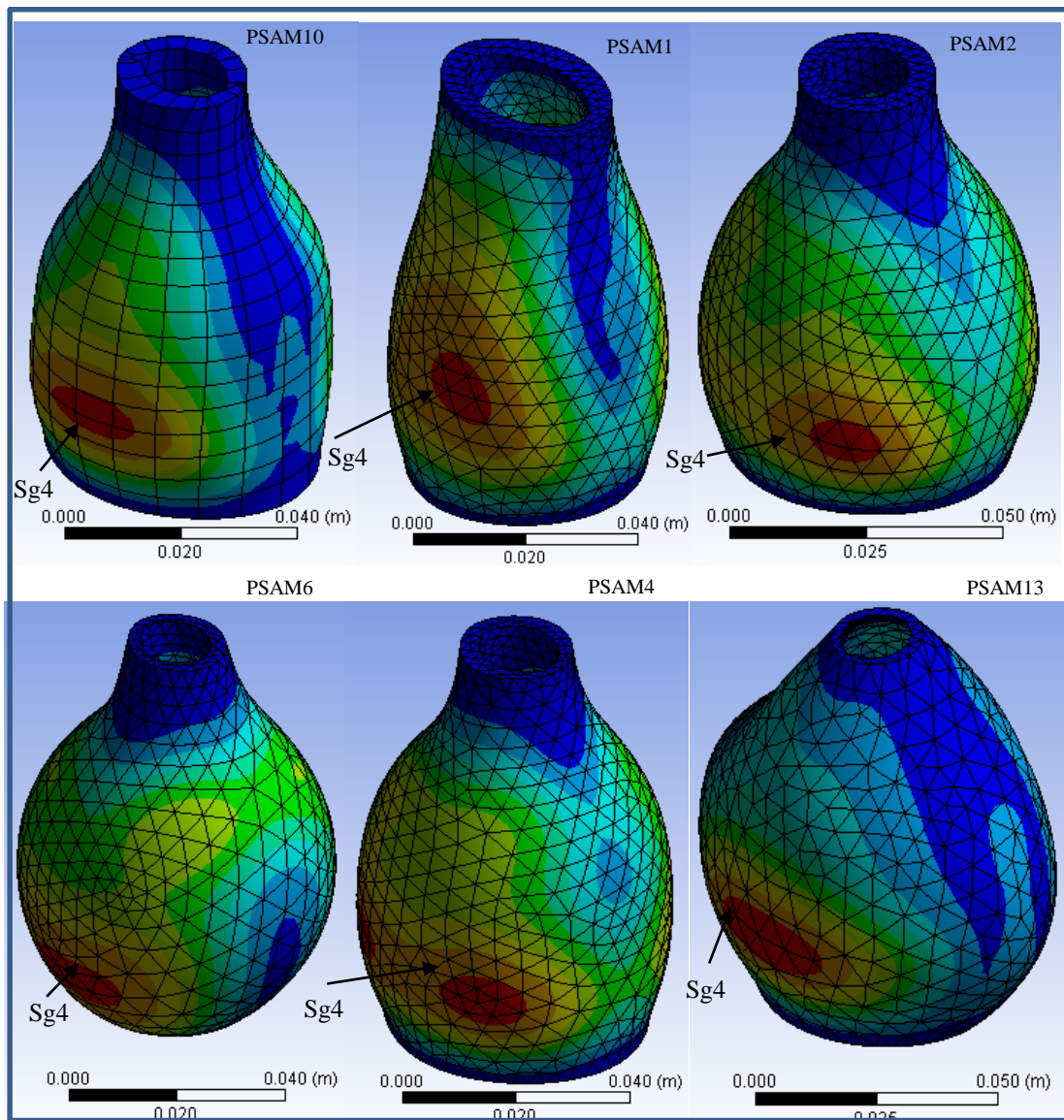


Figure 5. 15: Aneurysm deformation at affected region at point A in suspected segment

Data are extracted from these simulation results based on the affected region from model cross sections as shown in Figure 5.14. The specific regions for each affected area are identified over each segment before the thickness is figured. If the thickness does not correspond to the maximum diameter, the overall factors that contribute to this high deformation area are considered and tabulated in Table 5.3 based on P-SARP protocol in Section 4.3.1. The thickness is according to measured values from US as discussed in Section 5.2. These values show that the thickness does not totally rely on maximum diameter when an aneurysm deformed.

**Table 5. 3:** PSAM High Deformation

Patient	High Deformation Observed		
	Point	Segment	Thickness (cm)
PSAM1	A	4	0.5
PSAM2	G	4	0.53
PSAM3	C	3	0.53
PSAM4	G	4	0.24
PSAM6	A	4	0.53
PSAM7	G	4	0.34
PSAM8	A	3	0.4
PSAM9	A	2	0.26
PSAM10	A	4	0.56
PSAM11	A	3	0.53
PSAM12	A	3	0.29
PSAM13	A	4	0.37

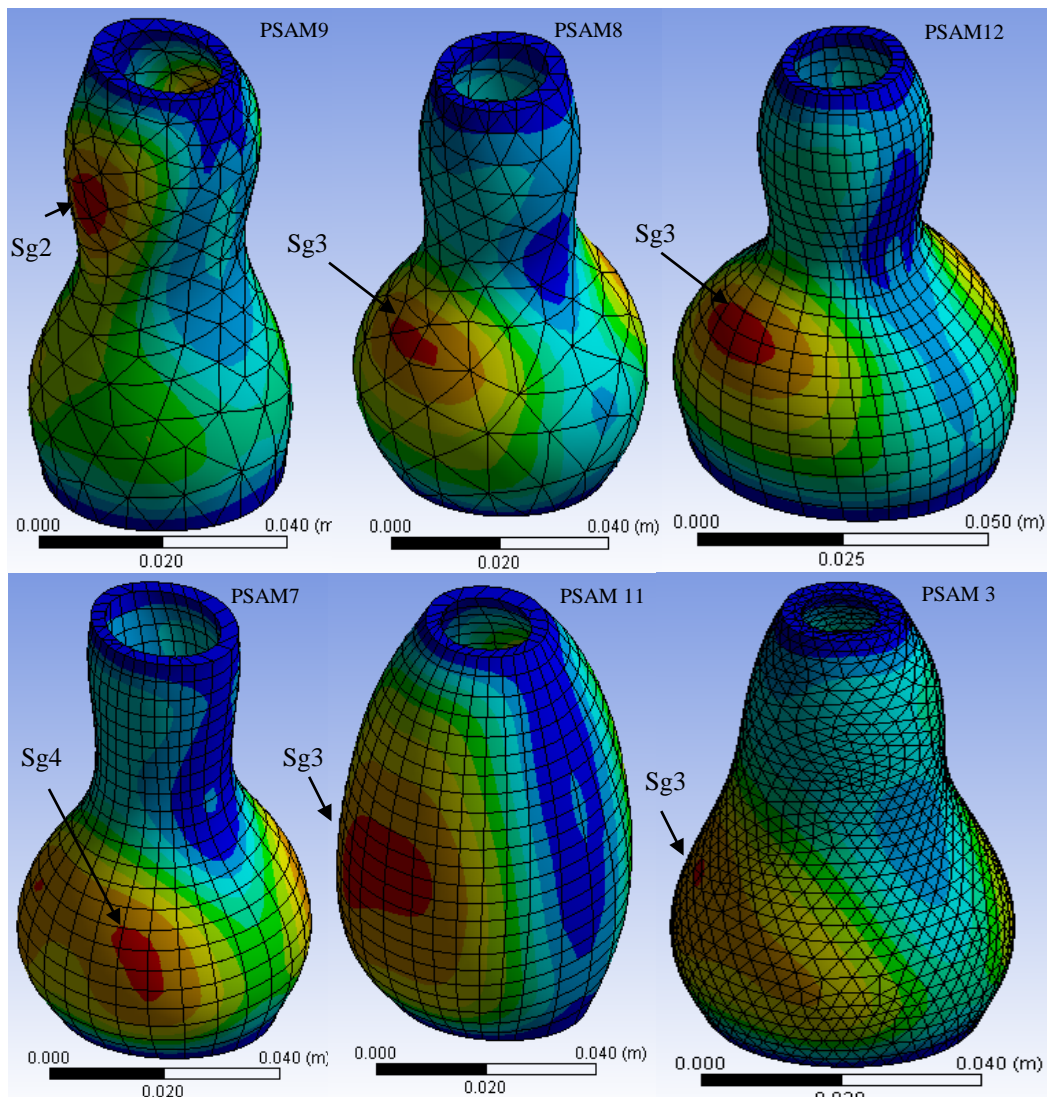


Figure 5. 16: Aneurysm deformation at different point and segments

#### 5.4.2 Maximum Stress Region

ANSYS modelling provides a better insight of high stresses occurred after the vessel being pressurized (Figure 5.17). The maximum stresses are larger on the unspecified surface but would typically correspond to the anterior surface due to the presence of the spinal column on the posterior as explained in Section 5.2 and Figure 5.1. These results are consistent with the fact that wall is more tensioned on the flatter surface in segment 3 (the most stretched/deformed region) and at the posterior side. There is no external support specifically that could be stopping the wall deforming during loading pressure rather than the blood vessel itself which is the most affected point. This could explore the possibilities of reliable information to guide the clinical management of the aneurysm disease.

The results related to a thrombus, Schurink et al. [153] showed that the presence of a thrombus during aneurysm did not reduce the mean and the pulse pressure near the aneurysmal wall, thus thrombus will not reduce the risk of rupture of the aneurysm. However, the existence of thrombus which behaves like the tissue wall, will have a more significant decrease in strength with respect to the number of load cycles that indicate its vulnerability against fatigue failure which will be discussed in Chapter 6.

The maximum stresses in other PSAM models shown in Figure 5.18 are observed to define the determinant factor that contributes to maximum wall stress (which could lead to rupture). Further from this maximum and minimum stress obtained from the result, the mean stress and the alternating stress can be calculated from each model using equation (Equation 5-2 and 5.3). Considering pulsatile at one time produce maximum wall stress during peak systolic and minimum stress is diastolic (non-zero mean stress).

$$\text{Mean Stress} = \frac{\text{Minimum stress} + \text{Maximum stress}}{2} \quad (5-2)$$

$$\text{Alternating Stress} = \frac{\text{Maximum stress} - \text{Minimum stress}}{2} \quad (5-3)$$

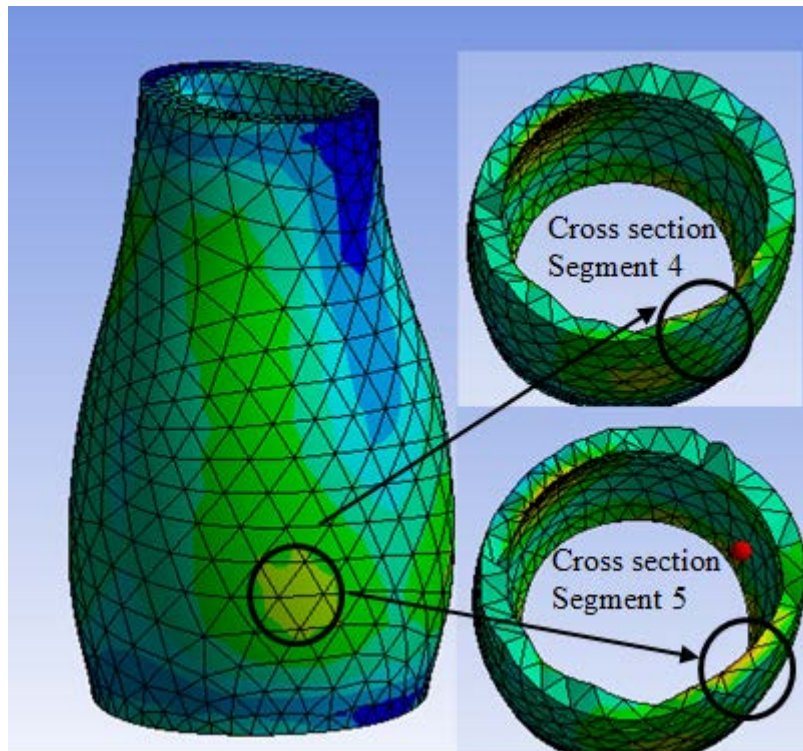


Figure 5. 17: Maximum Stress region location (a) and High Strain Energy (b) at segment (sg) 4 and 5

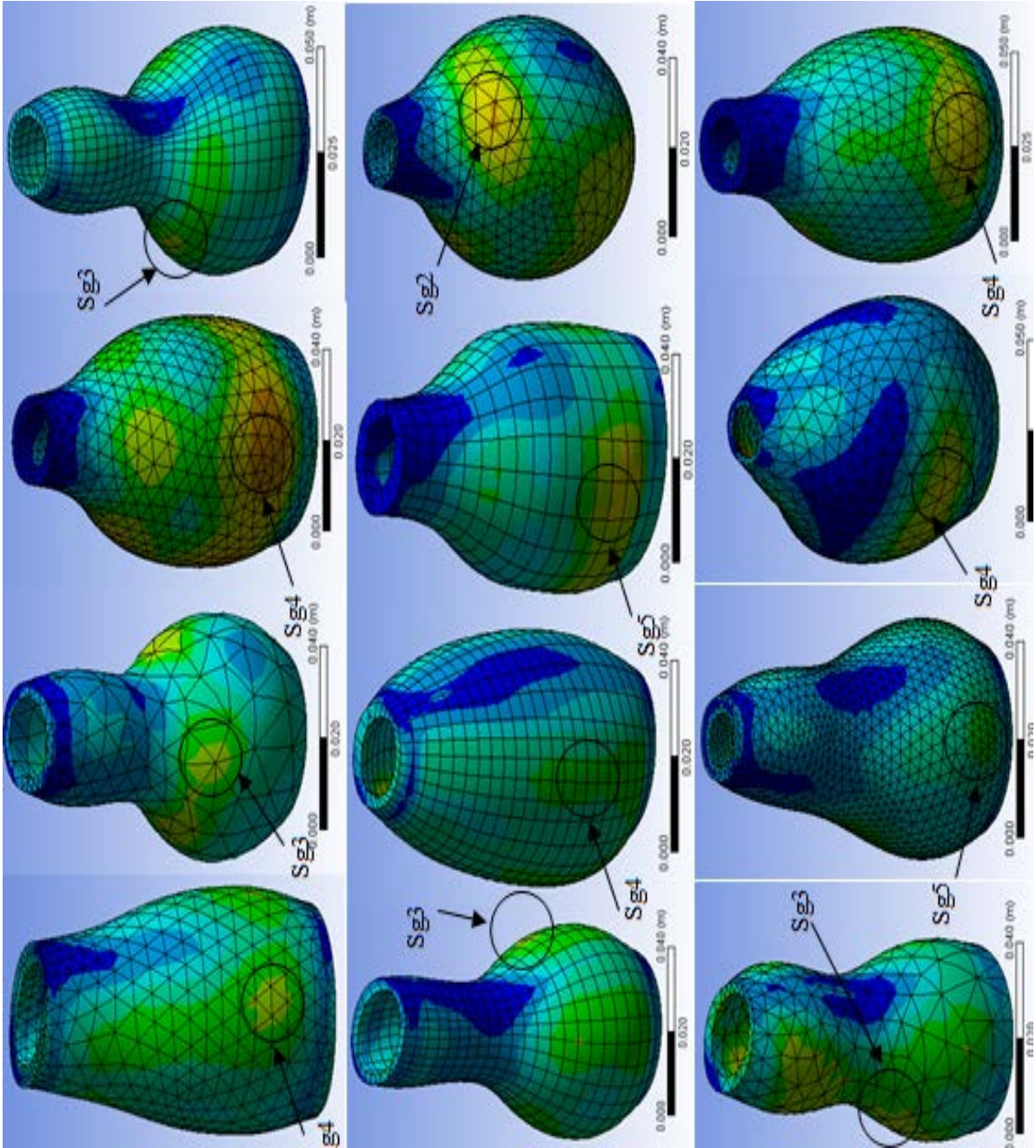


Figure 5. 18: Maximum Stress for PSAM

### 5.4.3 Ultimate Strain Energy Region

Since the strain energy is defined as the energy dissipated in each of the loaded models with one pulsatile flow, it provides good information in understanding the effected region in the aneurysm model as shown in Figure 5.19. Even though it forms more strain energy at the close region where maximum stresses were obtained, it also leads one to visualize more regional spots with a high inclination to ultimate energy strain. Looking into aneurysm models in Figure 5.20, there are multiple regions that show high energy strain due to multiple variant parameters to be observed further in determining the contributing factors of rupture. Multi-region maximum strain energy obtained on different segments show that any surface has a high tendency of the rupture. From the figure 5.19, we observe that each critical point corresponds to reach a useful conclusion by referring to the affected aneurysm location from the US images.

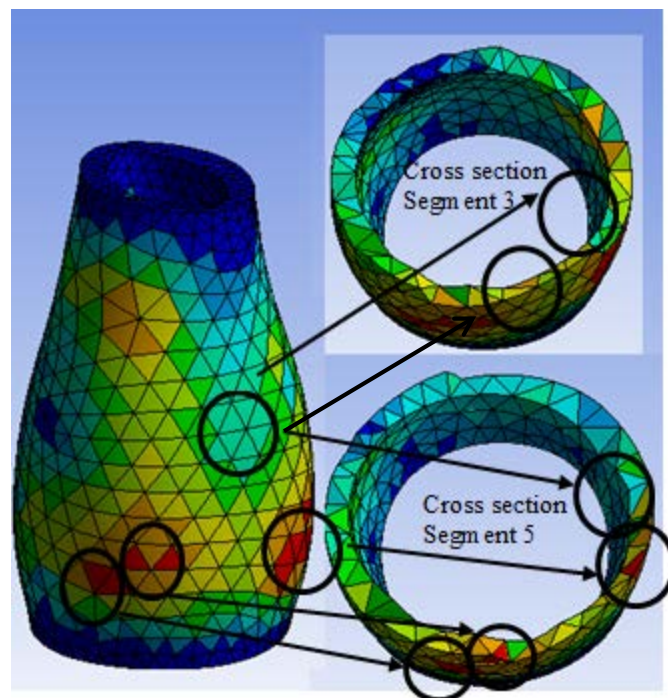


Figure 5. 19: High Strain Energy at segments (Sg) 3 and 5

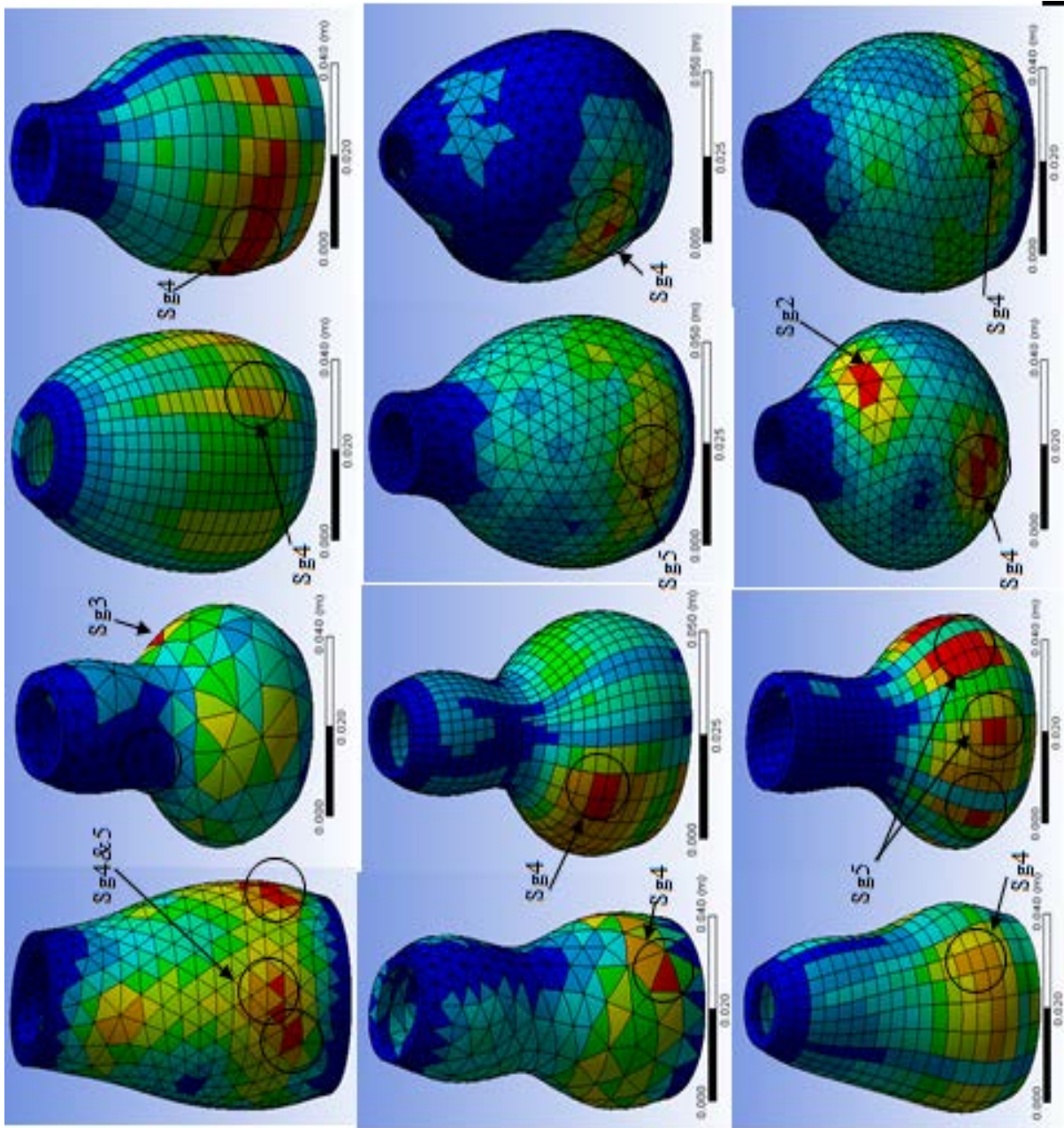


Figure 5. 20: Various strain energy point on aneurysm PSAM model

## 5.5 Closure

In growing aneurysm, elevated wall tension strength may lead to sudden rupture. An ultimate strength of the wall tissue is unpredictable by looking from any *in vivo* image modalities from the patient. But, it is possible to interrelate the behaviour of the tissue that is already unstressed from *ex vivo* specimen testing. Currently, only limited resources are available for estimating wall stress and strength *in vivo*, necessitating *ex-vivo* specimen testing [73]. Using various tensile specimens testing, initial estimation of the weakened tissue progress to rupture can be calculated by studies on biomechanical properties as discussed in Chapter 3. Chapter 6 will discuss how the wall deformation based on computational results compare with specimen *in vitro* testing results to postulate rupture prediction.

## CHAPTER 6: ANEURYSM WALL DEFORMATION AND RUPTURE

### PREDICTION

#### 6.1 Introduction

This chapter discusses 1) geometrical aspects of the failure which can be incorporated by modelling and structure characterization; 2) physical aspects of blood vessel tissue failure. The geometrical aspect is based on AAA geometry variation which is a normal practice used by the medical community in assessing aneurysms. The physical aspect is based on engineering concepts of failure theories. Two approaches are discussed here, one based on the biaxial state of stress testing and the second is based on the cyclic loading generated by the pulse wave.

#### 6.2 Geometric Aspects of Failure

Statistical evaluations were performed to analyse the high contribution parameters to aneurysm rupture using geometric data from *in vivo* US image. The Correlation Coefficient (Correl) and Regression were evaluated to develop specific prediction criteria based on geometry. This evaluation provides a relative risk for rupture over region and affected thickness for each PSAM.

The Correl is a statistical value that delivers the strength of the linear relationship between two variables [154]. The Pearson's correlation coefficient ( $r$ ), for each relationship from this geometric analysis was determined to measure the association between the thickness and segment of the mode using Excel<sup>TM</sup>. It is defined by Equation 6-1 as

$$Correl(x, y) = \frac{\sum(x - \bar{x})(y - \bar{y})}{\sqrt{(x - \bar{x})^2 (y - \bar{y})^2}} \quad (6-1)$$

where  $\bar{x}$  and  $\bar{y}$  the variable samples are means average (variable 1) and average (variable 2). However, the regression coefficient was determined using [155].

$$y_i = \beta_1 X_{i1} + \dots + \beta_p X_{ip} + \varepsilon_i = X_i^T \beta + \varepsilon_i \quad (6-2)$$

$$i = 1, \dots, n$$

Where  $y_i$  is dependent variable,  $X_i$  is independent variable,  $\beta$  is P-dimensional parameter vector,  $\varepsilon_i$  is noise and T denotes the transpose, so that  $x_i^T \beta$  is the inner product between vectors  $X_i$  and  $\beta$ .

Regression slope analysis was performed to evaluate the rupture risk contribution based on aneurysm segmentation over the thickness of the aneurysm wall. Using four different points (Figure 5.1) to represent the circular size of the circumferential image of aneurysm, it is possible to investigate the affected location related to human physiology. For example, point A is located opposite to point E which is supported by the body's spine. When there is a deformation, the most affected thickness happens at the location without spinal support; at point A, C and G, see Table 6.1. However, observing the significant affected points due to the thickness in vertical and horizontal deformation, it is concluded that point A is more significant compared to other points. When observing through the segment, A3 is more significant to the thickness from both deformations followed by segment A5. This explains that when the diameter increases at A4 and A5, the most affected thickness due to the high stretching occurs on A3 in all directions.

**Table 6. 1:** Thickness per Segment Level Measurement (cm)

	Patient 1	Patient 2	Patient 3	Patient 4	Patient 5	Patient 6	Patient 7	Patient 8	Patient 9	Patient 10	Patient 11	Patient 12
A	0.56	0.48	0.4	0.32	0.29	0.26	0.3	0.26	0.29	0.4	0.39	0.32
C	0.34	0.5	0.29	0.19	0.32	0.29	0.32	0.21	0.19	0.29	0.26	0.34
E	0.37	0.42	0.26	0.34	0.24	0.21	0.23	0.21	0.26	0.53	0.23	0.26
Level 1	G	0.48	0.42	0.32	0.32	0.24	0.27	0.21	0.4	0.37	0.34	0.34
A	0.56	0.53	0.25	0.37	0.4	0.56	0.29	0.37	0.26	0.34	0.53	0.37
C	0.4	0.4	0.32	0.24	0.34	0.32	0.32	0.21	0.29	0.37	0.37	0.29
E	0.26	0.42	0.4	0.25	0.24	0.4	0.29	0.32	0.26	0.34	0.4	0.34
Level 2	G	0.37	0.29	0.32	0.24	0.37	0.34	0.32	0.26	0.34	0.32	0.24
A	0.66	0.5	0.4	0.32	0.5	0.48	0.29	0.4	0.26	0.69	0.53	0.29
C	0.32	0.42	0.53	0.29	0.4	0.34	0.37	0.4	0.4	0.5	0.4	0.34
E	0.45	0.42	0.37	0.26	0.37	0.29	0.34	0.37	0.24	0.53	0.37	0.34
Level 3	G	0.48	0.34	0.26	0.19	0.42	0.29	0.32	0.34	0.74	0.42	0.29
A	0.5	0.58	0.45	0.34	0.45	0.53	0.32	0.37	0.37	0.56	0.53	0.34
C	0.26	0.24	0.29	0.21	0.32	0.42	0.26	0.26	0.35	0.32	0.4	0.32
E	0.48	0.4	0.5	0.21	0.42	0.32	0.32	0.45	0.32	0.45	0.34	0.32
Level 4	G	0.34	0.53	0.32	0.24	0.42	0.34	0.42	0.26	0.32	0.29	0.37
A	0.5	0.53	0.45	0.29	0.4	0.37	0.4	0.4	0.48	0.5	0.32	0.4
C	0.4	0.34	0.48	0.34	0.32	0.42	0.37	0.29	0.37	0.37	0.32	0.32
E	0.48	0.4	0.32	0.32	0.26	0.21	0.32	0.34	0.32	0.4	0.29	0.34
Level 5	G	0.48	0.53	0.45	0.34	0.45	0.29	0.4	0.37	0.45	0.34	0.34

The  $r$  values for vertical segments 3 to 5 as a function of thickness were 0.649, 0.211 and 0.407, respectively. For horizontal segments 3 to 5 as function of thickness were 0.415, 0.108 and 0.407, respectively. These correlation coefficients are statistically insignificant ( $r > 0.8$  for statistical significance) and this is due to the biological variability in tissue.

Table 6. 2: Regression summary based on thickness variation in each segments

Segment	Thickness Point (P value)			
	Vertical Deformation		Horizontal Deformation	
	Point A	Point E	Point C	Point G
A1	0.174	0.900	0.698	0.018
A2	0.228	0.261	0.096	0.037
A3	0.002	0.010	0.034	0.100
A4	0.149	0.268	0.382	0.565
A5	0.611	0.082	0.041	0.095
Overall (Vertical)	0.002	0.570	0.109	0.694
Overall (Horizontal)	0.004	0.858	0.064	0.433

An informal interpretation of a  $p$ -value, based on a significance level of about 10%, might be [156]

- $p \leq 0.01$ : very strong presumption against null hypothesis
- $0.01 < p \leq 0.05$ : strong presumption against null hypothesis
- $0.05 < p \leq 0.1$ : low presumption against null hypothesis
- $p > 0.1$ : no presumption against the null hypothesis

### 6.3 Physical Aspect of Failure

In this respect, two failure hypotheses were proposed; i) ultimate strength of the tissue specimen, and ii) number of cyclic loads due to fatigue. To understand the basics of vessel wall hemodynamic failure, knowledge of the elastic and viscoelastic properties are important. The tissue behaviour was investigated in terms of the stress-strain relationship and ultimate tensile strength (UTS) through *in vitro* specimen testing. Both were taken into consideration to investigate AAA rupture mechanisms. This chapter contains:

- 1) Tissue experimental raw data, true stress and true strain are calculations
- 2) A comparison between modelling parameter results (e.g. maximum stress and maximum strain) with experimental data to find stress distribution and wall straining effect in aneurysms in Chapter 5.
- 3) An investigation into the relation between the modelling results and the experimental data in order to formulate some hypothesis on rupture prediction.

From experimental investigations [123, 124], it has been reported that there were two possible mechanisms to initiate AA rupture. One was based on tensile loading where the tissue is loaded in a biaxial state until failure. The other was based on the principle that the blood flow pulses produce cyclic loading which may lead to failure. Both of these hypotheses were tested against the computer simulation mode in order to formulate an appropriate algorithm for rupture. Six tested specimens from various locations were analysed to identify the specific region of rupture and strain energy required to rupture. This serves to formulate some understanding of the weakest points in aneurysm.

This chapter is divided into three sections (Figure 6.1) to focus on mechanics of tissue strength followed with a discussion on tissue fatigue from tissue cyclic loading.

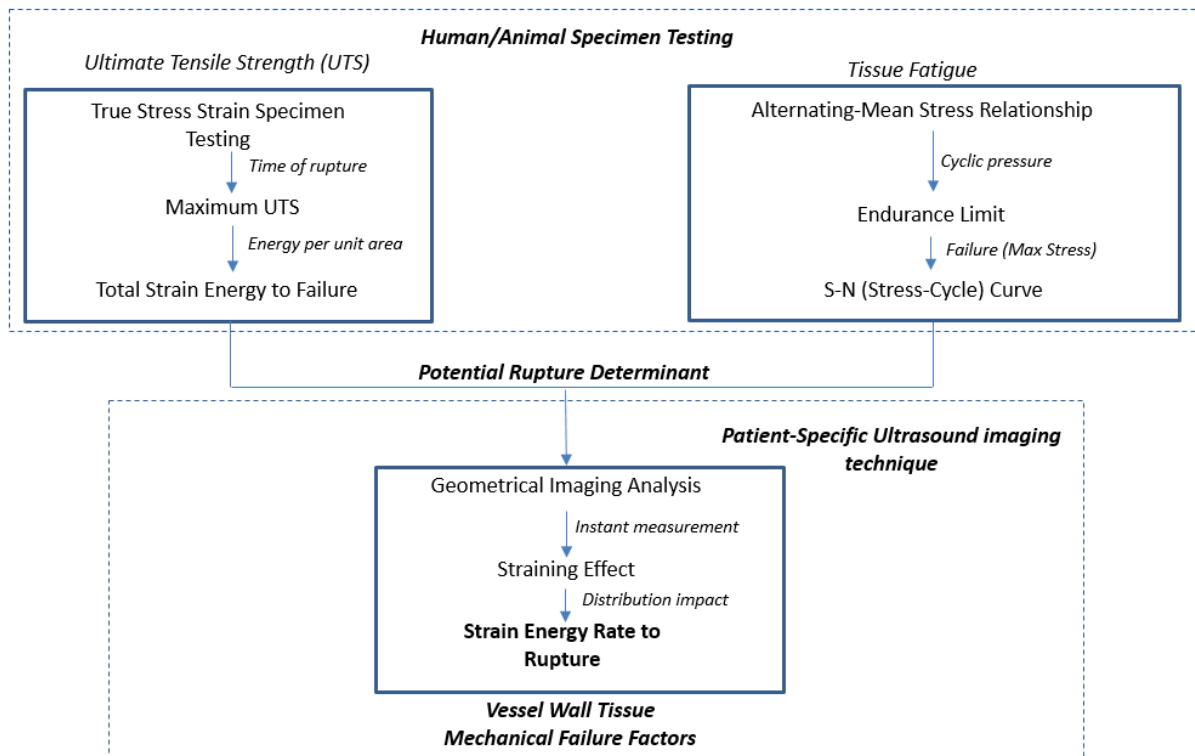


Figure 6. 1: Tissue Failure Prediction Analysis

Understanding failure theories may help in postulating appropriate AA rupture mechanisms. Dealing with biological tissues introduces a surplus of inconsistency. One of the utmost limitations of these experiments is biological variability and the availability of human arteries for testing. For this preliminary step of the research, we investigate our approach using two tests; 1) Experimental data performed in collaboration with our collaborator, Sugita [124] for failure tissue strength to determine the strain energy per unit time; and 2) Available data on cyclic loading on porcine tissue rings [123] to determine the tissue life cycle estimation using the Stress Cycle (S-N) curve. We postulate two scenarios using the available failure theory from the tissue rupture.

## 6.4 Biaxial State of Loading

Human tissues are very difficult to obtain for testing; however, experimental data to support this investigation was obtained through collaboration with Sugita [124]. An experimental setup for tissue testing was developed to test the AA rupture from human tissues. Identifying stress and strain of the real aneurysm specimen requires a specific size to be excised from an aneurysm tissue. A testing device was fabricated to measure the rupture properties of AA. Specimens obtained from AA tissue were clamped in a circular shape. The specimens selected for this study are given in Table 6.3. From this testing we observe four parameters that contribute to the failure when their specific regions are taken into consideration to compare with our simulation results. There were

1. Maximum Stress ( $\sigma_{\max}$ )
2. Maximum Strain ( $\epsilon_{\max}$ )
3. Maximum Energy ( $E_{\max}$ )
4. From above three parameters, we calculate Maximum Strain Energy per unit time ( $U_T$ ) to determine rate of the strain energy.

Table 6. 3: Summary of origin, sex age, position and dimensions of aneurysm specimens

Specimen #	Origin	Sex	Age	Position	Diameter (mm)	Thickness (mm)
H0104A	AAE	Female	74	Descending	50	2.7
H0123	TA	Male	63	Descending	65	4.1
H0108	TA	Male	68	Arch	50	3.3
H0109	AD	Male	70	Descending	62	3.4
H0116A	TA	Male	73	Arch	65	3.8
H0119A	TA	Male	67	Arch	62	4.3

AAE, annulo aortic ectasia; TA, true aneurysm; AD, aortic dissection.

#### 6.4.1 Experimental Setup

The illustration in Figure 6.2 shows the entire experimental setup for the specimen pressure imposed testing. Air pressure was generated from a compressor, regulated with an electro pneumatic regulator, and applied to the specimen using a rubber balloon for gradual pressure to make the specimen bulge into the hole at the pressure rate of 10mmHg until the specimen ruptured or the maximum pressure reached 4500mmHg. The regulator was controlled with a PC through the D/A converter. The actual pressure applied to the specimen was also measured with the pressure transducer and their values were recorded with the PC through the strain amplifier and analogue to digital (A/D) converter.

The images of specimen deformation were captured with CCD cameras placed at both front and lateral sides of the specimen and were also recorded in a video cassette recorder using a digital video mixer and high speed camera at 3000 frame/s, respectively to identify the crack initiation point. Throughout this setup, the pressure and deformation of the specimen until rupture stage by stage were measured until the failure location point of the observed material was pressurized. This helps us to determine a specific region or point where failure occurs before and after the maximum pressure is applied.

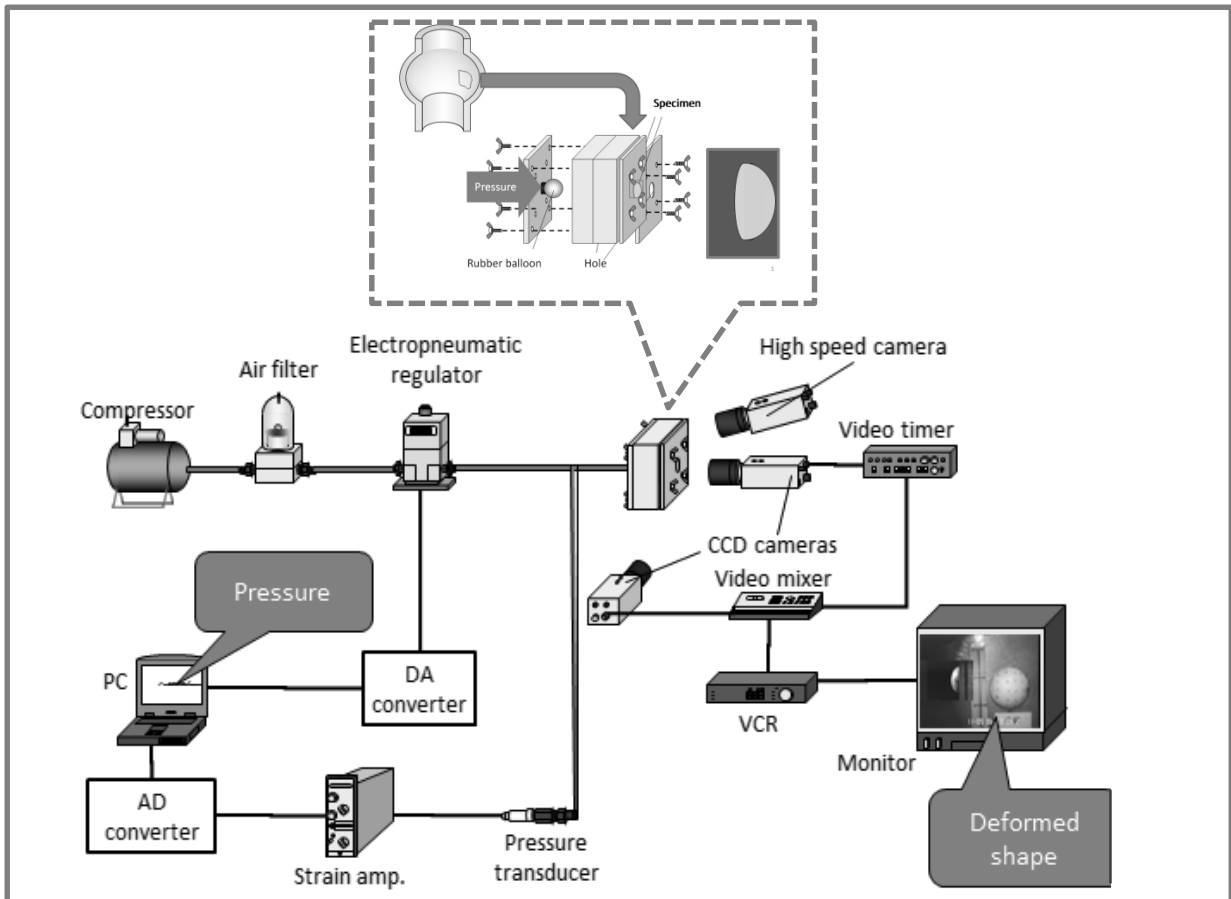


Figure 6.2: Experimental Setup: Schematic Illustration for Pressure Imposed Test Device Setup image with permission from Sugita [124].

#### 6.4.2 Raw Data Analysis

The original raw data obtained from this experiment was based on engineering strain and true stress. However for the current research, using true stress and true strain are more relevant to the anticipated rupture. The engineering strain,  $\epsilon_e$  is given by:

$$\epsilon_e = \frac{l - l_0}{l_0} = \frac{\Delta l}{l_0} \quad (6-3)$$

Where  $l$  = instantaneous length and  $\Delta l$  = the change in length of the original length  $l_0$ . However, to calculate true strain ( $\varepsilon$ ), the formula is calculated based on the instantaneous length and is given by:

$$\varepsilon = \frac{dl}{l} \text{ or } \varepsilon = \int_{l_0}^l \frac{dl}{l} = \ln\left(\frac{l}{l_0}\right) \quad (6-4)$$

The circumferential length of the ellipsoid ( $L_{\text{circumference-ellipsoid}}$ ) was calculated using the approximation formula [68];

$$L_{\text{circumference-ellipsoid}} \approx \pi(a + b) \left[ 1 + \frac{1}{4} \left( \frac{a-b}{a+b} \right)^2 + \frac{1}{64} \left( \frac{a-b}{a+b} \right)^4 + \frac{1}{256} \left( \frac{a-b}{a+b} \right)^6 \right] \quad (6-5)$$

Where  $a$  and  $b$  represent the radius and the maximum diameter.

Using a third-order approximation for the circumference of an ellipse at no load gives  $2r$ .

Equation  $\varepsilon$  can be written as

$$\varepsilon = \frac{L_{\text{circumference-ellipsoid}}}{4r} - 1 \quad (6-6)$$

The true strain according to spheroid and elliptical formulas [68] is based on the level of inflation and the formula components by converting Equation 6-6 into Equation 6.4 as follows (A detailed true stress calculation is explained in Appendix B). Figure 6.3 illustrates how the equation is formulated based on combined geometry.

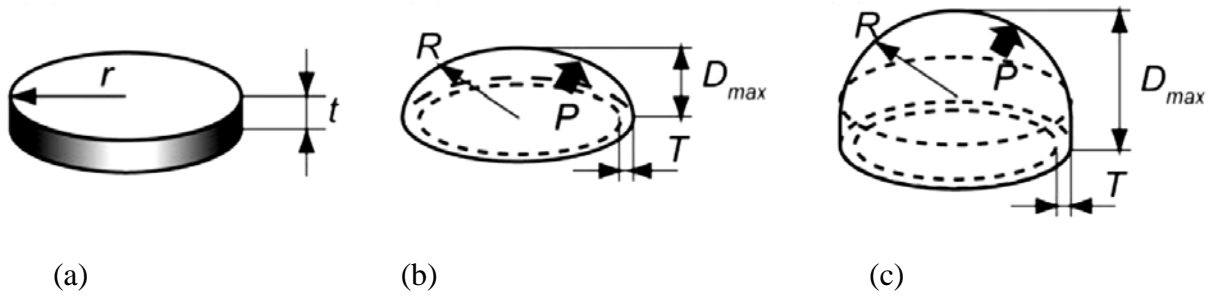


Figure 6. 3: Pressurized Specimen during Inflation Testing (a) Flat surface at no load state (b) Pressure loading supplied until maximum diameter (c) Pressure loading supplied after combined geometry [124]

In this geometric formulation, to calculate true stress and true strain, a combination spheroid formula (Figure 6.3c) and cylinder (Figure 6.3a) are used after considering the shape deformation after the specimen is pressurized. Spheroid geometry is considered when  $D_{max} < r$  and combination geometry when  $D_{max} > r$ , where  $r$  is the radius of the hole of the metal plate;  $t$ , the thickness at the no-load state;  $R$ , the curvature radius of the specimen;  $P$ , the pressure;  $T$ , the thickness of the specimen and  $D_{max}$ , the maximum deformation of the specimen. The new true strain ( $\epsilon_{true}$ ) for above formulation can be written as:

$$\epsilon_{true} = \ln \left( \frac{L_{circumference-ellipsoid}}{4r} - 1 \right) \quad (6-7)$$

By substituting Equation 6-7 into Equation 6-5, the new  $L_{circumference-ellipsoid}$  length as follow:

$$L_{circumference-ellipsoid} \approx \ln \left( \pi(a+b) \left[ 1 + \frac{1}{4} \left( \frac{a-b}{a+b} \right)^2 + \frac{1}{64} \left( \frac{a-b}{a+b} \right)^4 + \frac{1}{256} \left( \frac{a-b}{a+b} \right)^6 \right] - 1 \right) \quad (6-8)$$

This calculation from Equation 6-7 to 6-8 only applies when  $D_{max} \leq r$ . For  $D_{max} \geq r$ , the length on the specimen is equivalent to half of circumferential length (within radius,  $r$ ) plus double the length of the cylinder. The true strain is expressed by obtaining Equation 6-9 and 6-10.

$$\varepsilon = \frac{\pi r + (D_{max} - r)}{2r} - 1 \quad (6-9)$$

$$\varepsilon_{true} = \ln \left( \frac{\pi r + (D_{max} - r)}{2r} - 1 \right) \quad (6-10)$$

The true stress is used to calculate using formulated equation to obtain the specimen true stress and strain. Figure 6.4 shows the true stress and strain graph. The area under the curve represents the total energy required to failure. During the experiment, the load was applied at a certain rate (10mmHg/s). This can calculate the total energy per unit time to rupture for each specimen. From this true stress strain curve we;

1. Manage to design a stress strain curve with respect to different specimen which already are characterized based on their excised origin
2. Calculate the amount of energy required for each specimen to failure using the energy rate formula
3. Amount of the average energy required for each specimen to failure
4. Classify specimen characteristics from the experiment for a comparison study with the simulation model which is based on US.
5. Identify the particular point at which instability appears to absorb the energy prior to fracture from the deformed image.

### 6.4.3 Prediction Factors from True Stress Strain Curve

In the true stress and true strain data calculations, tangent modulus values were averaged from all specimen curves in Figure 6.4 referring to the stress-strain behaviour of specimens. These material properties are used for modelling purposes. However, the tissue specimen pre-stressing condition before testing is neglected due to its small impact on the zero reference strain at the beginning of the stress value measured.

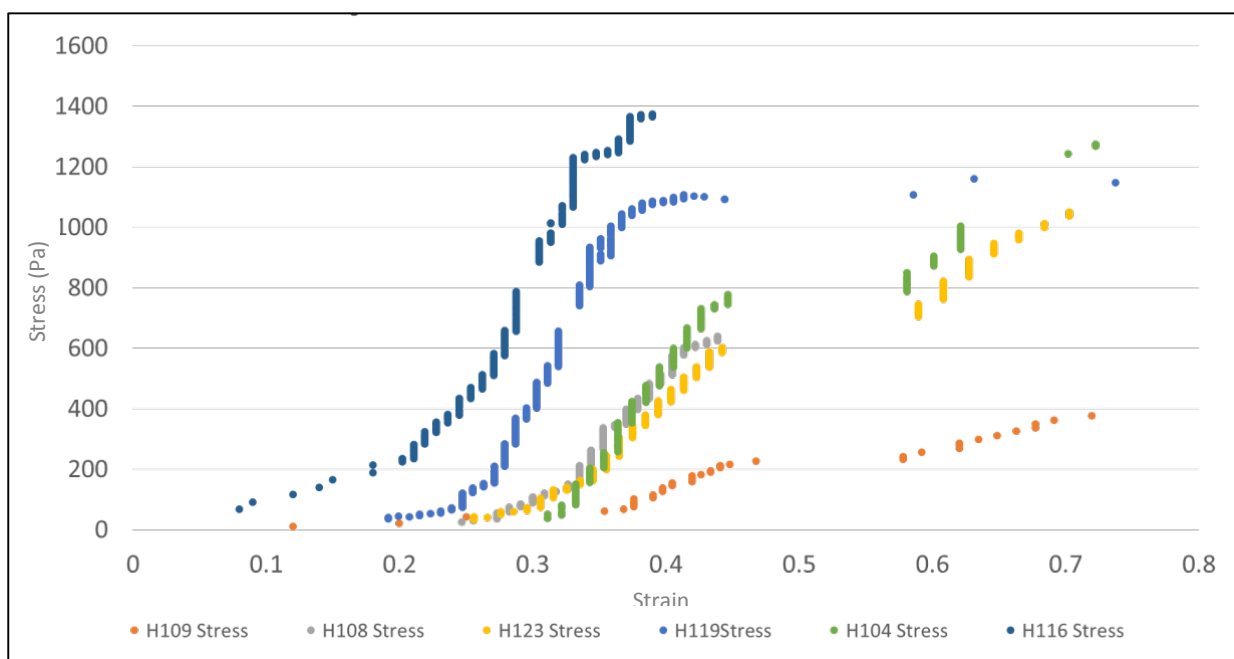


Figure 6. 4: All Specimens True Stress and True Strain Curve

All specimens were categorized into three groups of cohorts to distinguish between the diameter of the patients and group of the specimen where it originally excised from. A Young's Modulus ( $E$ ) assumption is used to represent all specimens' material properties when working in computational modelling. All the calculated data were tabulated by referring to a patient specific diameter range classification in Table 6.2.

All the samples rupture at stresses between 0.3-1.3MPa. Therefore, rupture can be predicted if the stress in the wall is within this range or determined to be higher than 1.3MPa. Knowing a range for ultimate strength as well as maximum wall stress, provides a good diagnostic tool which has not been previously defined. Defining this value proposes the possible rupture range based on unruptured arteries which also provides a basis to compare the changes in time that effect aneurysm progress. Strain energy is calculated based on the stress-strain curve from true stress and true strain specimen curve

We calculate the energy rate using the below equation:

$$\text{Energy per unit Time } (U_T) = \frac{\text{Total Energy required to rupture}(U_f)}{\text{Time}} \quad (6-11)$$

Where  $U_f$  is calculated from Equation 3-3 and time is the total time for a specimen to rupture *in vitro*. All the specimens energy rate ( $U_T$ ) were calculated and classified according to the range of aneurysm diameter, the thickness and specific region where the specimens are excised from Table 6.3. From this, the strain energy, maximum stress and maximum strain deformation from simulated results from aneurysm models are compared with experimental values to postulate failure criterion. Various results from different models can be seen in Table 5.3 where the output is obtained from aneurysm simulation results. Using multiple parameters in assessing the input model, we specifically calculate strain energy and stresses to compare with calculated experimental data in Chapter 7 for analysis and discussion.

Table 6. 4: Patient Specific Diameter Range Classification

Cohort #	Diameter (cm)	In range excised specimen from Sugita experimental data	Average Energy per Unit Time ( $U_T$ )	Relative Patient data from Ultrasound Image	Average Ultimate Strength, UTS (MPa)	Total Energy to failure (J)
1	4.0-5.4	H104 (5.0) & H108(5.0)	0.41	P1,3,4,5,7, 9, 11& 12	0.96	76.64
2	5.5-6.4	H119 (6.2)	0.37	P2,6,8,10	1.15	140.75
3	6.5 above	H116 (6.5) & H123 (6.5)	0.49	P13	1.21	156.47

Table 6. 5: Specimens Strain Energy per unit time

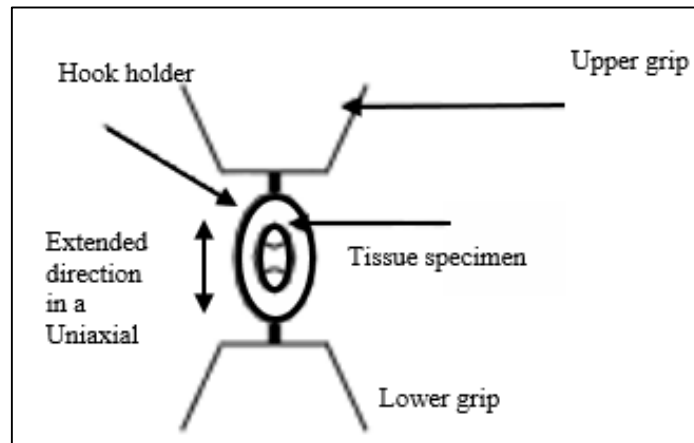
	H109	H108	H123	H119	H104	H116	Average
<b>Energy to Failure, <math>U_f</math> (J)</b>	59.86	57.02	154.08	140.75	96.27	158.86	111.14
<b>Stress to Failure (MPa)</b>	0.37	0.64	1.05	1.15	1.27	1.37	1.10
<b>Time to Failure (Sec)</b>	49.00	152.00	284.00	381.00	214.00	368.00	254.99
<b><math>U_T = dE/dt</math> (J)</b>	1.22	0.38	0.54	0.37	0.45	0.43	0.56

## 6.5 Tissue Fatigue Cyclic testing

Wall tissue motion in this experiment is measured by a technique under pulsatile pressure or cyclic loading because the heart rate provides the information on the wall behaviour. These measures tend to dominate the relationship between pulse pressures and changes in the size of the wall based on number of cycle. In *in vivo* aneurysm studies, inconsistencies in heart rate cycle spontaneously changes blood pressure as well as the internal forces on the arterial wall of aneurysms. Considering the number of consistent heart rates during a certain period of time through a variation in percentage value, leads to an understanding on the number of cycles estimated. The cyclic fatigue tested by Gilpin [123] using test profiles specifically to distinguish between high ultimate stress percentage and low ultimate stress in terms of number of cycles is further evaluated and discussed in the next section.

### 6.5.1 Experimental Setup

The only available fatigue test for AA was given by Gilpin [123]. Tissues were initially preconditioned before being loaded with pressure values at specific amplitudes for 5000 cycles at a rate 1.5 of Hz. Before loading, the tissue needed to be positioned onto two hooks as shown in Figure 6.5a. The profile (Figure 6.5b) was run repeatedly until the specimen failed. If failure occurs before initial value of 5000 cycles, the test was stopped immediately.  $L_a$  is the cycled amplitude that is based on a percentage of the ultimate load,  $F_{ult}$ .



(a)

Command	Control Rate (N/Sec)	Amplitude (N)	Frequency	Number of Cycles
1. Load	0.4 N/Sec	--	--	--
2. Amplitude	--	0.4 N	1Hz	10
3. Load	0.4 N/Sec	--	--	--
4. Amplitude	--	La	1.5Hz	1000

(b)

Figure 6. 5: a) Cyclic Test Setup and b) Profile table

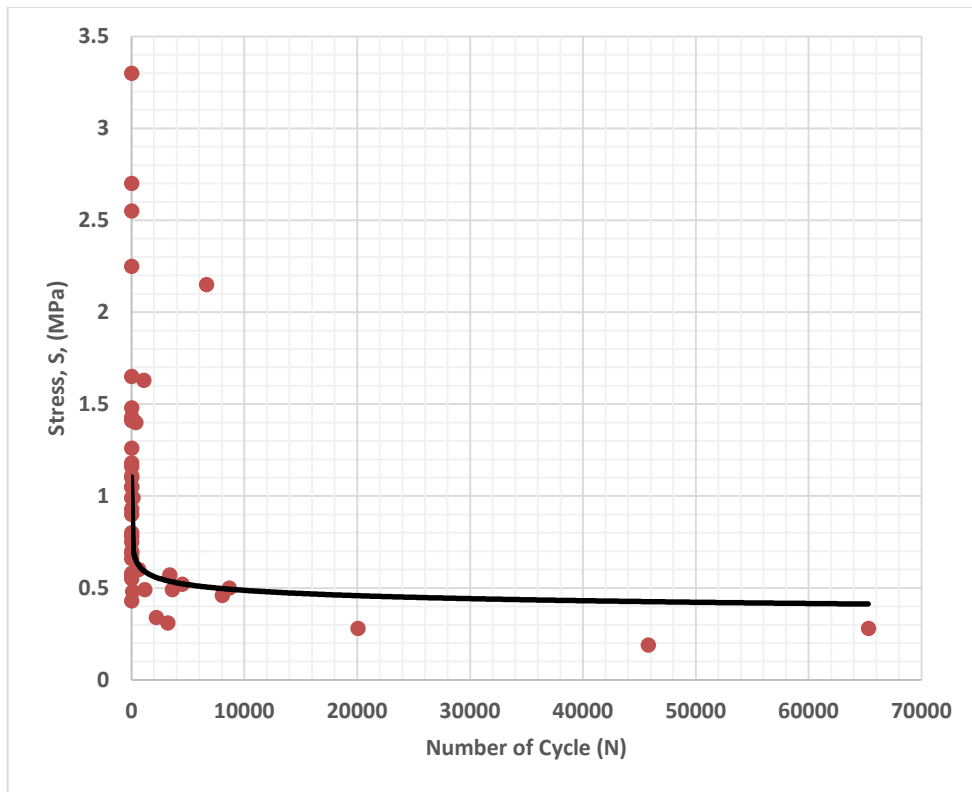
### 6.5.2 Data Analysis

The collected data from cyclic loading experiment is used to perform and to plot the Stress-Cycle (S-N) curve to estimate the potential failure points to predict failure. This curve is plotted based on pressure-cycle loading estimation that can be proposed for clinical application of real tissue. The local stress can be represented by blood pressure which may affect the vessel dilation. Thus, knowing these stress factors (under cyclic loading), the number of cycles to rupture is able to be predicted. Even though the exact number of cycles is hardly estimated, a range of the estimated time is better than no estimate leading to events such as unpredictable aneurysm rupture [123]. The data observed is substantial for aneurysm failure because of the

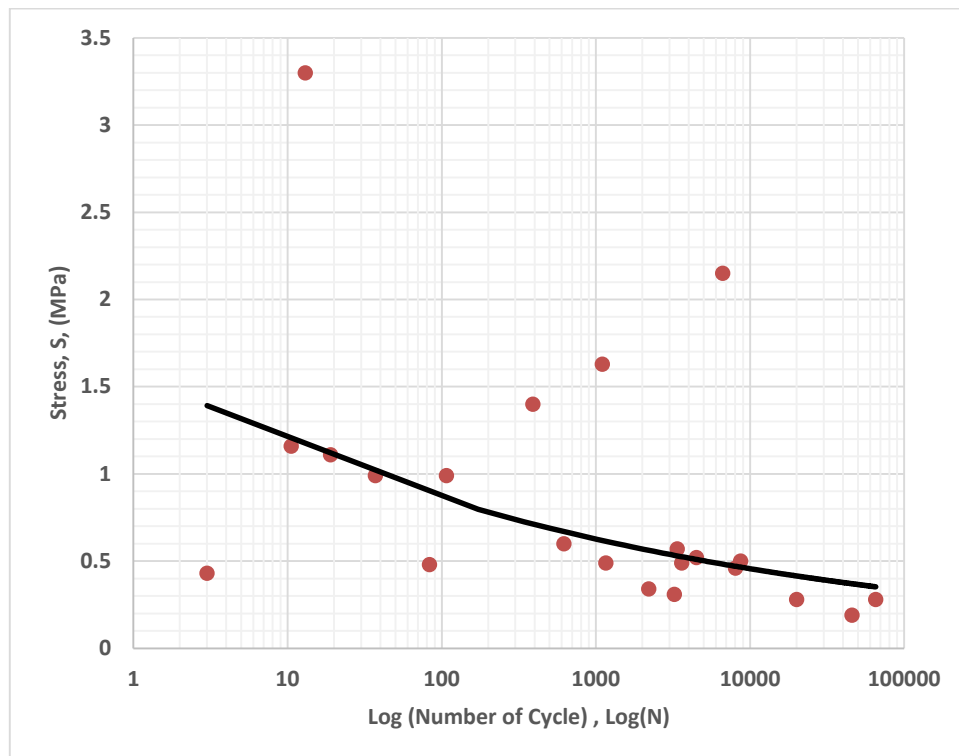
thickness influences as discussed in Section 5.2. Therefore, this could lead to higher stresses and energy strain on the tissue wall from normal cyclic loads without considering the local tissue diameter size. As a result, it is significant to know the S-N curve of tissue behaviour to predict the failure from aneurysm according to high potential factors such as stresses and number of cycles.

### 6.5.3 Prediction Factor – Calculated Stress-Cycle Curve (S-N curve)

All the graphs based on the tabulated values (Figure 6.6a and 6.6b) are reconstructed to acquire similar results on cyclic loading testing, also to correlate it so that it can be used for ultimate tissue failure compared to that of Sugita [124] as explained in Section 6.2.1. In order to estimate the failure based on cyclic loading, average failure trend line from Sugita's ultimate strength [124] is plotted in the same graph in Figure 6.7. Using the plotted graph, we further elaborate and discuss the estimation of tissue rupture based on our PSAM in Chapter 7.



(a)



(b)

Figure 6. 6: S-N curve based cyclic loading of specimen [123], (a) Number of cycles and (b) Log (N) cycle

From the cyclic loading result, the stress and endurance limit curve is plotted to estimate the stress endurance limit for tested specimen by Sugita [124]. The UTS values from the specimens are plotted against endurance limit as cyclic loading results [123]. This linear curve will be used for evaluating the progressing of the stress values against the time period and explained in Chapter 7.

A simulated result provides a  $U_T$  that can rely on estimating the strain energy per unit time (in seconds). Considering the estimated heart beat in seconds, we could postulate from the amount of energy required to tissue failure using a calculation shown below:

$$\text{Number of Cycle } (N) = \frac{\text{Total Strain Energy to rupture}}{\text{Time for one cycle}} \quad (6-12)$$

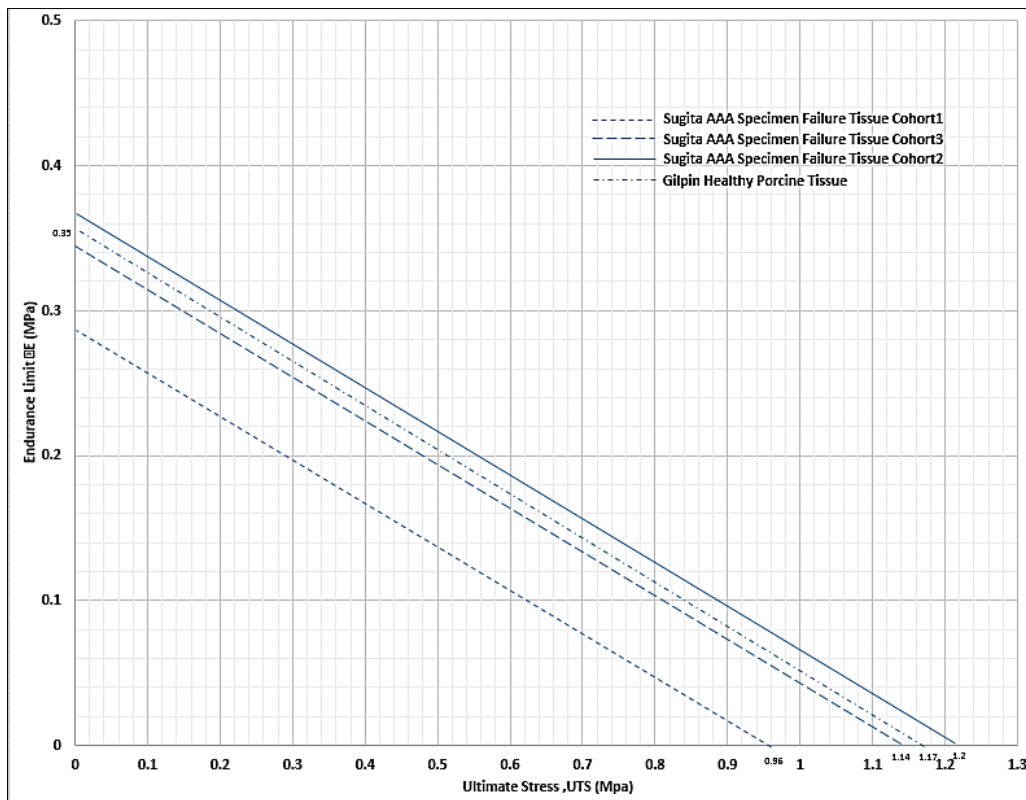


Figure 6. 7: Sugita UTS and Gilpin’s Cyclic Loading Stresses vs. Endurance Limit

## 6.6: Blood Vessel Fatigue to Failure

Failure or rupture of the blood vessel can occur when high amounts of pressure are continuously placed upon the fatigued vessel or the wall stiffness itself becomes weak by time. However, the estimated times need to be correlated with the time of failure as an aneurysm and not only as a specimen. Thus, it is desirable to accurately determine the model of pressure versus fatigue relation in determining the maximum limit strength with varying wall ratios [75, 76, 88, 89]. Using experimental data from tested specimen or similar material for biomechanics stress and strain relating to the rupture, it is expected that we should be able to understand the fundamentals of the complete aneurysm rupture. The numerical experiment also describes the behaviour of more realistic models in which the geometry of the wall material are obtained based on geometry physical impact [36, 61, 90-93].

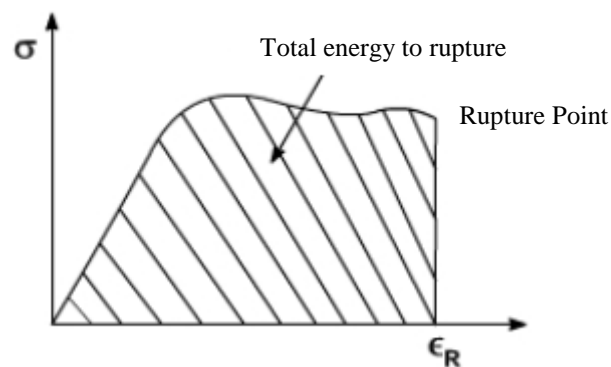


Figure 6. 8: Curve of Total Energy to Rupture

## 6.7: Other Related Prediction Factors

According to the combination of the two failure methods discussed, the failure of the tissue is convincing to be estimated. The measured ultimate strength from both have significant characteristics in the direction of the rupture and from that point, other related factors can also be observed to understand the tissue failure. Physiologically, the cycling of collagen under the

increased load will fatigue the fibres, most likely at an accelerated rate, and ultimately lead to thorough failure [123]. Both failures in the above *in-vitro* experiments demonstrate the trend of decreasing strength with an increased number of cycles and decrease of strain energy. However, other factors are not to be neglected due to a consistent contribution towards the abovementioned failure e.g. cyclic loading and cyclic strain energy. This consideration is necessary to be highlighted when dealing with modelling reconstruction.

### 6.7.1: Cyclic Loading

The relativity of the material fatigue subjected to repeated cyclic loading is theoretically validated in metal and composite study, including in relation to our bodies [88, 157]. Considering the pulsatile waveform imposed in our model, we reconstruct an equation to represent the blood waveform which is more complex. This distorted peak cycle type applies to certain observations that have to be made including the approximated amplitude of sinusoidal waveforms from the cycle period (Figure 6.9). The overall observation of the stress cycle as shown in Figure 6.10 (until 20 cycles) is considered to ensure that the fatigue behaviour is directly affected based on shape and systolic pressure. Since the pulsatile pressure is considered a constant with the number of cycles, the strain of the tissue is expected to gradually increase in small amounts. This condition agrees with the fatigue theory on the strain deformation as discussed in Sec 6.5 that failure occurred whenever the stress value exceeds a maximum deformed limit over time. A cyclic loading experiment result from [123] is applied to correlate the time taken for tissue specimen rupture with gradual pressures.

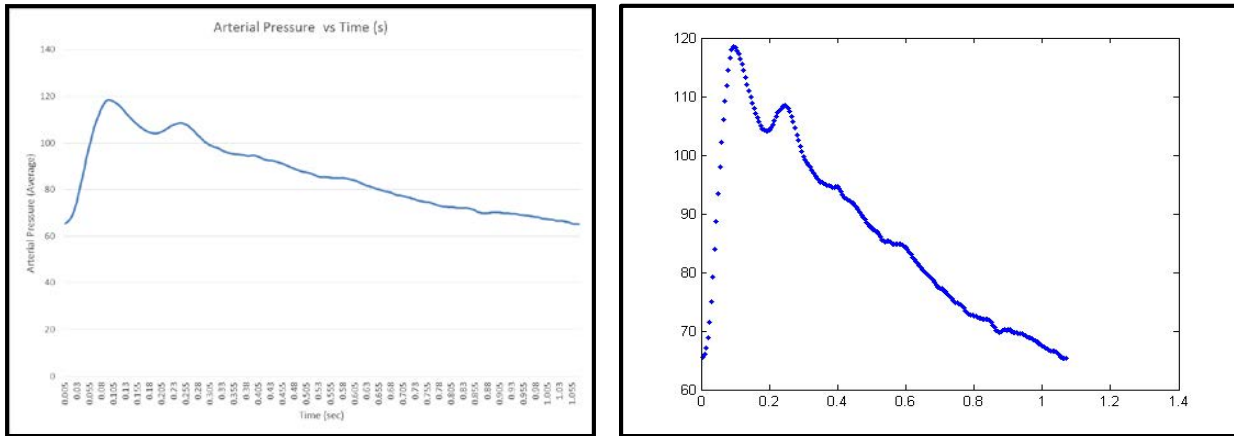


Figure 6. 9: Reconstructed pressure wave for cycle loading modelling

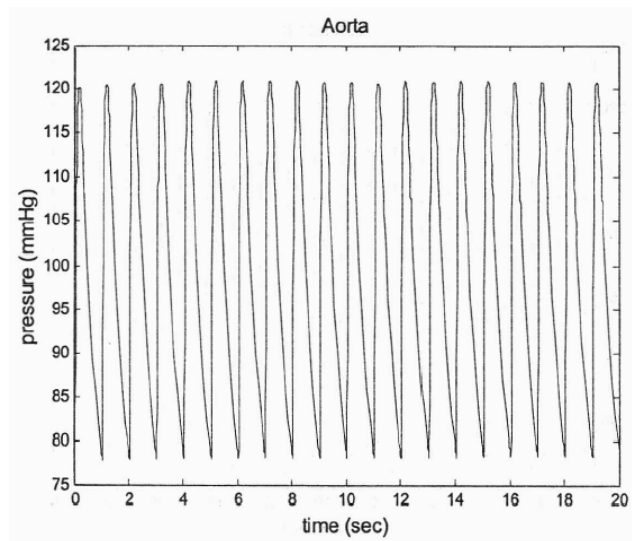


Figure 6. 10: Pulsatile time flow for pressure waveform measured in aorta within 20 sec [158]

### 6.8: Closure

This chapter described how tissues have been tested in a range of strain rates and number of cycles to rupture by experiment. This information is interrelated to research objectives that investigate the aneurysm factor contribution. Therefore, further analysis and discussion to associate the findings from these experiments with our PSAM results from the US imaging technique will be elaborated in Chapter 7. A number of models are developed to study the earlier stage of aneurysm disease (not at critical risk) development. All the correlations from the findings are formulated to establish a practicable formula in aneurysm prediction investigations.

## CHAPTER 7: ANALYSIS AND DISCUSSION

### 7.1 Introduction

This chapter analyses and discusses the mechanisms of the aneurysm simulation results from computational model compared with experimental results in investigating the rupture. The significance of the models developed based on the maximum stress, strain deformation and energy from their specific location is analysed. Therefore, these analyses present a correlation between wall biomechanics and experimental failure criterion. The consequences of the deformed aneurysm models toward the rupture are discussed referring to cyclic loading pressure that measured by fatigue.

### 7.2: Model Geometrical Analysis

A geometrical location is the most feasible parameter that has been investigated by both computational and experimental methods. Affected location also provides some added variable values to be examined. We elaborate on these parameters in different comparison studies in order to determine their significant contributions.

Comparison with a simulated result obtained from modelling for geometrical analysis, shows that the most affected areas (maximum stress, strain and energy) occurred in the region that is closest to maximum (deformed) diameter, as shown in Figure 7.1. An investigation in Section 7.2.1 was established to compare these findings within other available parameters to study the association in rupture prediction.

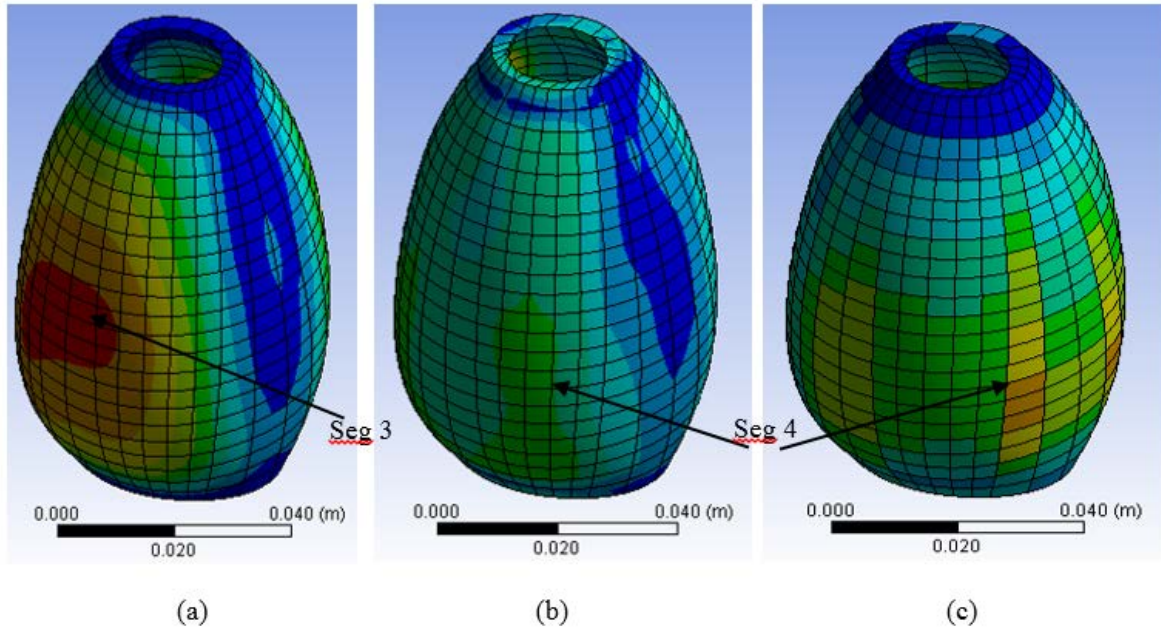


Figure 7. 1: Parameters Comparison Location for a) Max Diameter, b) Maximum Stress and c) Maximum Strain Energy

The tested specimens rupture happened in different regions in the aneurysm wall, but their critical feature is that they are unpredictable. The testing experimental result is analysed to determine the correlation between the different *in vivo* regions from each PSAM compared to *in vitro* excised specimen's characteristics (e.g. patient information where the specimens are originally excised from). Specimen origin location from different parts of the aneurysm region shown in Figure 7.2 is geometrically compared. This comparison explores the importance of the region location related factor for rupture. It has been classified that the related specimen ruptures with their maximum stress, strain deformation and energy are based on the diameter. This comparison leads to further understanding and analysing the possible characteristics for rupture prediction.

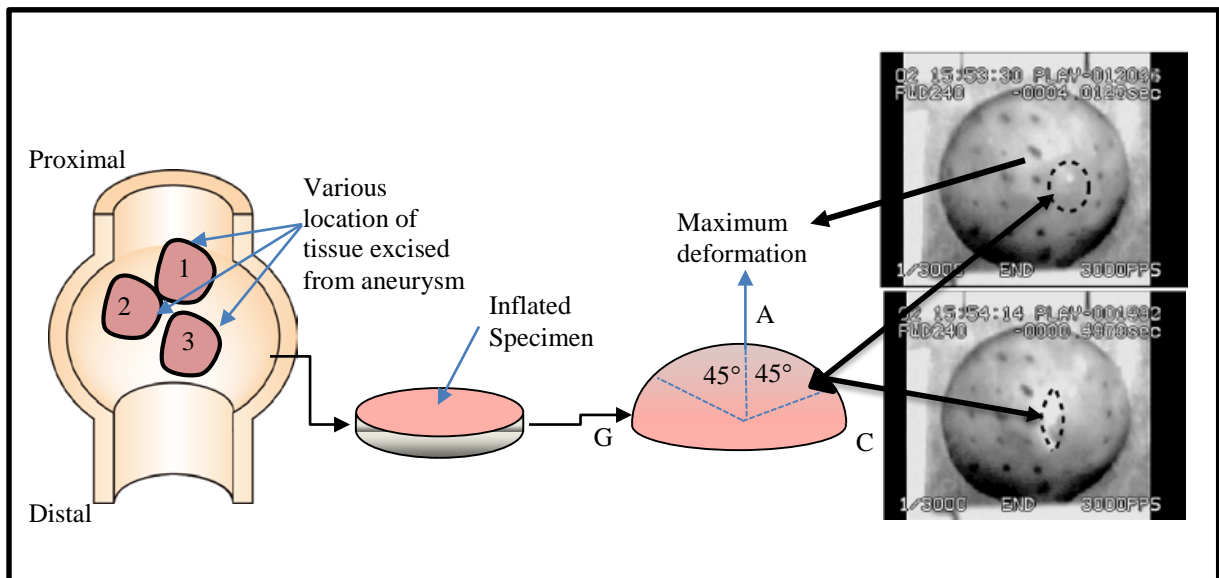


Figure 7. 2: Excised specimen taken from patient aneurysm rupture at multiple region. A high-speed digital image taken from Sugita [124] with permission

As shown in Figure 7.2, regions 1 to 3 are represent one of the excised locations on aneurysm tissues which are close to aneurysm sac maximum diameter. Other excised specimen locations were mentioned in Table 6.1. Since most of the specimens fail near maximum diameter (due to high stretch location) from high speed digital image records, we estimated the boundary to precise failure locations. From the measured diameter and maximum stress values at  $0.98 \pm 0.39$  MPa, both PSAM and experimental results were further analysed in Section 7.3.

### 7.2.1: High Risk Location and Affected Factors

Table 7.1 shows the segment location obtained from our modelling result with respect to patient specific characteristics such as location, height and weight. A high risk location related parameters based on high deformation aneurysms from the aneurysm model is explored. From there, the correlation based on grouping diameters with other parameter classifications (e.g.: BMI and diameter) from aneurysm patients was investigated. This provides the correlated parameters to specific locations with high risk of rupture from observation. Refer to Section 5.4 for critical result location and Section 6.4 for segment location)

**Table 7. 1:** High Risk Location Related Factors

Patient	High Risk Geometrical Analysis				
	Segment Location	Max Diameter (cm)	BMI	Height (cm)	Weight (kg)
PSAM1	4	4.31	24.29	159.5	61.8
PSAM2	4	5.74	25.09	72.5	72.5
PSAM3	3	2.84	22.47	59.7	59.7
PSAM4	4	4.82	25.27	83.7	83.7
PSAM5	4	4.45	28.20	77.7	77.7
PSAM6	4	5.17	26.15	81	81
PSAM7	3	2.47	25.60	71.4	71.4
PSAM8	2	2.64	22.34	74	74
PSAM9	4	3.62	24.58	64.5	64.5
PSAM10	3	4.31	21.45	57	57
PSAM11	3	4.44	23.63	80	80
PSAM12	4	3.44	23.77	77	77
PSAM13	4	5.43	23.28	51	51

One of the most widely used diagnostic tools to identify weight problems within a population including underweight, overweight and obesity is Body Mass Index (BMI). From the classification method in the table, we compare a healthy body weight for aneurysm patients with the rupture risk. As a result, we found that 38% of the patients are overweight and the balance of the 62% is in normal weight range. These values show the aneurysm risk does not relate much with obesity or overweight. However, 80% of overweight patients have high risk of rupture at segment location 4. Thus, the weight problem is a less significant factor in rupture risk.

The deformation axis from vertical and horizontal diameter aneurysms measured using the P-SARP method provides an important element to predict the rupture. Diameter and expansion as studied by [23] has among the highest biomechanics factor to contribute to rupture risk. Our findings show the diameter from different deformation axes and various locations are unpredictable parameters and also need to be considered as important rupture elements. Even

though most of the location is assessed from patient data as shown in Figure 7.3 (as maximum diameter); the abovementioned factors could not be ignored.

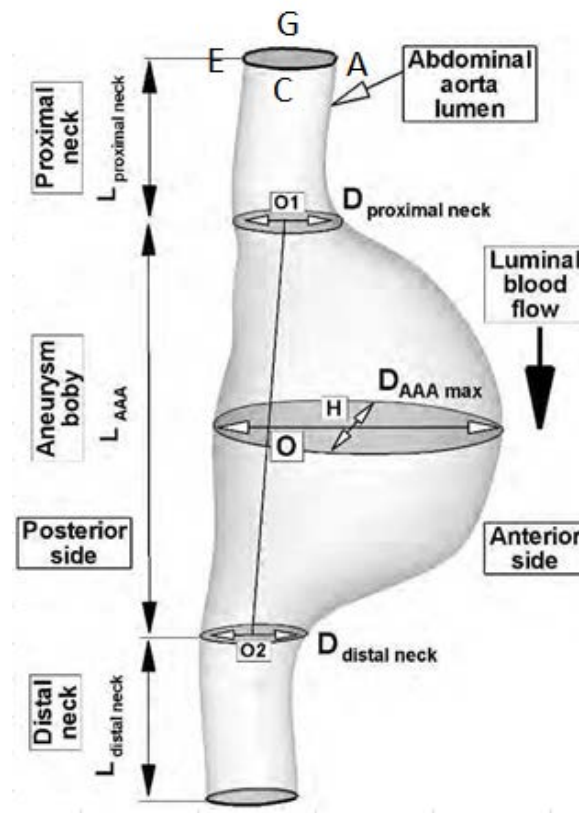


Figure 7. 3: Aneurysm Formation Atlas

Table 7.2 details all the diameter segments for each patient referring to the P-SARP protocol in Section 4.3 where V1 to V5 represent the vertical segment (A to E point) and H1 to H5 represents the horizontal segment (C-G point). After comparison with affected segment locations in Table 7.1, we found that the designated diameter from the modelling results in Section 5.4 were not at the maximum diameter for some of the patients. Almost 84% high risk aneurysm locations happen at low tendency rupture diameter. This indicates the high risk region does not always occurred at maximum diameter.

Table 7. 2: Segmented Diameter Deformation Based on a) Vertical Axis; and b) Horizontal Axis

Vertical Segment (cm) (A-E point)					
	V1	V2	V3	V4	V5
<b>Patient1</b>	2.63	3.1	3.94	4.31	4.52
<b>Patient2</b>	2.56	2.98	4.94	5.34	5.34
<b>Patient3</b>	1.77	2.56	2.84	3.64	4.02
<b>Patient4</b>	2	2.79	4.48	4.57	4.66
<b>Patient5</b>	1.96	2.95	4.39	4.45	2.27
<b>Patient6</b>	1.73	3.06	4.94	4.54	2.61
<b>Patient7</b>	2.37	2.28	2.47	4.14	3.92
<b>Patient8</b>	2.28	2.64	2.37	4.66	5.27
<b>Patient9</b>	2.12	2.45	2.3	3.62	4.06
<b>Patient10</b>	2.22	2.58	4.31	4.34	4.51
<b>Patient11</b>	2.21	3.75	4.44	4.56	3.6
<b>Patient12</b>	2.52	2.81	2.62	3.44	3.86
<b>Patient13</b>	2.03	4.78	5.72	5.43	5.05

(a)

Horizontal Segment (cm) (C-E point)					
	H1	H2	H3	H4	H5
<b>Patient1</b>	3.52	3.24	4.37	4.51	4.38
<b>Patient2</b>	2.56	3.06	5	5.74	5.68
<b>Patient3</b>	1.78	2.5	2.98	3.56	4.19
<b>Patient4</b>	2.07	2.82	4.84	4.82	4.96
<b>Patient5</b>	2.19	4.01	4.6	4.5	2.45
<b>Patient6</b>	1.97	2.71	5.57	5.17	2.66
<b>Patient7</b>	2.86	2.39	2.7	4.23	4.24
<b>Patient8</b>	2.08	2.86	2.71	5.46	5.87
<b>Patient9</b>	2.6	3.15	2.74	3.62	4.03
<b>Patient10</b>	2.4	2.86	4.94	5.1	5.24
<b>Patient11</b>	2.38	4.14	5.02	5.02	4.24
<b>Patient12</b>	2.41	2.7	2.84	3.74	3.98
<b>Patient13</b>	1.86	4.66	8.15	8.33	5.45

(b)

### 7.3: Physical Parameter Analysis

This analysis as explained in Section 5.4.1, discusses the importance of parameters generated from simulation results according to the patient aneurysm modelling setup. These parameters are also derived from experimental data as discussed in Section 6.4.

#### 7.3.1: Strain Energy

In the computational method, we use numerical model results from simulation to obtain strain energy per unit time using ANSYS as discussed in Chapter 5. In experiments, the value has been calculated from failure specimens to observe the final ultimate load (in Chapter 6) before calculating the strain energy per unit time (using Equation 6-11) from the real specimen. The comparable model parameter is deliberately selected to correlate modelling results and real specimens based on diameter classifications produced in Table 7.2. This analysis leads to non-invasive observation of the rupture relativity factors from both methods.

In the specimen analysis, the position and dimensions were recorded during testing to determine the failure parameter of the samples. Based on the amount of displacement (true stress strain testing), the average strain energy calculated from all six specimens are 111.14 J. Since failure was defined as a complete tear of all tissues across the specimen wall, high stretch tissue may have taken more displacement before artery failure. As a result, the artery wall may have failed earlier than visualised (from high speed camera image discussed in Section 6.4). The evidence was unclear to support this speculation due to other factors such as tissue specimen holder during inflation testing. This may have increased the ultimate spot measurement and therefore the stretch proportion. Table 6.2 summarizes the diameter classification in Table 7.3 for normalising the diameter range in calculating empirical evidence based on modelling and experimental data as below:

- The PSAM (from US images) is classified as per specimen from experiments based on diameter size
- The energy required by specimens to rupture is averaged due to standard pressure loading rate.
- Energy per unit time ( $U_T$ ) is calculated based on tested specimen and generated computational model with diameter classification for comparison.

**Table 7. 3:** Patient Specific Diameter Range Classification

Cohort #	Diameter (cm)	In range excised specimen from Sugita experimental data	Average Energy per Unit Time ( $U_T$ )	Relative Patient data from Ultrasound Image	Average Ultimate Strength, UTS MPa	Total Energy to failure (J)
1	4.0-5.4	H104 (5.0) & H108(5.0)	0.41	P1,3,4,5,7, 9, 11& 12	0.96	76.64
2	5.5-6.4	H119 (6.2)	0.37	P2,6,8,10	1.15	140.75
3	6.5 above	H116 (6.5) & H123 (6.5)	0.49	P13	1.21	156.47

The combination parameters are incorporated in Section 7.4 to determine the correlation between parameter factors to rupture and diameter ranges from each PSAM. Table 7.3 could be used as US data assessment for aneurysm patients to determine the possible location, current thickness and time estimation based on strain energy results from the developed model. This calculation provides the time estimation to the rupture based on simulation results with respect to both incorporated methods.

### 7.3.2: Maximum Stress

The stress result from simulation has been generated to produce the maximum and minimum value of the stress that can be used to calculate the mean stress and alternating stress (Equation 5-2 and 5-3). These values are calculated to define the interrelation between the failures modes with the number of cycles generated based on pulsating blood flow (heart beat). The results of this stress help to measure the effect on the risk of AA rupture in term of number of cycles.

The mean stress and alternating stress are shown in the Table 7.4. From this table, we conducted the fatigue analysis in the next section based on the number of estimated cycles. The calculated stresses resulting from the reconstructed aneurysm model simulations were plotted to produce the endurance stress in the S-N curve in order to estimate the fatigue cycle for each patient model.

Table 7. 4: Mean Stress and Alternating Stress Results based on Aneurysm Model

Model	Maximum Stress (MPa)	Minimum Stress (MPa)	Mean Stress (MPa)	Alternating Stress (MPa)
<b>Patient 1</b>	0.097	0.002	0.049	0.047
<b>Patient 2</b>	0.097	0.008	0.048	0.038
<b>Patient 3</b>	0.077	0.041	0.059	0.018
<b>Patient 4</b>	0.11	0.007	0.055	0.055
<b>Patient 5</b>	0.094	0.0039	0.048	0.045
<b>Patient 6</b>	0.09	0.0013	0.045	0.044
<b>Patient 7</b>	0.116	0.0015	0.058	0.057
<b>Patient 8</b>	0.075	0.002	0.038	0.036
<b>Patient 9</b>	0.084	0.0062	0.042	0.041
<b>Patient 10</b>	0.1	0.0076	0.053	0.046
<b>Patient 11</b>	0.77	0.0062	0.041	0.035

#### 7.4: Comparison Study and Empirical Evidence

The comparison study must be influenced by the evidence or results. Thus it can be perceived by our rationalities and is derived from our observations and empirical data based on both observations and experiment results. In the process of accepting or disproving the hypothesis, the proofs with interpretation are derived to a conclusion on the basis of observation or experiment. To define this, the modelling data need to be multiplied by a certain factor to get the comparative actual experimental value. Parameter factors of both methods in different points of view are presented here.

This comparison study involves the diameter range that we classify for specimen origin (from the patient) and US patient modelling as shown in Table 7.5. This table presents the diameter range with allocated patient for both methods. ‘X’ is representing the tick for which the patient and specimen belong to that diameter range. P1 to P13 are patient aneurysm models which are reconstructed based on aneurysm patient US; and SP1 to SP6 are the excised specimens from patient aneurysm diameter. This intentionally presented to show the significant correlation between selected parameters (within the diameter range) from computational and experimental methods towards rupture.

**Table 7. 5:** Modelling-Experimental Parameter Analysis Diameter Classification

Diameter Range (cm)	Prediction Factor Comparison																		
	PSAM Model													Experiment					
	P 1	P 2	P 3	P 4	P 5	P 6	P 7	P 8	P 9	P 10	P 11	P 12	P 13	S P 1	S P 2	S P 3	S P 4	S P 5	S P 6
Below 4.0			X				X	X	X			X							
4.0-4.5	X				X					X	X								
4.5-5.0				X											X			X	
5.0-5.5						X							X						
5.5-6.0		X																	
6.0-6.5														X		X	X		X
6.5 above																			

Since a geometrical analysis has established the correlation between model strain deformation and location with other human factors as explained in Table 7.1, this physical parameter analysis achieves in tracking the same thing. A correlation has been established based on specimens and PSAM values from two variable parameters with respect to diameter range. Stress and strain energy parameters are interrelated with the diameter to determine more association between the model and the experimental approaches. Figure 7.4 shows the correlation between the specimen and model stress parameter values that has a similar linear trend line but is shifted in the vertical axis. Similar correlation results are obtained for strain

energy parameter in Figure 7.5 for all aneurysm diameters. In this graph, the log axis is chosen due to very small energy values generated by the model (1s pulse) compared to failure specimen energy (at UTS). This similar trend line reveals that these two parameters establish a good relationship in predicting the aneurysm rupture and has a very significant correlation.

These correlations lead to the investigation of the number of cycles from the computational model based on specimen failure modes for estimation. The exploration details are discussed in next fatigue analysis section.

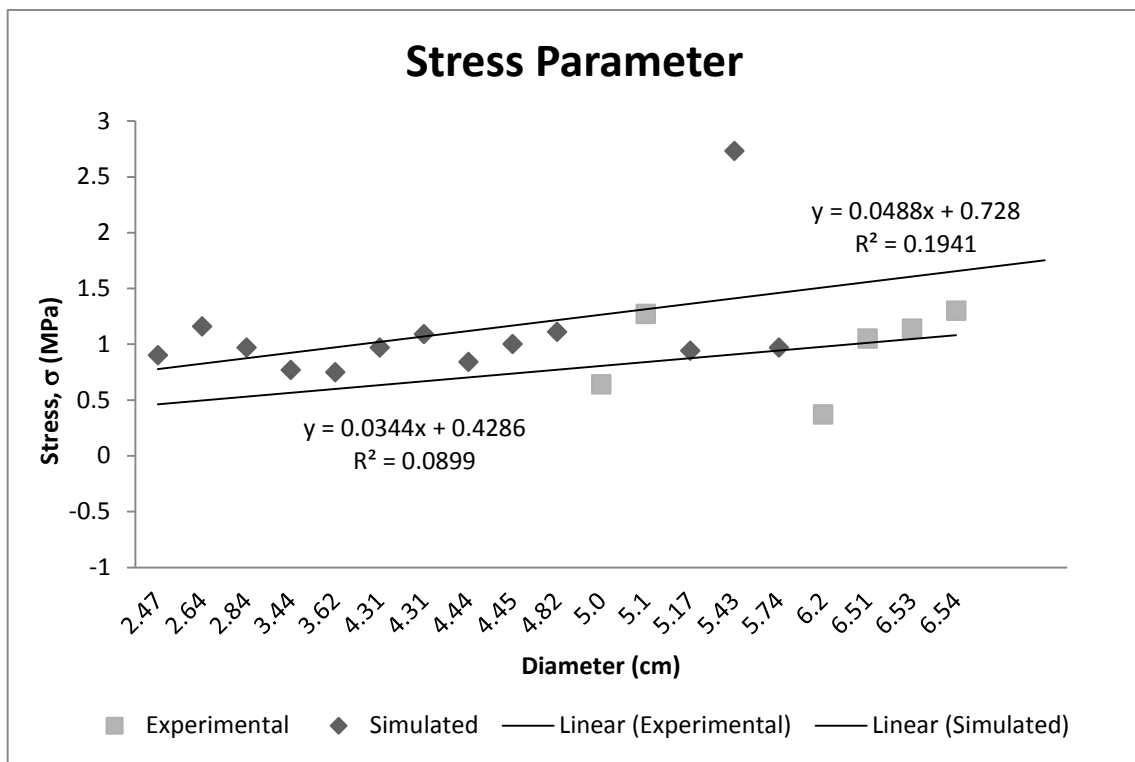


Figure 7. 4: Stress Parameter Correlation Graph

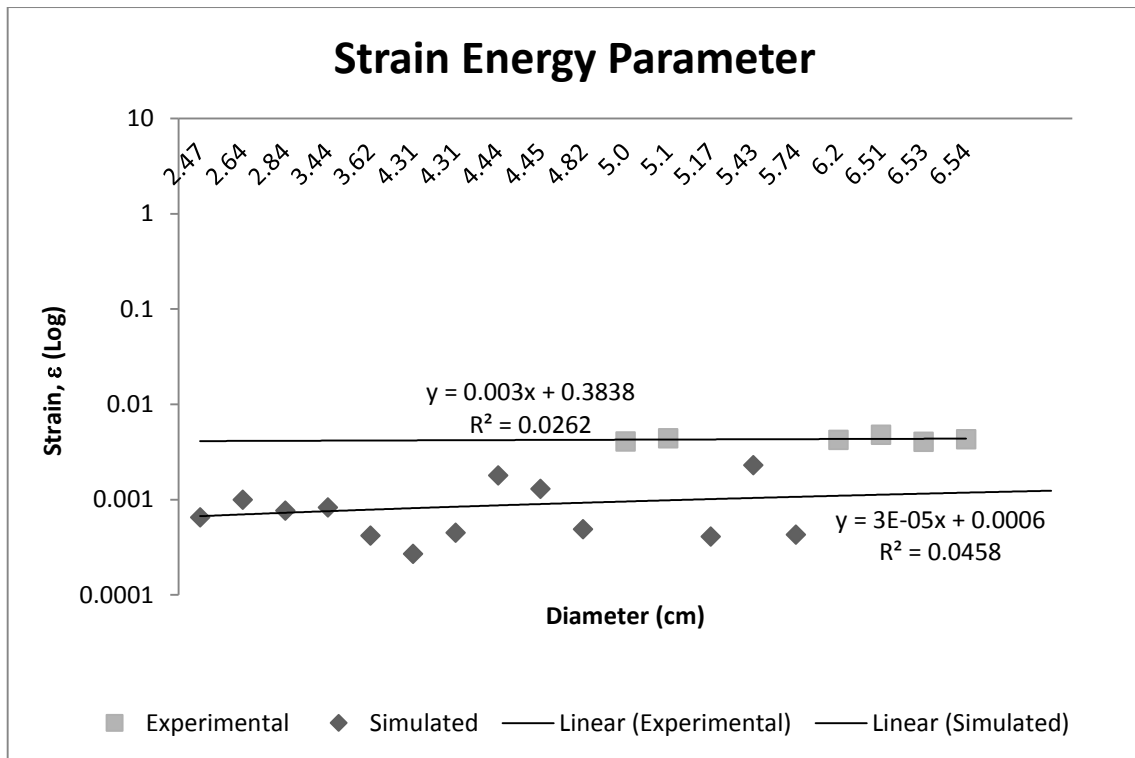


Figure 7. 5: Strain Energy Parameter Correlation Graph

### 7.5: Ultimate Failure Tissue Analysis

By taking into consideration that the rupture mode is calculated based on affected parameters during pressure loading for the detection of failure mechanisms, we analyse three parameters (stress, strain and energy). Based on the information collected from US images (diameter, thickness and loading) for constructing the PSAM, the consistency to account for aneurysm factors from the experimental part is feasible. Referring to large tissue deformation from [30] theory, developing novel practical models for a rupture aneurysm model has to rely on specific determinants as determined from real specimens. As opposed to contemporary models, these models are time dependent and can be used to determine the number of pulse cycles estimated from the weakest point to rupture. The simulated model could estimate the rupture time based on calculated strain energy rate as discussed in Section 6.4 as well as their specific location and the thickness.

### 7.5.1 Failure Tissue Formula

The results in Chapter 5 are investigated in more detail and incorporated with tissue failure analysis to derive a new formula for investigating the rupture instantaneously. This formulation takes into consideration all the studied parameters in Section 5.4 compared to calculated parameters discussed in Section 6.4.3. The comparison leads to the formulation of the rupture/failure from both methods using similar mechanisms with additional time estimated elements. The results from PSAMs show there are non-specific locations that have a higher tendency to rupture. Thus, increasing the high possibility that rupture may not rely on single criteria. By looking into maximum stress and maximum strain from every model there is correlation in terms of maximum location. In addition, we found that the result from maximum deformation (diameter) does not much associate with those parameters. This shows that maximum stress and maximum strain energy has significant stress values in determining the high potential of the rupture from the simulated models. From a mechanical perspective, the hemodynamic characteristics have stress impacts at any location on the elastic wall as long as the thickness and material properties were not considered.

### 7.6: Fatigue Tissue Analysis

Another way to reach physical damage or rupture of the materials is by cumulative fatigue cycles using the correlation between fatigue life of blood vessel wall and its deformation energy. This correlation theory was studied in determining the value of energy relation on experimental testing value relationship [159] which was later validated by the theory of failure under cyclic loading and the existence of critical energy [160]. These studies lead to findings on the accumulation of hysteresis energy during fatigue, and the strain energy accumulation on damage model done by [161, 162].

### 7.6.1: Fatigue Formula

From this fatigue tissue theory, we study the pressure versus endurance curve that can be engaged from PSAM model for maximum and minimum limit strength with varying wall ratios as proposed by [76]. Taking into consideration the strain energy accumulation for interrupted loading cycle could lead to validate energy-based fatigue life prediction of the tissue. This prediction provides understanding the roles of the strain energy rate accumulated during failure specimen during the testing. Here, we calculate the optimum value of tissues strength from experimental testing to formulate a fatigue tissue formula using stresses values. The mean and alternating stress values are calculated from the generated model (Table 7.4) in determining the endurance stresses as explained in next section.

### 7.6.2: Stress Life Cycle (S-N curve) Analysis

Due to the variability of biological tissue, the stress correlation coefficient (as discussed in Section 6.2) does not indicate very strong relationship for high elasticity tissue. However, the test performed on aneurysm tissues indicates that the material was exhibiting no fatigue damage accumulation. S-N curve was obtained based on tissues cyclic loading below ultimate strength of the material. The tested magnitude was set below the constant cyclic load according to ultimate strength to determine the materials final stress. Other factors that may affect the stress calculation are also considered.

The factors that affect the stress life cycle calculation is observed to determine the specific location and the specimens that are cycled to failure at higher stresses than the ultimate strength had higher stretch ratios than the nearby specimen. This validates the rupture specimen failure that does not always occurred at maximum diameter as discussed earlier in this chapter. This

large ratio is due to a larger amount of stretch experienced by the circumference or close location to maximum deformation (as discussed in Section 6.2), that increases the stress value. The accumulation of damage shown by histology indicates that fatigue damage is accumulating and the positive slope of the time vs. position curve indicates the material failure [123]. The correlation between the loaded maximum stresses, strain energy and the number of cycles to failure permits us to estimate the cycles to Failure. Thus, the fatigue failure point of soft tissue can be predicted.

We plotted the S-N curve according to reconstructed fatigue graph (referring to Fig 6.6a) to determine the endurance stress for each PSAM model. Using maximum and minimum stresses from Table 7.3, the linear line is plotted as illustrated in Figure 7.6. Here, the classification of the diameter range specimens and the models are important to be differentiated between failure strength (UTS) of the tissues. Hence, an individual line is plotted before the number of cycle is determined as shown in Figure 7.7 as explained in Section 6.5.3.

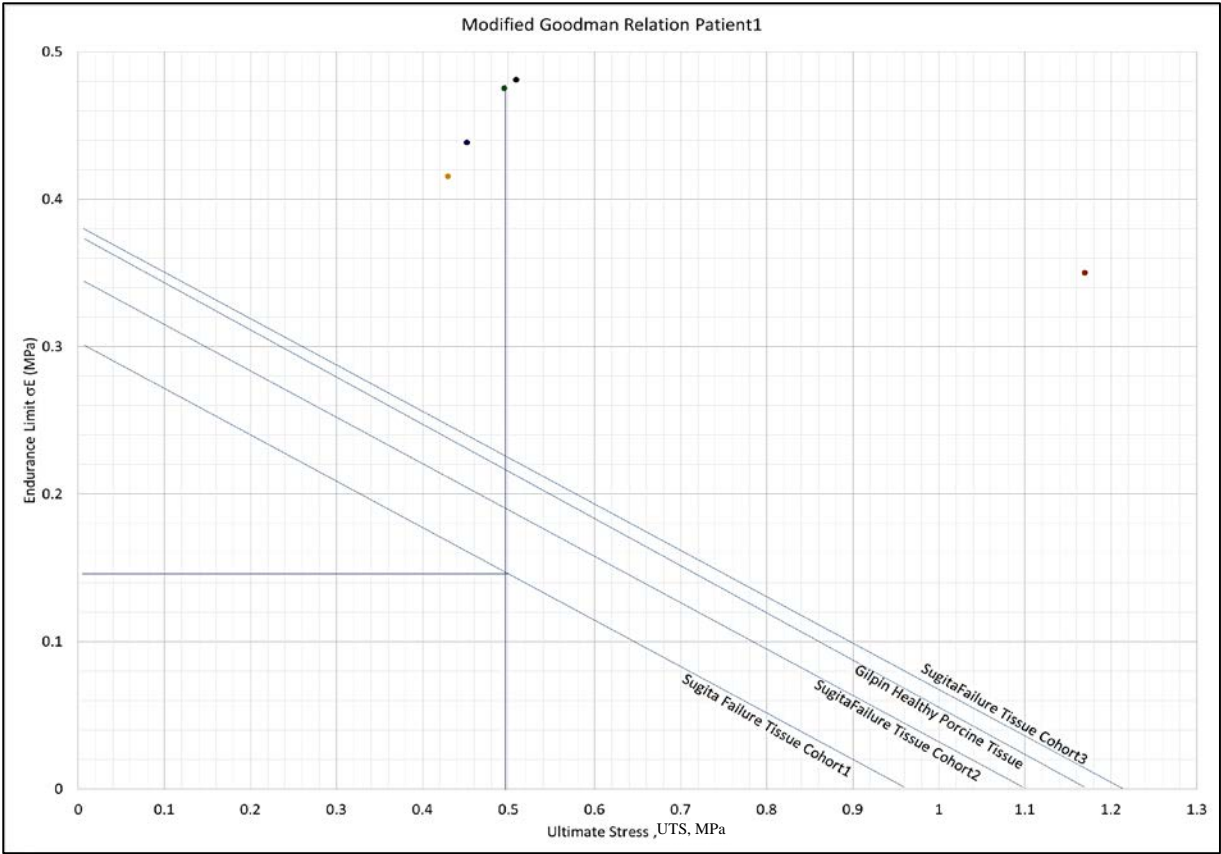


Figure 7. 6: Goodman Relation for PSAM-Failure Group Specimen

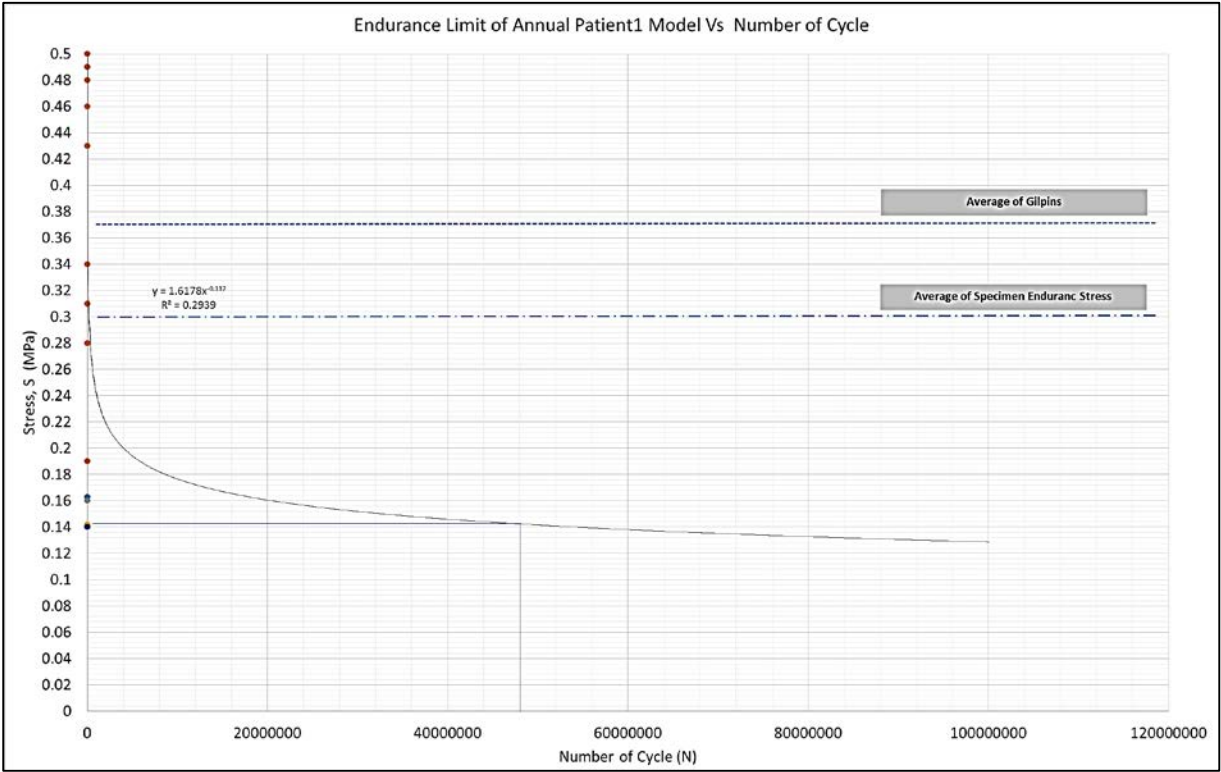


Figure 7. 7: Number of Cycle for PSAM-Failure Group Specimen

## 7.7: Aneurysm Progress Validation

Annual progresses of the AAA patient aneurysm were reconstructed based on the available database from the Manukau Super Clinic (CMDHB). The measurement of the model is according to the progressing history of the patient aneurysm which has been recorded into the CMDHB database. All the available parameters were taken into account for model reconstruction including estimated geometry, pressure and the thickness of the wall (Appendix C). The approach is basically different compared to the P-SARP protocol applied for normal remodelling as in Chapter 4 due to limited access to the US images.

The validations are discussed according to different approaches which are based on the available parameters significant to the method of the research proposed in previous sections. The progress of the segments particularly with high suspected effect is monitored based on the period of a year's information recorded for further validation (Appendix D). The time period between data collected is calculated for comparison studies for the S-N curve later in the next section. The yearly progressing model is considered based on the highest impact of maximum stress (Appendix C: B1), strain energy (Appendix C: B2), strain deformation (Appendix C: B3) and their location as discussed previously in Chapter 5. However, to generate the annual mean and alternating stress from the model, the progressing model is reconstructed using the P-SARP protocol according to the data summarized in Table 7.6.

Table 7. 6: Annual Aneurysm Progress Database

	Data Collection Date				Delta Time (days)		
<b>Patient1</b>	13/05/2011	7/08/2012	14/03/2013	21/01/2014	452	219	313
<b>Patient2</b>	22/10/2009	20/09/2011	31/08/2012	14/03/2013	698	346	195
<b>Patient3</b>	24/01/2012	14/03/2013	10/09/2013	27/03/2014	415	180	198
<b>Patient4</b>	29/06/2011	8/08/2012	14/03/2013	28/08/2013	406	218	167
<b>Patient5</b>	20/12/2011	4/09/2012	19/04/2013	15/10/2013	259	227	179
<b>Patient6</b>	18/11/2011	6/07/2012	19/04/2013	21/01/2014	231	287	277
<b>Patient7</b>	2/11/2010	12/12/2011	19/04/2013	20/03/2014	405	494	335
<b>Patient8</b>	14/12/2010	26/07/2011	9/05/2012	27/06/2013	224	288	414
<b>Patient9</b>	18/03/2011	27/09/2011	26/01/2012	27/06/2013	193	121	518
<b>Patient10</b>	22/09/2009	9/12/2010	7/02/2011	27/06/2013	443	60	871
<b>Patient11</b>	4/08/2011	1/11/2012	15/08/2013	19/03/2014	455	287	216
<b>Patient12</b>	25/05/2011	27/06/2012	15/08/2013	16/04/2014	399	414	244
<b>Patient13</b>	14/08/2012	15/08/2013	4/03/2014	14/08/2012	366	201	567

#### 7.7.1: Annual Validation Methods

A variety of methods in defining failure analysis are normally used for metal that can be replicated in this tissue failure such as the Goodman Relation. Using limited available US imaging parameters, good information to be organized from aneurysm model simulations have been produced. Three observed parameters as discussed in previous chapters offer options for tissue rupture and the number of cycles to be further investigated. In this section we discuss a few failure methods to calculate rupture based on our computational result incorporated with failure of tissue specimens. Aneurysm progress is individually tracked using the Goodman Relation method which can be used to determine the ultimate stress and endurance limit. Based on annual stresses occurring from modelling results (Table 7.6), the endurance stress is plotted on the Goodman Relation graph and S-N curve as shown in Figure 7.8 and Figure 7.9, respectively. All the data was recorded and summarized in Table 7.7.

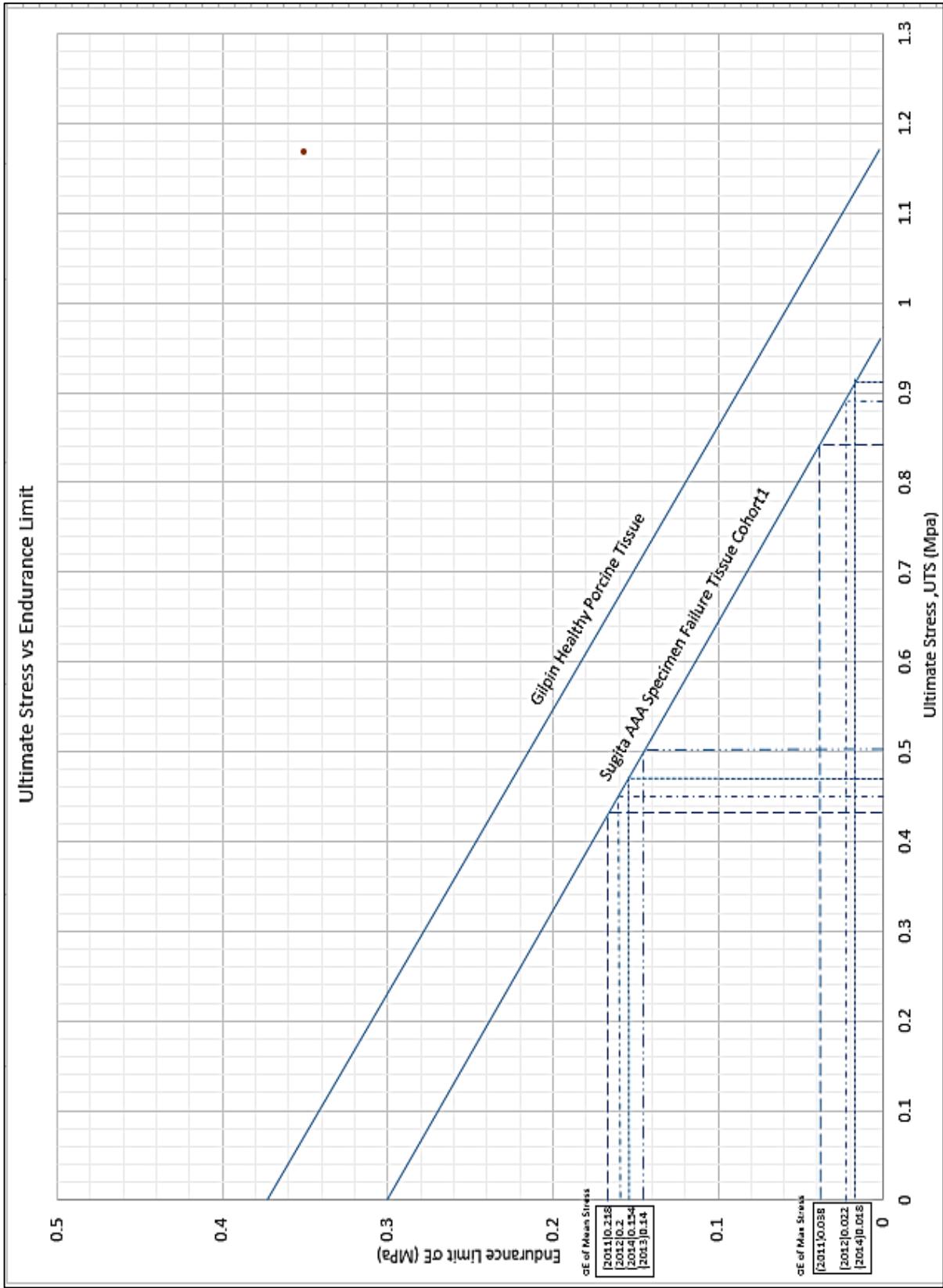


Figure 7. 8: Goodman Relation based on Aneurysm Progressing Years

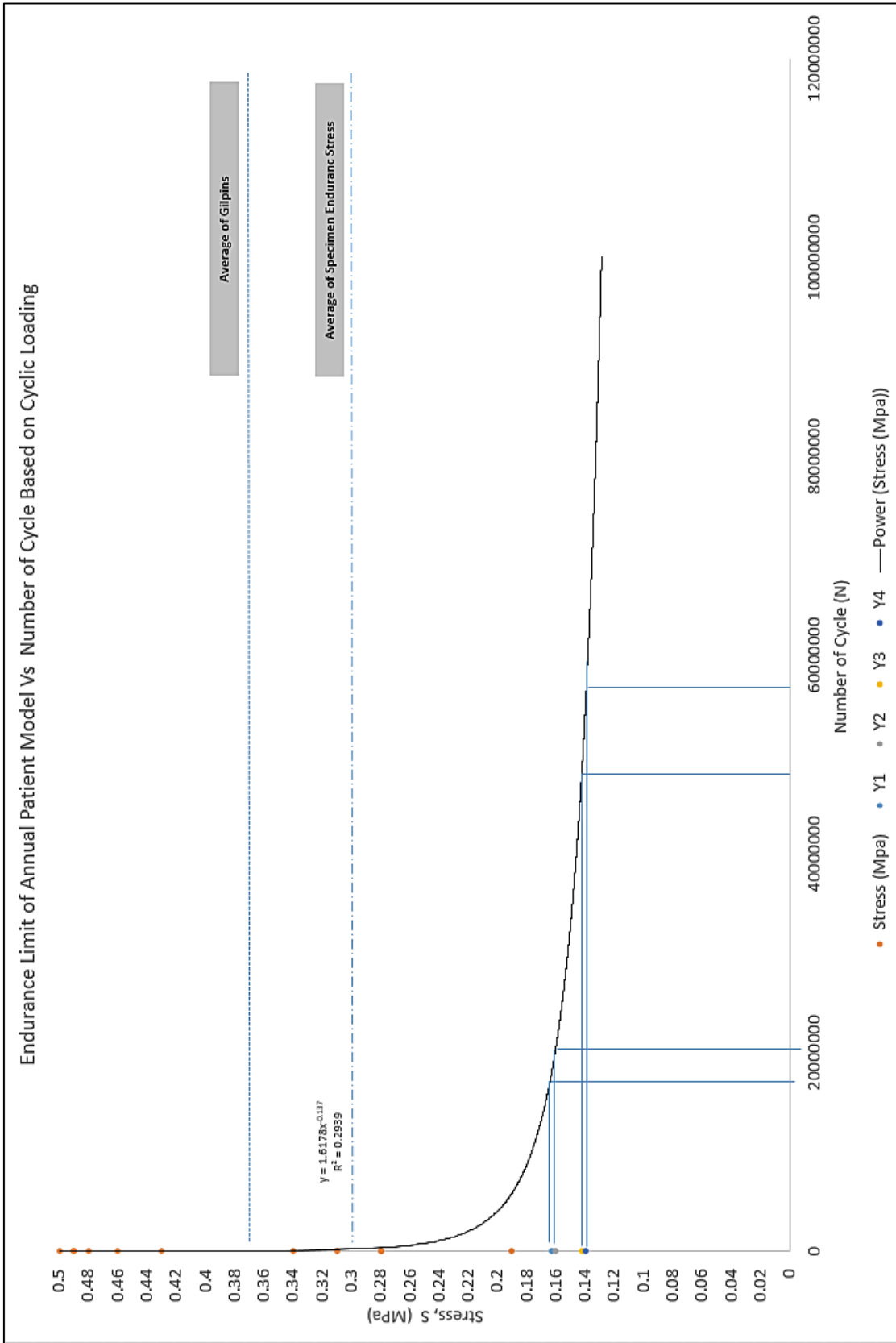


Figure 7. 9: Number of Cycle based on Aneurysm Progressing Years

The modified Goodman range-of-stress illustrated in Figure 7.10 (which is also used as a failure locus) is used to ensure that all endurance stress amplitude values are within the region. Refer to Appendix E. This range estimates the rupture at cycle N and more cycles without failure if the stress amplitude value touches the locus and lies near the locus, respectively. However, if any stress amplitude that exceeds the bound of the locus, the failure is estimated fewer than N cycles.

Table 7. 7: Endurance Stress from Annual Aneurysm Progress

Patient	Endurance Stress from Goodman			
	Y1	Y2	Y3	Y4
P1	0.163	0.16	0.142	0.14
P2	0.196	0.21	0.193	0.191
P3	0.112	0.119	0.116	0.155
P4	0.12	0.119	0.121	0.115
P5	0.21	0.2	0.192	0.18
P6	0.14	0.202	0.155	0.206
P7	0.16	0.208	0.2	0.164
P8	0.164	0.145	0.16	0.18
P9	0.23	0.198	0.207	0.218
P10	0.16	0.155	0.133	0.13
P11	0.186	0.175	0.17	0.164

The number of cycles which is considered to base on heart beat pulses and all the values have to rely on it for this forecasting. We estimated that if this tissue fatigue can be calculated on real tissue, the number of cycles from each endurance stress to reach rupture is possible to calculate within three years of aneurysm annual progress. However, due to no availability data from human tissue, we estimate the number of cycles based on the S-N plot approximation range as recorded in Figure 7.9.

Modified Goodman Range of Stress Diagram

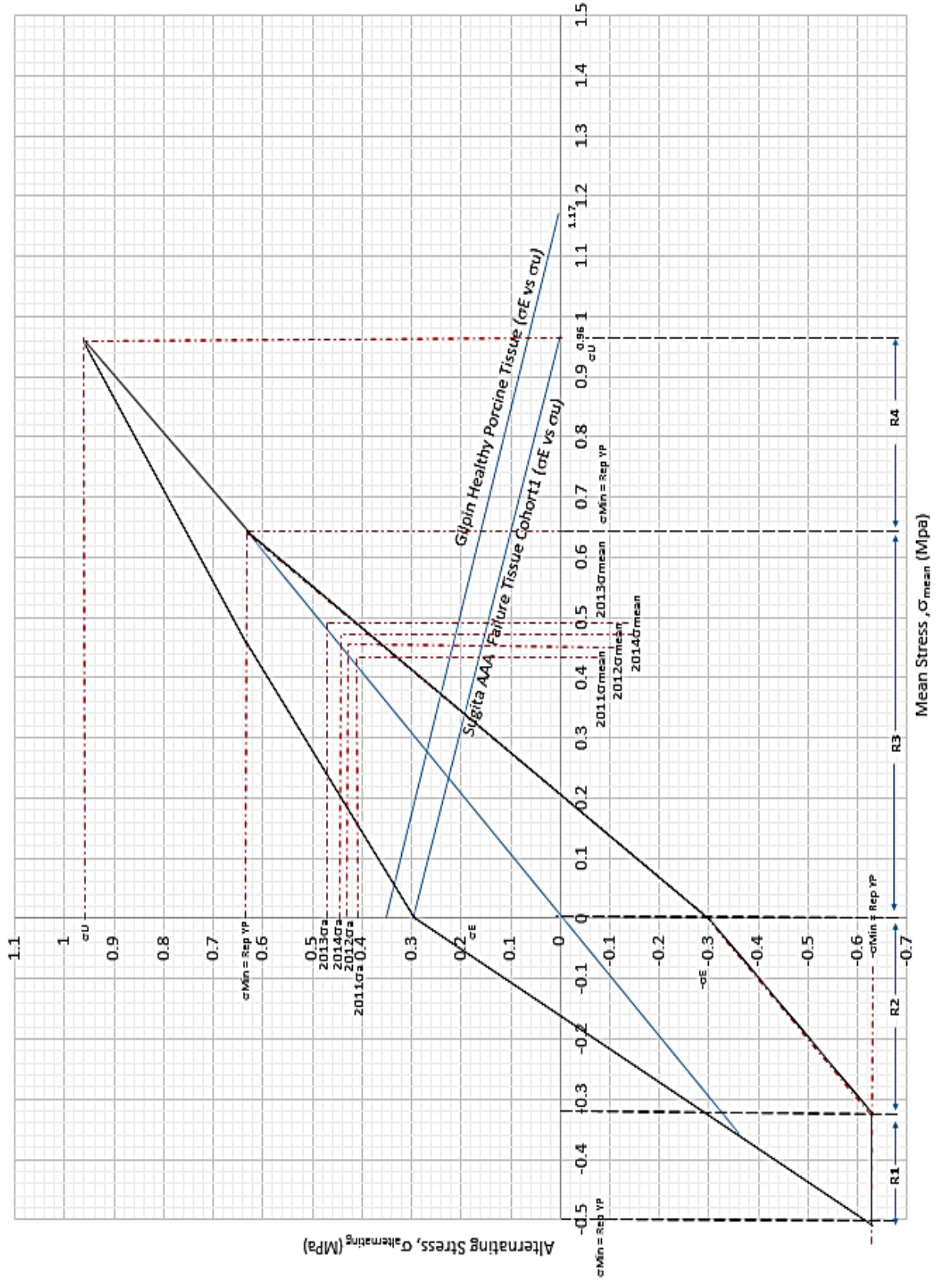


Figure 7. 10: Goodman Stress Range

## 7.8: Summary

Computational simulation and modelling provides the means to estimate and quantify tissue biomechanical factors which have the potential to contribute more effectively on tissue rupture analysis. The mechanical rupture is the structural tissue failure strength of the constructed wall and by performing tissues biomechanics modelling offers a better estimation on the risks of wall rupture due to aneurysm. Different selection from diverse parameters of the patient-specific material characteristics might lead to an improvement in aneurysm-related mortality rates.

The main objectives of this thesis are to develop an understanding of how aneurysms are predicted. Also how we can use various theories to help us in predicting the aneurysm wall precisely in the method which is better than current method which is only rely on the diameter. The study met all the critical objectives set at the beginning as it has been accomplished to do proper model that correlate well the experimental data. It also shows good correlation with multiplier factor of parameters over the model to safely predict the actual outcome based on the comparison between the modelling verses experimental data.

This research has achieved the following objectives by:

- Obtaining US data from 13 AAA patient assessments which has been conducted at Manukau Super Clinic using the proposed P-SARP protocol in Chapter 4.
- Developing the model based on the data which has been determined to generate the aneurysm model result from simulation as discussed in Chapter 5.
- From the results obtained, the location of critical variables such as maximum stress, strain and energy has been determined and discussed in Chapter 6.
- The critical rupture parameters were further justified according to the failure hypotheses and been analysed and investigated in Chapter 7.

## 7.9: Conclusion

This research aim is to investigate aneurysm prediction for AAA. All of the contribution possibilities related towards its failure non-invasively were analysed in order to investigate rupture mechanism and discussed. In this research the theory of fatigue and failure ideas are caused by the gradual accumulation of small amounts of irrecoverable energy that has been initiated by several authors [161] who reviewed the situation and proposed an energy criterion for the failure. By applying the basic idea of hysteresis in dynamic loading and unloading, a certain amount of energy is retained in the material as hysteresis energy and here, the stored energy is in relatively small amounts per cycle. Since this energy is irrecoverable, it accumulates within the material. Whenever the amount accumulated reaches the amount necessary for rupture to occur, the material fails. This situation mirrors the situation of an aneurysm patient whose aortic blood vessel wall is being continuously loaded by the straining effect from instant blood vessel cyclic loading.

The theory of the rupture proposed in this research was compared to the multidimensional US modelling that has been segmented from proposed technique to investigate aneurysm rupture prediction. Precise parameters are taken into consideration for model reconstruction using ANSYS. Based on comparison from modelling and experimental results, we conclude that the rupture predictor is feasibly contributed by three elements obtained from computational model. Thus, it could help us to understand the risk of the failure increase significantly according to the parameters changes.

## 7.10: Future Work

The findings from the current research could establish further investigation on predicting aneurysm rupture instantaneously by integrating advanced technology. This could lead to the development of aneurysm smart models that could have more influence on the advanced parameter effect towards rupture prediction. It could be carried out in new research areas in different levels of study that will explore other dimensions to extending performance, scope and application from this research.

### 7.10.1: Integrated Aneurysm Assessment Method for Screening, Processing and Prediction Improvement

In US aneurysm assessing process, the proposed method of screening can be incorporated with advance system for better visuals, screening process and also prediction such as Artificial Intelligence (AI) system. Within this system, our proposed research method could be suggested to employ with;

1. Integrated scanning with 3D digitizing Image Capture tools (Digitizing)

This high accuracy digitizing image system provides faster, precise and accurate images from their resources including US. By implementing this into this method, there is no need to manually capture US images during screening and assessment. This technique could be performed by the same vascular nurse if this system is integrated into the US device which has been proved to be able to determine the specific aneurysm rupture parameter contributor.

2. Integration of Visual Analytics System (VA) using Accelerated Computing Method High Performance Computing (HPC)

This system is an automatic recognition of image capturing from the abovementioned point. It could be analysed to determine specific characteristic for next stage processing such as proposing boundary conditions, smoothing surfaces in modelling and suggesting the aneurysm shape formation. In addition, further research can be developed to determine the optimum parameters that could be assessed from aneurysm deformation and rupture.

3. Parallel Computing Using General Purpose Graphic Processing Unit (GPGPU)

This GPU-accelerated computing is the use of a graphics processing unit (GPU) together with a CPU to accelerate scientific, analytics, engineering, consumer, and enterprise applications [163]. Using this high speed graphic processing unit helps to improve the image precision determination when screening the US image as suggested in number 2. It will be beneficial to explore further on how GPU accelerator could process the images precisely and accurately before migrating into the model.

4. Intelligent Processing Algorithms for Prediction and Decision Support System (DSS)

This DSS is a management tool to help in making decisions, which may be quickly exchanging the selected parameter in advance (Unstructured and Semi-Structured decision problems). This DSS system develops specific algorithm and image correctness automatically. By integrating this algorithm, built model can do automatic

self-correction of the geometry precision based on affected region that can reduce the time consumption in reconstructing aneurysm model.

#### 7.10.2: Instantaneous AAA modelling reconstruction

This modelling reconstruction is suggested be improved in automatic precision in the future since the aneurysm modelling is a complex geometry. Using a new technique that could reduce the time consumption is an advantage. Auto model generation for reconstructing new 3D model and an automatic verification matching system could become a powerful tools in assessing and screening aneurysm formation and progress.

## REFERENCES

1. Kleinstreuer, C., Z. Li, and M.A. Farber, *Fluid-structure interaction analyses of stented abdominal aortic aneurysms*. Annual review of biomedical engineering, 2007. **9**: p. 169-204.
2. Wikipedia. [http://en.wikipedia.org/wiki/File:Circulatory\\_System\\_en.svg](http://en.wikipedia.org/wiki/File:Circulatory_System_en.svg).
3. S., M., *Cardiovascular assessment and management in developing countries*. Vascular Health and Risk Management, 2005. **1**(1): p. 15-18.
4. The National Heart Foundation of New Zealand, *Reducing your risk of heart attack and stroke*. 2004, Auckland: The National Heart Foundation of New Zealand;.
5. M.J., M. and A. C., *Structure and function small arteries*. Physiological Reviews, 1990. **70**(4).
6. Kantonen, I., et al., *Mortality in ruptured Abdominal Aortic Aneurysms*. European Journal Vascular Endovascular Surgery, 1998(17): p. 208-212.
7. Rose, J., et al., *Ruptured Abdominal Aortic Aneurysms: Clinical presentation in Auckland 1993-1997*. Australia New Zealand J. Surg, 2001(71): p. 341-344.
8. Greenwald, S.E., *Ageing of the conduit arteries*. The Journal of pathology, 2007. **211**(2): p. 157-72.
9. Radvany M. G. and Cho K. J. *Abdominal Aortic Aneurysm Imaging*. Medscape Reference, Radiography Overview 2008 October 2; Available from: <http://emedicine.medscape.com/article/416266-overview>.
10. Lasheras, J.C., *The Biomechanics of Arterial Aneurysms*. Annual Review of Fluid Mechanics, 2007. **39**(1): p. 293-319.
11. Fillinger, M.F. and R.A. Schwartz, *Volumetric blood flow measurement with color Doppler ultrasonography: the importance of visual clues*. J. Ultrasound Med, 1993. **12**: p. 123-130.
12. Lally, C., F. Dolan, and P.J. Prendergast, *Cardiovascular stent design and vessel stresses: a finite element analysis*. Journal of Biomechanics, 2005. **38**(8): p. 1574-81.
13. Holzapfel, G.A., *Biomechanics of Soft Tissue*, in *Computational Biomechanics*, J. Lemaitre, Editor. 2000: Graz, Austria.
14. G.A.Holzapfel, T.C.Gasser, and R.W.Ogden., *A new constitutive framework for arterial wall mechanics and a comparative study of material models*. November 2000: Graz, Austria.
15. Gasser, T.C. and G.A. Holzapfel, *A rate-independent elastoplastic constitutive model for biological fiber-reinforced composites at finite strains: continuum basis, algorithmic formulation and finite element implementation*. Computational Mechanics, 2002. **29**(4-5): p. 340-360.
16. Raghavan M.L and D.A. Vorp, *Toward a biomechanical tool to evaluate rupture potential of abdominal aortic aneurysm - identification of a finite strain constitutive model and evaluation its applicability*. Journal Biomechanics, 2000. **33**: p. 475-482.
17. Karamanoglu, M., et al., *Functional origin of reflected pressure waves in a multibranched model of the human arterial systems*. American Journal of Physiology, 1994. **267**: p. H1681-H1688.
18. Karamanoglu, M., et al., *An analysis of the relationship between central aortic and peripheral upper limb pressure waves in man*. European Heart Journal, 1993. **14**: p. 160-167.
19. Sandiford, P., D. Mosquera, and D. Bramley, *Trends in incidence and mortality from abdominal aortic aneurysm in New Zealand*. The British journal of surgery, 2011. **98**(5): p. 645-51.
20. Doyle, B., et al., *A Finite Element Analysis Rupture Index (FEARI) assessment of electively repaired and symptomatic/ruptured Abdominal Aortic Aneurysm*. WCB 2010, IFMBE Proceeding, 2010(31): p. 883-886.
21. Vande Geest, J.P., et al., *A biomechanics-based rupture potential index for abdominal aortic aneurysm risk assessment: demonstrative application*. Annals of the New York Academy of Sciences, 2006. **1085**: p. 11-21.
22. Maier, A., et al., *A comparison of diameter, wall stress, and rupture potential index for abdominal aortic aneurysm rupture risk prediction*. Annals of Biomedical Engineering, 2010. **38**(10): p. 3124-34.
23. Kleinstreuer, C. and Z. Li, *Analysis and computer program for rupture-risk prediction of abdominal aortic aneurysms*. Biomed Eng Online, 2006. **5**: p. 19.
24. Fillinger, M.F., et al., *Prediction of rupture risk in abdominal aortic aneurysm during observation: wall stress versus diameter*. Journal of vascular surgery : official publication, the Society for Vascular Surgery [and] International Society for Cardiovascular Surgery, North American Chapter, 2003. **37**(4): p. 724-32.
25. Ahlgren A. R., et al., *Stiffness and diameter of the common carotid artery and AAA in women*. Ultrasound in Medical and Biology, 1997. **23**(7): p. 983-988.
26. B. Sonesson, T. Sandgren, and T. Lanne, *Abdominal Aortic Aneurysm wall mechanics and their relation to risk of rupture*. European Journal Vascular Endovascular Surgery, 1999. **18**: p. 487-493.

27. Martufi, G., et al., *Multidimensional growth measurements of abdominal aortic aneurysms*. Journal of Vascular Surgery, 2013.
28. Martufi, G., et al., *Three-Dimensional Geometrical Characterization of Abdominal Aortic Aneurysms: Image-Based Wall Thickness Distribution*. Journal of Biomechanical Engineering, 2009. **131**.
29. Wolters, B.J., et al., *A patient-specific computational model of fluid-structure interaction in abdominal aortic aneurysms*. Medical Engineering & Physics, 2005. **27**(10): p. 871-83.
30. Fung, Y.C., *Biomechanics: Mechanical Properties of Living Tissues*. 2nd Edition ed. 1993, La Jolla, California: Springer- Verlag New York Inc.
31. Vorp, D.A. and J.P. van de Geest, *Biomechanical determinants of abdominal aortic aneurysm rupture*. Arteriosclerosis, Thrombosis and Vascular Biology, 2005. **25**: p. 1558-1566.
32. Rentschler M. E. and Baxter B. T., *Screening aortic drug treatments through arterial compliance measurements*. Vascular Pharmacology, 2008. **6**: p. 250-257.
33. Hasegawa, H. and H. Kanai, *Measurement of nonlinear property of artery wall using remote cyclic actuation*. Journal of Medical Ultrasonics, 2006. **33**(3): p. 143-151.
34. M. M. Stringfellow, P. Lawrence, and R.G. Stringfellow, *The influence of Aorta-Aneurysm geometry*. Journal of Surgical Research, 1986. **42**: p. 425-433.
35. Li, Z.Y., et al., *Association between aneurysm shoulder stress and abdominal aortic aneurysm expansion: a longitudinal follow-up study*. Circulation, 2010. **122**(18): p. 1815-22.
36. Bluestein, D., et al., *Intraluminal thrombus and risk of rupture in patient specific abdominal aortic aneurysm - FSI modelling*. Computer Methods in Biomechanics and Biomedical Engineering, 2009. **12**(1): p. 73-81.
37. Stenbaek, J., B. Kalin, and J. Swedenborg, *Growth of thrombus may be a better predictor of rupture than diameter in patients with abdominal aortic aneurysms*. European journal of vascular and endovascular surgery : the official journal of the European Society for Vascular Surgery, 2000. **20**(5): p. 466-9.
38. Khir, A., *Local and regional wave speed in the aorta: effects of arterial occlusion*. Medical Engineering & Physics, 2004. **26**(1): p. 23-29.
39. Madhukar S. Patel, David A. Brown, and S.E. Wilson, *Relevance of the ADAM and UK small aneurysm trial data in the age of endovascular aneurysm repair*. Archives of Surgery, 2009. **144**(9).
40. Thubrikar, M.J., M. Labrosse, and F.R. M., *Mechanical properties of abdominal aortic aneurysm wall*. Journal of Medical Engineering & Technology, 2001. **25**(4): p. 133-142.
41. Vorp, D.A., M.L. Raghavan, and M.W. Webster, *Mechanical wall stress in abdominal aortic aneurysm: influence of diameter and asymmetry*. J Vasc Surg, 1998. **27**(4): p. 632-9.
42. Raghavan, M.L., et al., *Wall stress distribution on three-dimensionally reconstructed models of human abdominal aortic aneurysm*. Journal of vascular surgery : official publication, the Society for Vascular Surgery [and] International Society for Cardiovascular Surgery, North American Chapter, 2000. **31**(4): p. 760-9.
43. Hua, J. and W.R. Mower, *Simple geometric characteristics fail to reliably predict abdominal aortic aneurysm wall stresses*. Journal of vascular surgery : official publication, the Society for Vascular Surgery [and] International Society for Cardiovascular Surgery, North American Chapter, 2001. **34**(2): p. 308-15.
44. Biasetti, J., F. Hussain, and T.C. Gasser, *Blood flow and coherent vortices in the normal and aneurysmatic aortas: a fluid dynamical approach to intra-luminal thrombus formation*. Journal of the Royal Society, Interface / the Royal Society, 2011.
45. Gasser, T.C., et al., *Biomechanical Rupture Risk Assessment of Abdominal Aortic Aneurysms: Model Complexity versus Predictability of Finite Element Simulations*. European Journal of Vascular and Endovascular Surgery, 2010. **40**(2): p. 176-185.
46. Gasser, T.C., et al., *Failure properties of intraluminal thrombus in abdominal aortic aneurysm under static and pulsating mechanical loads*. Journal of vascular surgery : official publication, the Society for Vascular Surgery [and] International Society for Cardiovascular Surgery, North American Chapter, 2008. **48**(1): p. 179-88.
47. Tong, J., et al., *Effects of Age on the Elastic Properties of the Intraluminal Thrombus and the Thrombus-covered Wall in Abdominal Aortic Aneurysms: Biaxial Extension Behaviour and Material Modelling*. European journal of vascular and endovascular surgery : the official journal of the European Society for Vascular Surgery, 2011.
48. Vande Geest, J.P., et al., *Towards a noninvasive method for determination of patient-specific wall strength distribution in abdominal aortic aneurysms*. Annals of Biomedical Engineering, 2006. **34**(7): p. 1098-106.
49. Wang, D., et al., *Effect of intraluminal thrombus on wall stress in patient-specific models of abdominal aortic aneurysm* ☆. Journal of Vascular Surgery, 2002. **36**(3): p. 598-604.
50. Myers K, et al., *Endoluminal Versus Open Repair for Abdominal Aortic Aneurysms*. 2001.

51. Faggioli G. L, et al., *Morphology of small aneurysm: Definition and impact on risk of rupture*. The American Journal of Surgery, 1994. **168**: p. 131-135.
52. Limet, R., N. Sakalihassan, and A. Albert, *Determination of the expansion rate and incidence of rupture of Abdominal Aortic Aneurysm*. Journal of Vascular Surgery, 1991. **14**(4): p. 540-548.
53. Powell, J.T., et al., *Rupture rates of small abdominal aortic aneurysms: a systematic review of the literature*. European journal of vascular and endovascular surgery : the official journal of the European Society for Vascular Surgery, 2011. **41**(1): p. 2-10.
54. Urbonavicius, S., et al., *Potential circulating biomarkers for abdominal aortic aneurysm expansion and rupture--a systematic review*. European journal of vascular and endovascular surgery : the official journal of the European Society for Vascular Surgery, 2008. **36**(3): p. 273-80; discussion 281-2.
55. L. H. Peterson, R. E. Jensen, and J. Parnell, *Mechanical Properties of Arteries in Vivo*. Journal the American Heart Association, 1960. **8**: p. 622-639.
56. Wolf YG, et al., *Computed tomography scanning findings associated with rapid expansion of abdominal aortic aneurysms*. Journal Vascular Surgery, 1994. **20**(5): p. 29-38.
57. Beller, C.J., et al., *Increased aortic wall stress in aortic insufficiency: clinical data and computer model*. European journal of cardio-thoracic surgery : official journal of the European Association for Cardio-thoracic Surgery, 2005. **27**(2): p. 270-5.
58. Fillinger, M., et al., *In vivo analysis of mechanical wall stress and abdominal aortic aneurysm rupture risk* ☆. Journal of Vascular Surgery, 2002. **36**(3): p. 589-597.
59. Gasser, T.C., et al., *Biomechanical rupture risk assessment of abdominal aortic aneurysms: model complexity versus predictability of finite element simulations*. European journal of vascular and endovascular surgery : the official journal of the European Society for Vascular Surgery, 2010. **40**(2): p. 176-85.
60. Georgakarakos, E., et al., *Peak wall stress does not necessarily predict the location of rupture in abdominal aortic aneurysms*. European journal of vascular and endovascular surgery : the official journal of the European Society for Vascular Surgery, 2010. **39**(3): p. 302-4.
61. Helderman, F., et al., *A numerical model to predict abdominal aortic aneurysm expansion based on local wall stress and stiffness*. Medical & biological engineering & computing, 2008. **46**(11): p. 1121-7.
62. Thubrikar, M.J., J. al-Soudi, and F. Robicsek, *Wall stress studies of abdominal aortic aneurysm in a clinical model*. Annals of vascular surgery, 2001. **15**(3): p. 355-66.
63. Vorp, D.A., M. Raghavan, and M.W. Webster, *Mechanical wall stress in Abdominal Aortic Aneurysm: Influence of diameter and asymmetry*. 1998.
64. Vorp, D.A. and J.P. Vande Geest, *Biomechanical determinants of abdominal aortic aneurysm rupture*. Arteriosclerosis, thrombosis, and vascular biology, 2005. **25**(8): p. 1558-66.
65. Venkatasubramaniam, A.K., et al., *A comparative study of aortic wall stress using finite element analysis for ruptured and non-ruptured abdominal aortic aneurysms*. European journal of vascular and endovascular surgery : the official journal of the European Society for Vascular Surgery, 2004. **28**(2): p. 168-76.
66. Raghavan, M.L., et al., *Regional distribution of wall thickness and failure properties of human abdominal aortic aneurysm*. Journal of Biomechanics, 2006. **39**(16): p. 3010-6.
67. Yoo, L., et al., *Quasilinear viscoelastic behavior of bovine extraocular muscle tissue*. Investigative ophthalmology & visual science, 2009. **50**(8): p. 3721-8.
68. Young, W.C. and R.G. Budynas, *Roark's Formula for Stress and Strain*. 7 ed. General Engineering Series, ed. M.-H.I. Edition. 2002, Singapore: McGraw-Hill Education (Asia).
69. Roylance, D., *Stress Strain Curves*. 2001, Massachusetts Institute of Technology: Cambridge, MA.
70. Khanafer, K., M.S. Schlicht, and R. Berguer, *How should we measure and report elasticity in aortic tissue*. European Society for Vascular Surgery, 2013.
71. O'Rourke, M.F. and G. Mancia, *Arterial stiffness*. Journal of Hypertension, 1999. **17**: p. 1-4.
72. Fung, Y.C., *Biomechanics: Motion, Flow, Stress, and growth*. 1990, La Jolla, California: Springer-Verlag New York Inc.
73. Xenos, M., et al., *Patient-based abdominal aortic aneurysm rupture risk prediction with fluid structure interaction modeling*. Annals of Biomedical Engineering, 2010. **38**(11): p. 3323-37.
74. Xenos, M., et al., *Patient based Abdominal Aortic Aneurysm rupture risk prediction combining clinical visualizing modalities with fluid structure interaction numerical simulations*. 32nd Annual International Conference of the IEEE EMBS, Buenos Aires, Argentina, 2010.
75. C.S. Shin and R.A. Smith, *Fatigue crack growth at stress concentrations- the role of notch plasticity and crack closure*. Engineering Fracture Mechanics, 1988. **29**(3): p. 301-315.
76. Tomkins, B., *Fatigue failure criteria for thick-walled cylindrical pressure vessels*. Pressure Vessel & Piping, 1972(1): p. 37-59.

77. Salvucci F. P., et al., *Association between mechanics and structure in arteries and veins - Experiment on sheep*. 31st Annual International Conference of the IEEE EMBS, Minneapolis, Minnesota, USA, 2009.
78. Schmid, F., et al., *In situ tensile testing of human aortas by time-resolved small-angle X-ray scattering*. Journal of synchrotron radiation, 2005. **12**(Pt 6): p. 727-33.
79. S.J. Peterson, M.S.I., N.T Kouchoukos, F.C.P. Yin, R.J. Okamoto. *Biaxial mechanical properties of dilated human ascending aortic tissue*. in *Serving Humanity, Advancing Technology*. 1999. Atlanta, GA, USA: IEEE.
80. Kim, J. and S. Baek, *Circumferential variations of mechanical behavior of the porcine thoracic aorta during the inflation test*. Journal of Biomechanics, 2011.
81. Vorp, D.A., *Biomechanics of abdominal aortic aneurysm*. Journal of Biomechanics, 2007. **40**(9): p. 1887-1902.
82. Di Martino, E.S., et al., *Biomechanical properties of ruptured versus electively repaired abdominal aortic aneurysm wall tissue*. Journal of vascular surgery : official publication, the Society for Vascular Surgery [and] International Society for Cardiovascular Surgery, North American Chapter, 2006. **43**(3): p. 570-6; discussion 576.
83. Gershon B., Cohn D., and Marom G., *Compliance and ultimate strength of composite arterial prosthese*. Biomaterials, 1991. **13**(1).
84. C. J. Chuong and Y.C. Fung, *Compressibility and constitutive equation of arterial wall in radial compression experiments*. Journal Biomechanics, 1984. **17**(1): p. 35-40.
85. Ramesh N. Vaishnav, et al., *Nonlinear anistropic elastic of the canine aorta*. Biophysical Journal, 1972. **12**: p. 1008-1027.
86. Okamoto, R.J., et al., *Mechanical Properties of Dilated Human Ascending Aorta*. Annals of Biomedical Engineering, 2002. **30**(5): p. 624-635.
87. Thompson, R.W., et al., *Pathophysiology of abdominal aortic aneurysms: insights from the elastase-induced model in mice with different genetic backgrounds*. Annals of the New York Academy of Sciences, 2006. **1085**: p. 59-73.
88. Putatunda, S.K., *Influence of material strength level on fatigue crack closure*. Engineering Fracture Mechanics, 1988. **30**(5): p. 627-639.
89. Schijve, J., *The effect of pre-strain on fatigue crack growth and crack closure*. Engineering Fracture Mechanics, 1976. **8**: p. 575-581.
90. Steinman, D.A., *Image-Based Computational Fluid Dynamics Modeling in Realistic Arterial Geometries*. Annals of Biomedical Engineering, 2002. **30**(4): p. 483-497.
91. Doyle B. J., et al., *An experiment and numerical comparison of the rupture location of an Abdominal Aortic Aneurysm*. Journal of Endovascular Therapy, 2009. **16**: p. 322-335.
92. Finol, E.A. and C.H. Amon, *Flow dynamics in anatomical models of abdominal aortic aneurysms: computational analysis of pulsatile flow*. Acta cientifica venezolana, 2003. **54**(1): p. 43.
93. McGloughlin, T.M. and B.J. Doyle, *New approaches to abdominal aortic aneurysm rupture risk assessment: engineering insights with clinical gain*. Arteriosclerosis, thrombosis, and vascular biology, 2010. **30**(9): p. 1687-94.
94. J. L. Wang, et al., *Failure Criterion of collagen fiber- Viscoelastic behavior simulated by using load control data*. Theoretical and Applied Fracture Mechanics, 1997. **27**: p. 1-12.
95. Takeda, T., et al., *A novel ultrasound technique to study the biomechanics of human esophagus in vivo*. American Journal Physiol Gastrointest Liver Physiol, 2002(282): p. 785.
96. Salsac, A.V., S.R. Sparks, and J.C. Lasheras, *Hemodynamic changes occurring during the progressive enlargement of abdominal aortic aneurysms*. Annals of vascular surgery, 2004. **18**(1): p. 14-21.
97. Romanov V., Agah M R., and Darvish K. *Viscoelastcity properties of aorta from oscillatory pressure test*. in *Proceedings of the ASME 2011 Summer Bioengineering Conference*. 2011. Farmington, Pennsylvania, USA: ASME.
98. Tse, K.M., et al., *Investigation of hemodynamics in the development of dissecting aneurysm within patient-specific dissecting aneurismal aortas using computational fluid dynamics (CFD) simulations*. Journal of Biomechanics, 2011. **44**(5): p. 827-36.
99. Gao, F., O. Ohta, and T. Matsuzawa, *Fluid-structure interaction in layered aortic arch aneurysm model: assessing the combined influence of arch aneurysm and wall stiffness*. Australasian Physics & Engineering Sciences in Medicine, 2008. **31**(1): p. 32-41.
100. Barakat, A.I., et al., *Unsteady and Three-Dimensional Simulation of Blood Flow in the Human Aortic Arch*. Journal of Biomechanical Engineering, 2002. **124**(4): p. 378-387.
101. Tan, F.P.P., et al., *Analysis of flow patterns in a patient-specific thoracic aortic aneurysm model*. Computers & Structures, 2009. **87**(11-12): p. 680-690.
102. Vande Geest, J.P., et al., *Gender-related differences in the tensile strength of abdominal aortic aneurysm*. Annals of the New York Academy of Sciences, 2006. **1085**: p. 400-2.

103. Scotti, C.M., et al., *Fluid-structure interaction in abdominal aortic aneurysms: effects of asymmetry and wall thickness*. BioMedical Engineering OnLine, 2005. **4**: p. 64.
104. Rissland, P., et al., *AAA risk of rupture-Patient specific FSI simulation using anisotropic model*. Journal of Biomechanical Engineering, 2008. **131**(March, 2009).
105. Zheyang Wu, Chun Yang, and D. Tang. *A Predictive Method for human carotid plaque rupture using in vivo serial MRI with follow up scan showing actual rupture and MRI based 3D model with FSI*. in *Proceedings of the ASME 2011 Summer Bioengineering Conference*. 2011. Farmington, Pennsylvania, USA: ASME.
106. Fraser, K.H., et al., *Fluid-structure interaction in axially symmetric models of abdominal aortic aneurysms*. Proceedings of the Institution of Mechanical Engineers, Part H: Journal of Engineering in Medicine, 2009. **223**(2): p. 195-209.
107. Di Martino, E.S., et al., *Fluid-structure interaction within realistic three-dimensional models of the aneurysmatic aorta as a guidance to assess the risk of rupture of the aneurysm*. Medical Engineering & Physics, 2001. **23**: p. 647-655.
108. Shahcheraghi, N., et al., *Unsteady and three-dimensional simulation of blood flow in the human aortic arch*. Journal of Biomechanical Engineering, 2002. **124**: p. 378-387.
109. Vignon-Clementel, I.E., et al., *Outflow boundary conditions for three-dimensional finite element modeling of blood flow and pressure in arteries*. Computer Methods in Applied Mechanics and Engineering, 2006. **195**: p. 3776-3796.
110. Khalil, A.S., B.E. Bouma, and M.R. Kaazempur Mofrad, *A combined FEM/genetic algorithm for vascular soft tissue elasticity estimation*. Cardiovascular Engineering, 2006. **6**(3): p. 93-102.
111. Szczerba, D., et al., *Mechanism and localization of wall failure during abdominal aortic aneurysm formation*, in *Biomedical Simulation*, F. Bello and P.J. Edwards, Editors. 2008, Springer Heidelberg: Berlin. p. 119-126.
112. Xu, X.Y., et al., *Analysis of flow patterns in a patient-specific thoracic aortic aneurysm model*. Computers & Structures, 2008. **87**(11-12): p. 680-690.
113. Tremblay, D., et al., *A comparison of mechanical properties of materials used in aortic arch reconstruction*. The Annals of thoracic surgery, 2009. **88**(5): p. 1484-91.
114. Watton, P.N., et al., *Modelling evolution and the evolving mechanical environment of saccular cerebral aneurysms*. Biomechanics and Modeling in Mechanobiology, 2011. **10**(1): p. 109-32.
115. Younis, H.F., et al., *Hemodynamics and wall mechanics in human carotid bifurcation and its consequences for atherogenesis: investigation of inter-individual variation*. Biomechanics and Modeling in Mechanobiology, 2004. **3**: p. 17-32.
116. Zhao, S.Z., X.Y. Xu, and M.W. Collins, *The numerical analysis of fluid-solid interactions for blood flow in arterial structures Part 1: A review of models for arterial wall behaviour*. Proceedings of the Institution of Mechanical Engineers, Part H: Journal of Engineering in Medicine, 1998. **212**(4): p. 229-240.
117. Tang, D., et al., *Simulating cyclic artery compression using a 3D unsteady model with fluid-structure interactions*. Computers & Structures, 2002. **80**(20-21): p. 1651-1665.
118. Tang, D.L., et al., *Wall stress and strain analysis using a three-dimensional thick-wall model with fluid-structure interactions for blood flow in carotid arteries with stenoses*. Computers & Structures, 1999. **72**(1-3): p. 341-356.
119. Eigenbrodt, M.L., et al., *Mathematical estimation of the potential effect of vascular remodelling/dilatation on B-mode ultrasound intima-medial thickness*. QJM : monthly journal of the Association of Physicians, 2004. **97**(11): p. 729-37.
120. Payne, S.J., *Analysis of the effects of gravity and wall thickness in a model of blood flow through axisymmetric vessels*. Medical and Biological Engineering & Computing, 2004. **42**: p. 799-806.
121. Hall, A.J., et al., *Aortic wall tension as a predictive factor for abdominal aortic aneurysm rupture: improving the selection of patients for abdominal aortic aneurysm repair*. Annals of vascular surgery, 2000. **14**(2): p. 152-7.
122. Sun, Z. and T. Chaichana, *Investigation of the hemodynamic effect of stent wires on renal arteries in patients with abdominal aortic aneurysms treated with suprarenal stent-grafts*. Cardiovascular and interventional radiology, 2009. **32**(4): p. 647-57.
123. Gilpin, C.M., *Cyclic loading of porcine coronary arteries*, in *School of Mechanical Engineering*. 2005, Georgia Institute of Technology: Georgia.
124. Shukei Sugita, et al., *Evaluation of Rupture Properties of Thoracic Aortic Aneurysms in a Pressure-Imposed Test for Rupture Risk Estimation*. Cardiovascular Engineering and Technology, 2012. **3**(1): p. 41-51.
125. M. Bonert, et al. *The relationship between wall shear stress distributions and intimal thickening in the human abdominal aorta*. BioMedical Engineering OnLine, 2003. **2**.

126. Katritsis, D., et al., *Wall shear stress: theoretical considerations and methods of measurement*. Progress in Cardiovascular Diseases, 2007. **49**(5): p. 307-329.
127. Jackson, M., et al., *Low wall shear stress predicts subsequent development of wall hypertrophy in lower limb bypass grafts*. Artery Research, 2009. **3**: p. 32-38.
128. Cecchi, E., et al., *Role of hemodynamic shear stress in cardiovascular disease*. Atherosclerosis, 2011. **214**(2): p. 249-56.
129. <http://www.ansys.com/>.
130. Liu, B. *Computer simulations of flow in curved tube with stenosis*. in *COMSOL Multiphysics User's Conference*. 2005. Boston.
131. Leung, J.H., et al., *Fluid structural interaction of patient specific abdominal aortic aneurysms: a comparison with solid stress modes*. Biomedical Engineering Online, 2006. **5**(33): p. 1-15.
132. Scotti, C.M., et al., *Wall stress and flow dynamics in abdominal aortic aneurysms: finite element analysis vs. fluid-structure interaction*. Computer Methods in Biomechanics and Biomedical Engineering, 2008. **11**(3): p. 301-322.
133. Steinman, D.A., et al., *Reconstruction of carotid bifurcation hemodynamics and wall thickness using computational fluid dynamics and MRI*. Magnetic Resonance in Medicine, 2002. **47**(1): p. 149-159.
134. Perktold, K. and D. Hilbert, *Numerical simulation of pulsatile flow in a carotid bifurcation model*. Journal of Biomedical Engineering, 1986. **8**: p. 193-199.
135. Atabek, H.B., *Wave propagation through a viscous liquid contained in a tethered, initially stressed, orthotropic elastic tube*. Biophysical Journal, 1968. **8**(626-649).
136. O'Rourke, M.F., *Ascending aortic pressure wave indices and cardiovascular disease*. American Journal of Hypertension, 2004. **17**(8): p. 721-723.
137. Yahya, M., *"Three dimensional finite element modelling of blood flow in elastic vessel: Effects and arterial geometry and elasticity on aneurysm growth and rupture"* Master of Science Thesis. 2010, Ryerson University, Toronto, Ontario, Canada
138. Canic, S., et al., *Blood flow in compliant arteries: an effective viscoelastic reduced model, numerics, and experimental validation*. Annals of Biomedical Engineering, 2006. **34**(4): p. 575-592.
139. Nichols, W.W., *Clinical measurement of arterial stiffness obtained from noninvasive pressure waveforms*. American Journal of Hypertension, 2005. **18**: p. 3S-10S.
140. Quarteroni, A., M. Tuveri, and A. Veneziani, *Computational vascular dynamics: problems, models and methods*. Computing and Visualization in Science, 2000. **2**: p. 163-197.
141. Bathe, K.J., *Finite Element Procedures*. 1996, Englewood Cliffs, New Jersey: Prentice Hall.
142. Shaik, E., K.A. Hoffman, and J.F. Dietiker, *Numerical Flow Simulations of Blood in Arteries*. 2006, Aerospace Sciences Meeting and Exhibit, AIAA.
143. J W Doucette, et al., *Validation of a Doppler guide wire for intravascular measurement of coronary artery flow velocity*. Journal of the American Heart Association, 1992. **85**: p. 1899-1911.
144. Tierney, A.P., A. Callanan, and T.M. McGloughlin, *In vivo feasibility case study for evaluating abdominal aortic aneurysm tissue properties and rupture potential using acoustic radiation force impulse imaging*. Journal of the mechanical behavior of biomedical materials, 2011. **4**(3): p. 507-13.
145. Wilson, K.A., et al., *The relationship between aortic wall distensibility and rupture of infrarenal abdominal aortic aneurysm*. Journal of vascular surgery : official publication, the Society for Vascular Surgery [and] International Society for Cardiovascular Surgery, North American Chapter, 2003. **37**(1): p. 112-7.
146. Brown, L.C. and J.T. Powell, *Risk factors for aneurysm rupture in patients kept under ultrasound surveillance*. Annals of Surgery, 1999. **230**(3): p. 289-297.
147. Long, A., et al., *Compliance of abdominal aortic aneurysm: evaluation of tissue doppler imaging*. Ultrasound in Medical and Biology, 2004. **30**(9): p. 1099-1108.
148. Teaching, E.U. <http://www.emergencyultrasoundteaching.com/>.
149. Pulsecor. <http://www.pulsecor.com/products/r65-vascular-monitor.html>.
150. Park, D.W., et al., *Arterial elasticity imaging: comparison of finite-element analysis models with high-resolution ultrasound speckle tracking*. Cardiovascular ultrasound, 2010. **8**: p. 22.
151. <http://www.aorticdissection.com>. 2003-2008; AorticDissection.com 2003-2008]. Available from: <http://www.aorticdissection.com/DISEASES%20OF%20AORTA.htm>.
152. ANSYS, I., *ANSYS Mechanical APDL Material Reference Release 14.5*. 2012, Canonsburg, PA: ANSYS.
153. Schurink, G.W.H., et al., *Thrombus within an aortic aneurysm does not reduce pressure on the aneurysmal wall*. Journal of Vascular Surgery, 2000. **31**: p. 501-506.
154. Mendenhall, W., *Introduction to Probability and Statistics*. Vol. 3rd Edition. 1971, Duxbury.
155. Wikipedia, [http://en.wikipedia.org/wiki/Linear\\_regression](http://en.wikipedia.org/wiki/Linear_regression).
156. Wikipedia, <http://en.wikipedia.org/wiki/P-value>.

157. Huang, Y., et al., *In vivo MRI-based simulation of fatigue process: a possible trigger for human carotid atherosclerotic plaque rupture*. BioMedical Engineering OnLine, 2013. **12**(36): p. 1-12.
158. Dindorf, R. and J. Wolkow, *Modelling of pulsatory flows in blood vessels*. Acta of Bioengineering and Biomechanics, 2001. **3**(2): p. 16-30.
159. T.M., J., *The value of the Energy Relation in the Testing of Ferrous Metals at Varying Ranges of Stress and at Intermediate and High Temperature*. Philosophical Magazines, 1923. **6**(46): p. 609-627.
160. N., E. *On Fatigue Test Under Progressive Stress*. in *Proc ASTM*. 1955.
161. Feltner, C.E. and M. J.D., *Microplastic Strain Hysteresis Energy as a Criterion for Energy Fracture*. Journal of Basic Engineering Transaction, ASME, 1966. **83**: p. 15-22.
162. E., S., *A Study of the Energy Criterion for Fatigue*. Nuclear Engineering and Design, 1966. **3**: p. 32-40.
163. NVIDIA, <http://www.nvidia.com/object/what-is-gpu-computing.html#sthash.JZ9RRu6M.dpuf>.

## APPENDIX A: HUMAN ETHICS APPROVAL



11 December 2012

Ahmed Al Jumaily  
Faculty of Design and Creative Technologies  
Dear Ahmed

Re Ethics Application: **12/273 Personalized Aneurysm Rupture Risk Prediction- Patient assessment through Ultrasound to measure real time deformation development of Aneurysm based on pressure waveform.**

Thank you for providing evidence as requested, which satisfies the points raised by the AUT University Ethics Committee (AUTE C).

Your ethics application has been approved for three years until 11 December 2015.

As part of the ethics approval process, you are required to submit the following to AUTE C:

- A brief annual progress report using form EA2, which is available online through <http://www.aut.ac.nz/research/research-ethics/ethics>. When necessary this form may also be used to request an extension of the approval at least one month prior to its expiry on 11 December 2015;
- A brief report on the status of the project using form EA3, which is available online through <http://www.aut.ac.nz/research/research-ethics/ethics>. This report is to be submitted either when the approval expires on 11 December 2015 or on completion of the project.

It is a condition of approval that AUTE C is notified of any adverse events or if the research does not commence. AUTE C approval needs to be sought for any alteration to the research, including any alteration of or addition to any documents that are provided to participants. You are responsible for ensuring that research undertaken under this approval occurs within the parameters outlined in the approved application.

AUTE C grants ethical approval only. If you require management approval from an institution or organisation for your research, then you will need to obtain this. If your research is undertaken within a jurisdiction outside New Zealand, you will need to make the arrangements necessary to meet the legal and ethical requirements that apply there.

To enable us to provide you with efficient service, please use the application number and study title in all correspondence with us. If you have any enquiries about this application, or anything else, please do contact us at [ethics@aut.ac.nz](mailto:ethics@aut.ac.nz).

All the very best with your research,

A handwritten signature in black ink, appearing to read 'Rosemary Godbold', is written over a horizontal line.

Dr Rosemary Godbold  
Executive Secretary

**Auckland University of Technology Ethics Committee**

Cc: Abd Halim Embong [abdhalim.embong@aut.ac.nz](mailto:abdhalim.embong@aut.ac.nz)

23 November 2012

Dear Dr Mahadevan

Thank you for registering your proposed study with the Counties Manukau DHB Research

Office:

Research Registration Number: 1404

Research Project Title: **Personalized Aneurysm Rupture Risk Prediction – Patient Assessment through Ultrasound to measure real time deformation development of Aneurysm based on pressure waveform**

Please accept this letter as confirmation of provisional approval for the proposed study to proceed at our organisation. Final approval will be provided once we have received confirmation of ethical approval via the Auckland University of Technology Ethical Committee and approval for the research to proceed from our Director of Hospital Services.

Yours Sincerely,

*S. Everitt.*

Dr Samantha Everitt

**Manager Research Office**

Counties Manukau District Health Board

## APPENDIX B: SPECIMEN TRUE STRESS AND TRUE STRAIN

### A.1 Maximum True Stress in specimen by Sugita [124]

The tensile stress  $\sigma$  of each specimen is given by Laplace's law:

$$\sigma = \frac{PR}{2T}, \quad (\text{A1})$$

where  $P$  is the pressure,  $R$  the radius of curvature, and  $T$  the thickness of the specimen during pressurization. When the maximum deformation  $D_{max}$  was less than the radius of the hole of the metal plate  $r$  ( $D_{max} < r$ ), the stress  $\sigma$  attains the maximum value at the point where the curvature radius  $R$  is the largest, as shown in Eq. A1. Since  $R$  is largest at the center of the specimen (see Appendix B), the maximum value of  $R$  is calculated as follows:

$$R = \frac{r^2}{D_{max}}. \quad (\text{A2-1})$$

When  $D_{max} \geq r$ ,  $R$  is identical to  $r$ :

$$R = r. \quad (\text{A2-2})$$

Due to the incompressibility of the specimens, the thickness of a specimen during pressurization  $T$  is calculated from the volume of the specimen at the no-load state (Fig. 2a) as follows:

$$T = \frac{\pi \cdot t}{S}, \quad (\text{A3})$$

where  $t$  is the thickness at the no-load state, and  $S$  the area of the curved surface of the specimen at  $P$ . When  $D_{max} < r$ , the surface of specimen  $S$  is written as follows:

$$S = \pi \left\{ r^2 + \frac{D_{max}^2}{e} \log \left[ \frac{r(e+1)}{D_{max}} \right] \right\}, \quad e = \frac{\sqrt{D_{max}^2 - r^2}}{r} \quad (\text{A4-1})$$

where  $e$  is an eccentricity (see Appendix C). When  $D_{max} < r$ ,  $S$  is calculated as the sum of the surface of the hemisphere with radius  $r$  and cylinder with length  $D_{max} - r$ :

$$S = \frac{4\pi r^2}{2} + 2\pi r(D_{max} - r) = 2\pi r D_{max}. \quad (\text{A4-2})$$

Substituting Eqs. A2–A4 into Eq. A1, we obtain the following:

$$\sigma = \frac{P}{2tD_{max}} \left\{ r^2 + \frac{D_{max}^2}{e} \log \left[ \frac{r(e+1)}{D_{max}} \right] \right\} \quad (D_{max} < r) \quad (1-1)$$

$$\sigma = \frac{PD_{max}}{t} \quad (D_{max} \geq r) \quad (1-2)$$

## A.2 Strain of the specimen

The strain of the specimen was calculated from the changes in the length passing through the top of the specimen ( $x = 0, y = 0$ ) along the surface of the specimen. When  $D_{max} < r$ , the length on the specimen equals half of the circumferential length of an ellipsoid with  $a$  and  $b$  values of the major and minor semi-axes, respectively as shown in Fig. 9. Since the circumferential length of the ellipsoid  $L_{circ-ellipsoid}$  was not strictly calculated from the integration, we used the approximation formula of circumferential length of an ellipsoid as follows:

$$L_{circ-ellipsoid} \approx \pi(a+b) \left[ 1 + \frac{1}{4} \left( \frac{a-b}{a+b} \right)^2 + \frac{1}{64} \left( \frac{a-b}{a+b} \right)^4 + \frac{1}{256} \left( \frac{a-b}{a+b} \right)^6 \right]. \quad (D1)$$

Here, we used a third-order approximation for the circumference of an ellipse. Since the length at no load equals  $2r$ , strain  $\varepsilon$  is written as follows:

$$\varepsilon = \frac{L_{circ-ellipsoid}}{4r} - 1. \quad (D2)$$

By substituting Eq. D1,  $r$ , and  $D_{max}$  into Eq. D2,  $a$ , and  $b$ , respectively, we obtain:

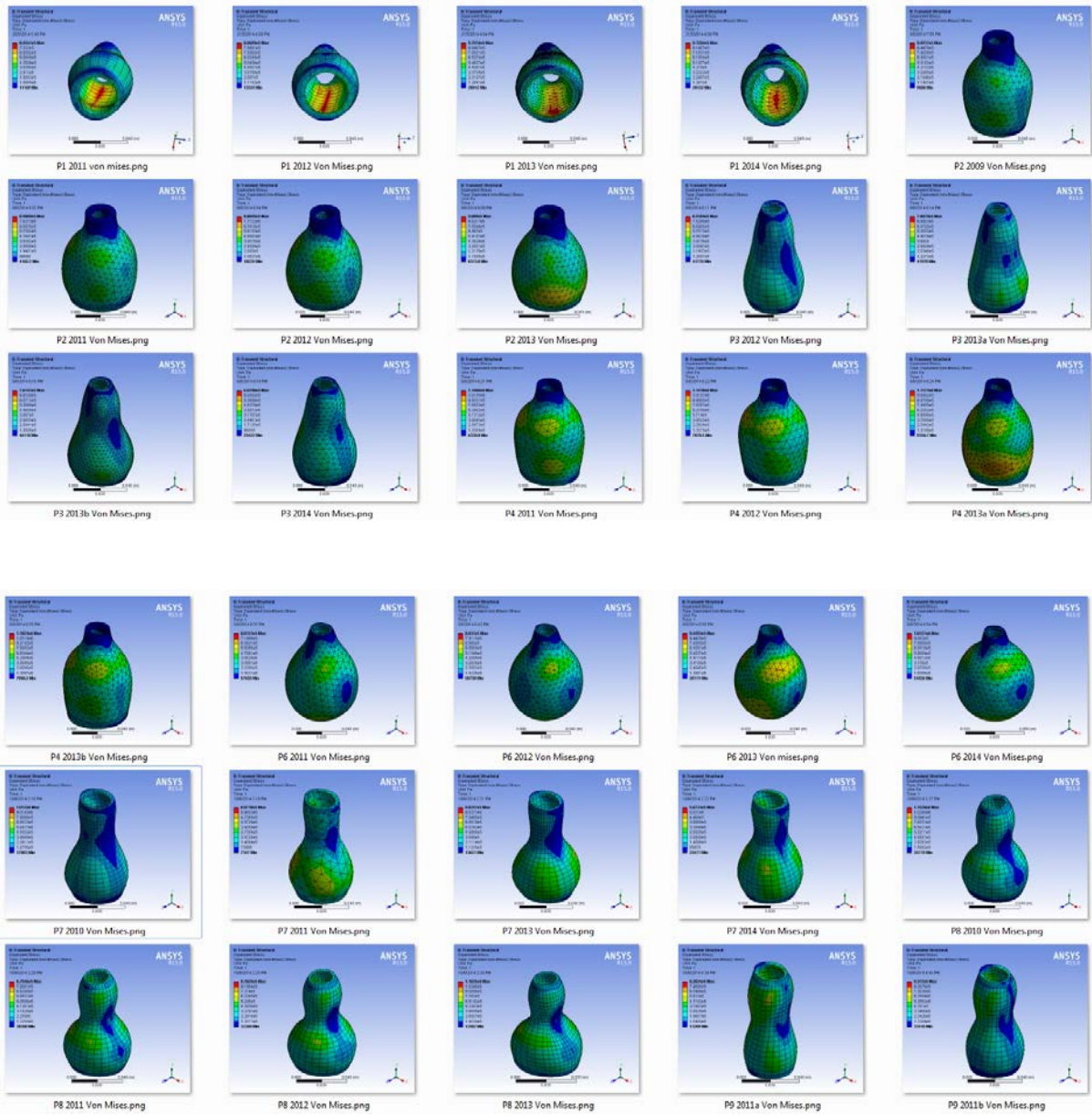
$$\varepsilon \approx \frac{\pi(r+D_{max})}{4r} \left[ 1 + \frac{1}{4} \left( \frac{r-D_{max}}{r+D_{max}} \right)^2 + \frac{1}{64} \left( \frac{r-D_{max}}{r+D_{max}} \right)^4 + \frac{1}{256} \left( \frac{r-D_{max}}{r+D_{max}} \right)^6 \right] - 1. \quad (D_{max} < r) \quad (2-1)$$

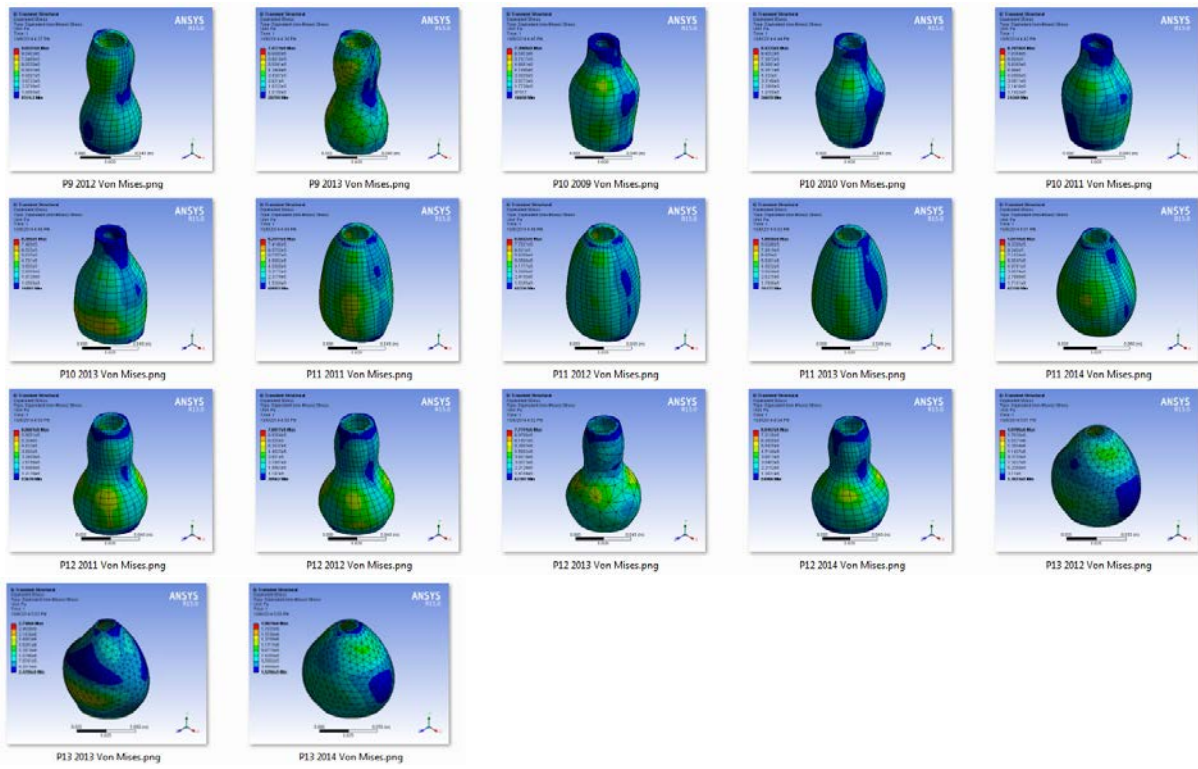
When  $D_{max} \geq r$ , the length on the specimen equals half of the circumferential length of a circle with radius  $r$  plus twice the length of the cylinder. Thus, the strain  $\varepsilon$  is written directly as follows:

$$\varepsilon = \frac{\pi r + 2(D_{max} - r)}{2r} - 1. \quad (D_{max} \geq r) \quad (2-2)$$

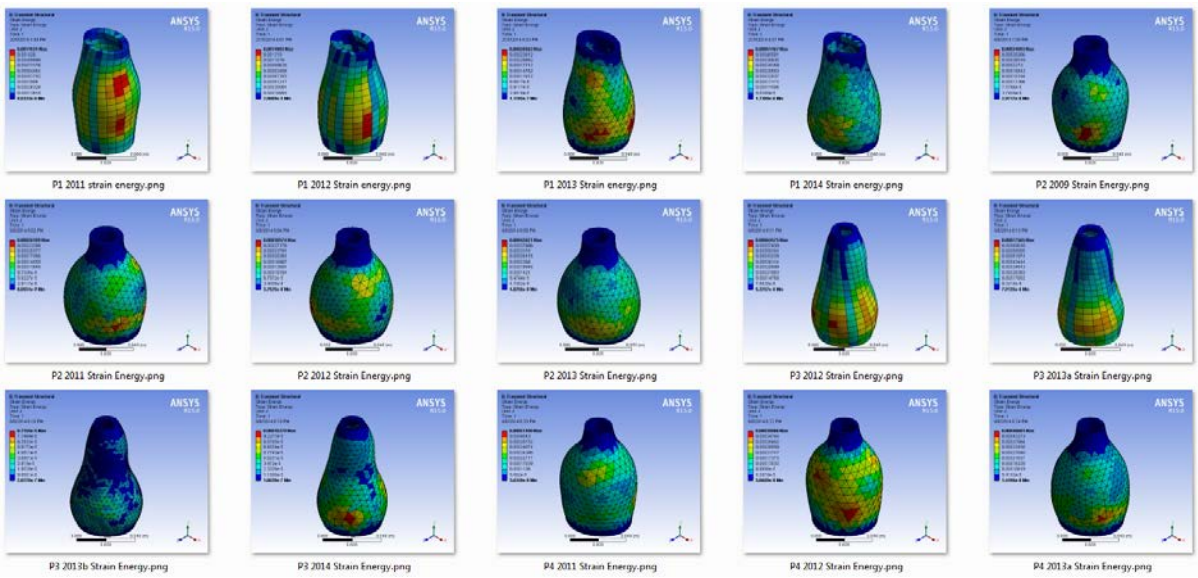
# APPENDIX C: ANEURYSM PSAM RESULTS

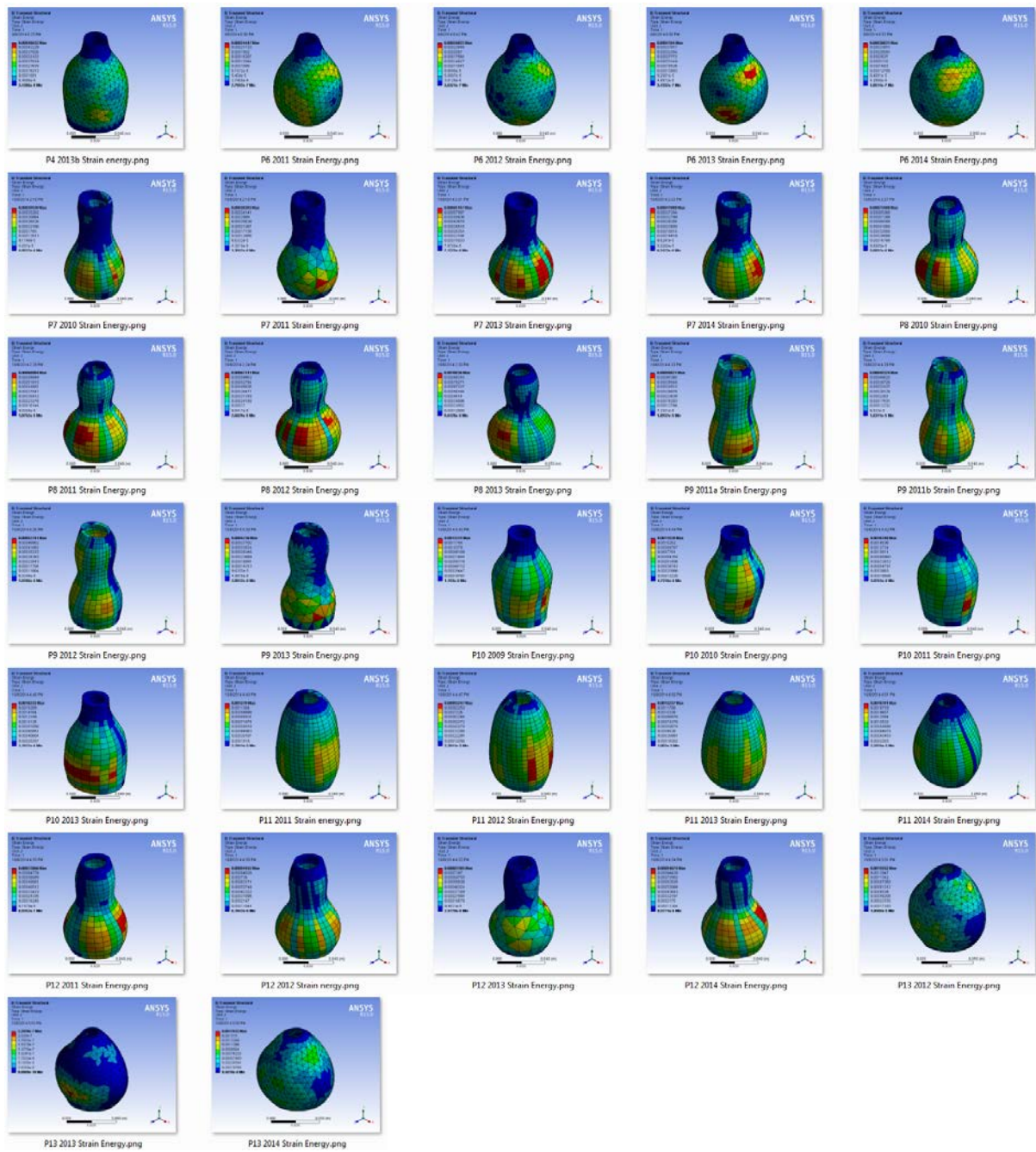
## B.1 Patient-Specific Von Mises Stress





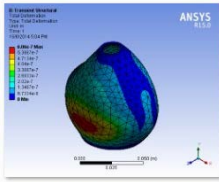
## B.2 Patient-Specific Strain Energy



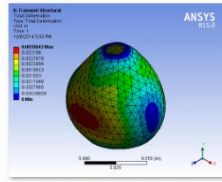


### B.3 Patient-Specific Deformation





P13 2013 Total Deformation.png



P13 2014 Total Deformation.png

## APPENDIX D: ANEURYSM GEOMETRY BASED ON 3 YEARS

### PROGRESS

Patient1	13/05/2011	7/08/2012	14/03/2013	21/01/2014	13/05/2011	7/08/2012	14/03/2013	21/01/2014
	2010	2011	2012	2013	2011	2012	2013	2014
	Segment4	Segment4	Segment4	Segment4	Segment5	Segment5	Segment5	Segment5
Vertical	3.81	4.41	4.31	4.44	3.84	4.43	4.52	4.62
Horizontal	3.81	4.44	4.51	5.18	3.91	4.38	4.38	5.28
A	0.58	0.61	0.5	0.53	0.64	0.66	0.5	0.58
C	0.45	0.32	0.26	0.45	0.45	0.58	0.4	0.42
E	0.53	0.58	0.48	0.34	0.37	0.48	0.48	0.45
G	0.45	0.56	0.34	0.48	0.53	0.56	0.48	0.4
Patient2	22/10/2009	20/09/2011	31/08/2012	14/03/2013	22/10/2009	20/09/2011	31/08/2012	14/03/2013
	2009	2011	2012	2013	2009	2011	2012	2013
	Segment4	Segment4	Segment4	Segment4	Segment5	Segment5	Segment5	Segment5
Vertical	4.53	5.13	5.25	5.34	4.51	5.13	5.38	5.34
Horizontal	5.02	5.21	5.63	5.74	4.7	5.21	5.21	5.68
A	0.69	0.53	0.51	0.58	0.43	0.53	0.5	0.53
C	0.37	0.56	0.56	0.24	0.53	0.56	0.4	0.34
E	0.54	0.48	0.42	0.4	0.4	0.48	0.45	0.4
G	0.42	0.42	0.48	0.53	0.34	0.42	0.32	0.53
Patient3	24/01/2012	14/03/2013	10/09/2013	27/03/2014	24/01/2012	14/03/2013	10/09/2013	27/03/2014
	2012	2013	2013	2014	2012	2013	2013	2014
	Segment4	Segment4	Segment4	Segment4	Segment5	Segment5	Segment5	Segment5
Vertical	3.62	3.64	4.06	4.12	3.69	4.02	4.13	4.12
Horizontal	3.93	3.56	4.21	4.16	3.75	4.19	4.26	4.23
A	0.53	0.45	0.48	0.56	0.37	0.45	0.37	0.61
C	0.32	0.29	0.37	0.5	0.42	0.48	0.35	0.58
E	0.48	0.5	0.48	0.53	0.42	0.32	0.35	0.5
G	0.34	0.32	0.37	0.53	0.45	0.45	0.42	0.56
Patient4	29/06/2011	8/08/2012	14/03/2013	28/08/2013	29/06/2011	8/08/2012	14/03/2013	28/08/2013
	2011	2012	2013	2013	2011	2012	2013	2013
	Segment4	Segment4	Segment4	Segment4	Segment5	Segment5	Segment5	Segment5
Vertical	4.5	4.67	4.57	4.45	4.6	4.77	4.66	5.01
Horizontal	4.65	4.62	4.82	5.08	5.12	4.85	4.96	4.93
A	0.42	0.51	0.34	0.32	0.48	0.42	0.29	0.51
C	0.27	0.32	0.21	0.37	0.34	0.34	0.34	0.37
E	0.37	0.41	0.21	0.4	0.35	0.48	0.32	0.4
G	0.4	0.42	0.24	0.43	0.32	0.4	0.34	0.27

Patient8	14/12/2010	26/07/2011	9/05/2012	27/06/2013	14/12/2010	26/07/2011	9/05/2012	27/06/2013
	2010	2011	2012	2013	2010	2011	2012	2013
	<b>Segment4</b>	<b>Segment4</b>	<b>Segment4</b>	<b>Segment4</b>	<b>Segment5</b>	<b>Segment5</b>	<b>Segment5</b>	<b>Segment5</b>
Vertical	4.29	4.46	4.58	4.66	4.4	4.48	4.58	5.27
Horizontal	4.97	4.89	5.04	5.46	4.64	4.7	4.76	5.87
A	0.42	0.44	0.48	0.4	0.42	0.48	0.34	0.37
C	0.37	0.4	0.36	0.4	0.4	0.37	0.45	0.26
E	0.32	0.36	0.4	0.37	0.45	0.4	0.37	0.45
G	0.42	0.44	0.45	0.32	0.37	0.45	0.4	0.42
Patient9	18/03/2011	27/09/2011	26/01/2012	27/06/2013	18/03/2011	27/09/2011	26/01/2012	27/06/2013
	2011	2011	2012	2013	2011	2011	2012	2013
	<b>Segment4</b>	<b>Segment4</b>	<b>Segment4</b>	<b>Segment4</b>	<b>Segment5</b>	<b>Segment5</b>	<b>Segment5</b>	<b>Segment5</b>
Vertical	3.36	3.84	3.98	3.62	3.45	3.93	3.8	4.06
Horizontal	3.19	3.83	3.5	3.62	3.36	3.81	3.79	4.03
A	0.37	0.4	0.45	0.37	0.42	0.42	0.56	0.48
C	0.34	0.45	0.42	0.35	0.29	0.42	0.48	0.37
E	0.29	0.4	0.45	0.32	0.34	0.45	0.43	0.32
G	0.34	0.4	0.42	0.26	0.32	0.5	0.5	0.37
Patient10	22/09/2009	9/12/2010	7/02/2011	27/06/2013	22/09/2009	9/12/2010	7/02/2011	27/06/2013
	2009	2010	2011	2013	2009	2010	2011	2013
	<b>Segment4</b>	<b>Segment4</b>	<b>Segment4</b>	<b>Segment4</b>	<b>Segment5</b>	<b>Segment5</b>	<b>Segment5</b>	<b>Segment5</b>
Vertical	3.89	3.61	4.63	4.34	3.93	3.09	3.8	4.51
Horizontal	4.32	4.22	3.93	5.1	4.44	3.34	4.29	5.24
A	0.5	0.53	0.42	0.56	0.54	0.53	0.58	0.5
C	0.4	0.45	0.53	0.32	0.48	0.45	0.4	0.37
E	0.61	0.48	0.57	0.45	0.4	0.48	0.69	0.4
G	0.4	0.34	0.5	0.32	0.42	0.34	0.56	0.45
Patient11	4/08/2011	1/11/2012	15/08/2013	19/03/2014	4/08/2011	1/11/2012	15/08/2013	19/03/2014
	2011	2012	2013	2014	2011	2012	2013	2014
	<b>Segment3</b>	<b>Segment3</b>	<b>Segment3</b>	<b>Segment3</b>	<b>Segment4</b>	<b>Segment4</b>	<b>Segment4</b>	<b>Segment4</b>
Vertical	4.23	4.39	4.44	4.62	4.34	4.45	4.56	4.96
Horizontal	4.43	4.74	5.02	5.94	4.69	4.77	5.02	6.14
A	0.42	0.4	0.53	0.42	0.43	0.54	0.53	0.5
C	0.37	0.45	0.4	0.29	0.41	0.48	0.4	0.37
E	0.32	0.4	0.37	0.4	0.32	0.42	0.34	0.4
G	0.32	0.5	0.42	0.34	0.32	0.45	0.29	0.37

## APPENDIX E: GOODMAN STRESS RANGE RECONSTRUCTION

1. Using information from Figure 7.8, a straight line approximation to the failure data is constructed in the tensile region where alternating stress ( $\sigma_{\text{alternating}}$ ) is constructed on X-Axis versus mean stress ( $\sigma_{\text{mean}}$ ) on Y-axis, as correspond to a failure life of N cycles.
2. This linear approximation passes through the point endurance strength ( $\sigma_{\text{Endurance}}$ ) on the X- axis and through the point Ultimate stress ( $\sigma_{\text{ultimate}}$ ) on the Y-axis.
3. In this calculation, only tensile mean data is used for Goodman relation diagram since the approximation values were generated from tensile testing.
4. Line representing the  $\sigma_{\text{mean}}$  is plotted. If the scale of X-axis is equal to the scale in Y-axis, the  $\sigma_{\text{mean}}$  line will make 45 degrees angle with coordinate axis.
5. This  $\sigma_{\text{mean}}$  line is used as a reference for plotting the next maximum stress ( $\sigma_{\text{maximum}}$ ) and minimum stress ( $\sigma_{\text{minimum}}$ ) on the range on stress diagram.
6. The  $\sigma_{\text{maximum}}$  line is obtained by adding the  $\sigma_{\text{alternating}}$  line to the  $\sigma_{\text{mean}}$  line.

$$\sigma_{\text{maximum}} = \sigma_{\text{alternating}} + \sigma_{\text{mean}}$$

7. The  $\sigma_{\text{minimum}}$  line is obtained by subtracting the  $\sigma_{\text{alternating}}$  line from  $\sigma_{\text{mean}}$  line.

$$\sigma_{\text{minimum}} = \sigma_{\text{mean}} - \sigma_{\text{alternating}}$$

8. The diagram will be then truncated at the yield point both on tension and in compression as figure 7.10 to complete the diagram.